Elektrische Energietechnik an der TU Berlin Band 9

Rong Dong

Design and comparison of two brushless DC drives for an electric propulsion system of solar-power unmanned aerial vehicles

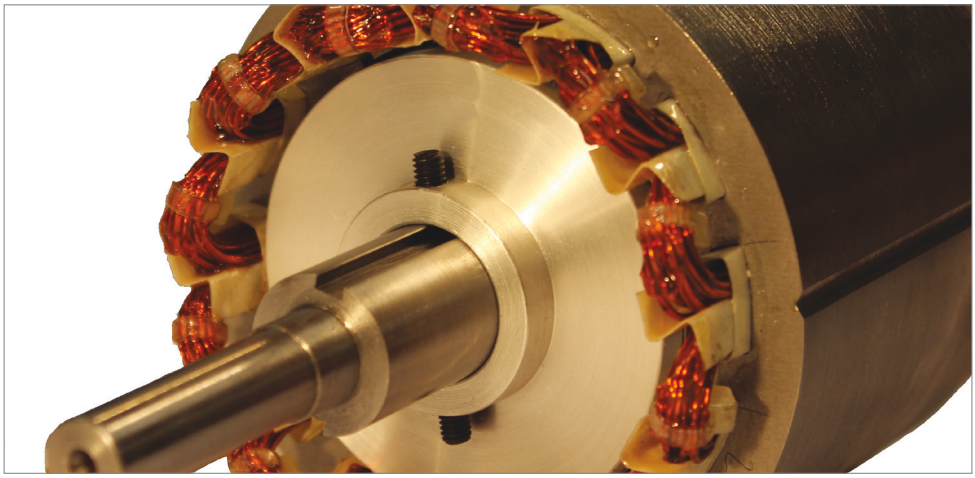

Universitätsverlag der TU Berlin

Technische Universität Berlin

Rong Dong

Design and Comparison of two Brushless DC Drives for an Electric Propulsion System of Solar-Power Unmanned Aerial Vehicles

The scientific series *Elektrische Energietechnik an der TU Berlin* is edited by:
Prof. Dr. Sibylle Dieckerhoff,
Prof. Dr. Julia Kowal,
Prof. Dr. Ronald Plath,
Prof. Dr. Uwe Schäfer

Elektrische Energietechnik an der TU Berlin | 9

Rong Dong

Design and Comparison of two Brushless DC Drives for an Electric Propulsion System of Solar-Power Unmanned Aerial Vehicles

Universitätsverlag der TU Berlin

Bibliographic information published by the Deutsche Nationalbibliothek
The Deutsche Nationalbibliothek lists this publication in the Deutsche Nationalbibliografie; detailed bibliographic data are available on the Internet at http://dnb.dnb.de.

Universitätsverlag der TU Berlin, 2020
http://verlag.tu-berlin.de

Fasanenstr. 88, 10623 Berlin
Tel.: +49 (0)30 314 76131 / Fax: -76133
E-Mail: publikationen@ub.tu-berlin.de

Zugl.: Berlin, Techn. Univ., Diss., 2019
Gutachter: Prof. Dr.-Ing. Uwe Schäfer
Gutachter: Prof. Dr.-Ing. Sibylle Dieckerhoff
Gutachter: Prof. Dr.-Ing. Sami Hlioui (ENS de Cachan, Frankreich)
Die Arbeit wurde am 08. November 2019 an der Fakultät IV unter Vorsitz von Prof. Dr.-Ing. Julia Kowal erfolgreich verteidigt.

Print: docupoint GmbH
Layout/Typesetting: Rong Dong

ISBN 978-3-7983-3126-6 (print)
ISBN 978-3-7983-3127-3 (online)

ISSN 2367-3761 (print)
ISSN 2367-377X (online)

Published online on the institutional repository of the Technische Universität Berlin:
DOI 10.14279/depositonce-9331
http://dx.doi.org/10.14279/depositonce-9331

ACKNOWLEDGEMENTS

The work of this dissertation was completed during the time I worked at the research institute of Elektrische Antriebstechnik at Technical University of Berlin.

First of all, I would like to thank my doctoral supervisor, Prof. Dr.-Ing. Uwe Schäfer. He provided me a great opportunity to study the scientific research and practice work, which not only cultivated my ability to think independently, but also inspired me to move forward. His experienced advice and guidance are the prerequisites for my successful completion of the thesis today.

Without the master's study under the supervision of Prof. Manfeng Dou at the research institute of permanent rare earth magnetic machine at Northwesten Polytechnical University, I would never have had the opportunity to contact this aviation field and continue to carry out the corresponding work.

I especially thank the colleagues who helped me during my work. Mechanical technician Mr. Jürgen Federspiel assembled the designed motor and helped me to built up the test bench setup and our laboratory engineer Mr. Arno Hellemann ordered the materials and components for my project. Special thanks I would give to the students who worked with me on this project.

Finally, I am grateful to my family with unconditional support and encouragement.

ZUSAMMENFASSUNG

Das elektrische Antriebssystem als Kernkomponente von unbemannten Solar Flugzeugen(UAVs, Unmanned Aerial Vehicles) für Langzeitflüge erfordert eine hohe Leistungsdichte und robuste Antriebstechnik. Bürstenlose Gleichstrommotoren (BLDCM) mit hoher Leistungs- und Drehmomentdichte sowie dafür angepasste Regelalgorithmen werden daher bevorzugt in UAVs eingesetzt.

Diese Dissertation zielt darauf ab, einen verbesserten BLDCM mit nur 4 eingebetteten Magnetblöcken zu entwerfen, um 8 Pole zu realisieren im Vergleich zu der herkömmlichen Struktur mit 8 Magnetblöcken. Das Verhalten beider BLDCM-Designs wurde analytisch ermittelt und die Motormodelle mit Hilfe von Finite-Elemente-Software in ANSYS verifiziert. Design und Konstruktion der Prototypen mit der vorgeschlagenen und der herkömmlichen Magnetstruktur wurden durchgeführt und es wurde ein Prüfstand für einen umfassenden Leistungsvergleich aufgebaut.

Da die vorgeschlagene Magnetstruktur zu einem Magnetkreis führt, bei dem die entgegengesetzten Pole keine Spiegelsymmetrie aufweisen, wurden die Längs- und Querinduktivität durch Finite-Elemente-Modellanalyse und Experimente absolut und differentiell untersucht. Weiterhin wurden Wirkungsgradkennfelder erstellt und das thermische Verhalten untersucht, um ein umfassendes Verständnis der beiden Motoren zu erhalten.

Um das sensorbedingte Ausfallrisiko zu eliminieren, wurde eine schnelle analoge Isolationsschaltung mit hoher Linearität und Stabilität zur Messung der gepulsten Spannungen bei 270 V Gleichspannung entwickelt, um eine sensorlose Steuerungsstrategie zu realisieren. Die Schaltung verwendet einen linearen Optokoppler mit integrierter Rückkopplungsfotodiode, sowie einen PI-Regler mit schnellen Operationsverstärkern im Rückkopplungspfad.

Ein 3D-Statormodell wurde erstellt, um die mechanischen Resonanzfrequenzen und die mögliche Anregung durch die elektromagnetische Radialkraft zu analysieren, die zu Vibrationen und Geräuschen bei der vorgeschlagenen und herkömmlichen Rotorstruktur führt. Es wurde auch eine analytische Modalanalyse durchgeführt, um die Genauigkeit von FEM-Simulationen und experimentellen Ergebnissen mit dem Impulshammer zu vergleichen und zu validieren.

ABSTRACT

The electrical propulsion system as the core component of solar-power Unmanned Aerial Vehicles (UAVs) for long duration flight requires high power density and stable drive technology. Brushless DC motors (BLDCM) with high power and torque density and control algorithms suitable for drive system are given preference for the application in UAVs.

This dissertation is aimed at designing an improved BLDCM using only 4 interior magnet blocks to realize 8 poles compared to the conventional 8 magnet blocks structure. The performances of both BLDCM designs have been analytically determined and the motor models were verified through finite element software in ANSYS. Design and construction of the demonstrators of BLDCMs with the proposed and the conventional magnet structure have been carried out and a test bench for extensive performance comparison has been set up.

Since the proposed magnet structure leads to a particularity of the magnetic circuit, the behavior of absolute and differential synchronous direct and quadrature inductances have been investigated by finite element model analysis and experiments. Efficiency maps were generated and thermal characteristics have been measured to gain a comprehensive understanding of the two motors.

To reduce the uncertainty of sensor control for BLDCM, a high speed, good linearity analog isolation circuit to measure the voltages of 270 V DC voltage to realize sensorless control strategy has been designed. The circuit combines a PI controller with fast operational amplifiers with a built-in linearizing feedback photodiode loop of a linear optocoupler.

A 3D stator model was built to analyse the mechanical resonance frequencies and possible excitation by the electromagnetic radial force leading to vibration and noise for the proposed and conventional rotor structure. Analytical calculation of natural mode frequencies has also been conducted to compare and validate the accuracy of FEM simulations and impact hammer testing experimental results.

Contents

1 Introduction

An aircraft capable of sustained flight, propelled by a zero emission renewable energy source, is a very attractive aerial platform. The increasing application of Unmanned Aerial Vehicles (UAVs) for science and civil purposes includes monitoring forest fires, border surveillance, weather prediction, etc. [1]. Corresponding research is comprehensively carried on.

In 1954, Daryl Chapin, Calvin Fuller, and Gerald Pearson invented the first silicon photovoltaic cell [2] which could transfer the sun's energy to electric power. Further progress made solar technology usable for propulsion of electric model airplanes become reality. Solar power driven UAV applications reduce the need for UAVs returning back to ground for changing batteries or recharging. The first flight of a solar-powered UAV, called **Sunrise I**, and an improved version, **Sunrise II**, were built and tested on the 4$^{\text{th}}$ of November 1974 and 12$^{\text{th}}$ of September 1975, respectively [3].

Short-endurance UAVs fail to accomplish long strategic missions due to their power source limitations. Although the solar power is used for extension of flight duration, current flight times are limited by the battery capacity. The ability of the UAV to fly for an extended period of time has been a challenge for the aeronautical organizations [4]. Recently, there has been great interest in the development of advanced long-endurance UAV capable of executing missions in higher altitude environments resulting in less power consumption and large amount of solar energy [5]. The main issue in high altitude flight is generating lift in the low density atmosphere. The majority of vehicles that operate at these altitudes do so by flying fast [6].

Recent remarkable solar powered long-endurance UAVs are listed as follows: Sky-Sailor with 3.2 m wing span and 2.4 kg weight is designed to cruise on Mars. Sky-Sailor has demonstrated the possiblity of continuous flight. It flew nonstop for 27 hours in June, 2008 [3]. Zephyr has been developed as a high altitude long endurance platform [1]. On 11th July 2018, Zephyr 8 flew for 25 days, 23 hours and 57 minutes in summer weather conditions, and has also performed successfully the high altitude pseudo-satellite program. Its wing span is 28 m and the weight is 53 kg, as shown in Fig. 1.1.

The flight duration of UAV varies widely depending on the aircraft size and its operation [7]. Due to lower effort for assembly, easier transportation and reduced requirements for the taking off and landing site, a small solar powered UAVs structure aiming for longer flight duration will be used as an application object for this thesis.

Fig. 1.1: Mechanical structure of Zephyr [8]

1.1 UAV specification

The current thinking for an aircraft's renewable energy system is to employ a photovoltaic array coupled to an electrochemical energy storage system such as fuel cells or battery. This construction provides the possibility of the long duration operation mode. The solar-powered UAVs collect and consume solar energy during the day and store the remaining part for the night flight.

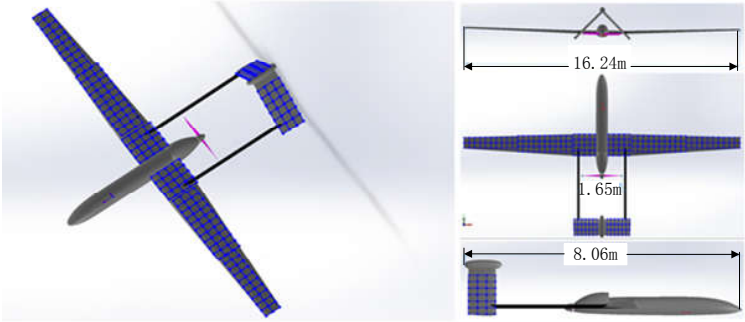

Fig. 1.2: Mechanical structure of Climate-Sailor [9]

The operational environment and mission requirements also have a significant influence on an UAV's capabilities. Take an airship as an example, operating the airship under minimum aerodynamic drag conditions will produce the maximum performance with the minimum size. For observation missions, the station-keeping drag is a function of mean wind velocity, airship's size, weight including payload, and the air density at working altitude [6].

As shown in Fig. 5 from [10], the gradient of the solar radiation increases slowly above 20 km altitude but the wing span increases dramatically. The required wing area for solar cells will increase at high altitudes. Moreover, increasing the operational altitude can lead to a heavier aircraft. Therefore, 20 km is selected as the working altitude for the UAV in this thesis.

1.2 Climate-Sailor Mechanical Structure

In this thesis, the case study called Climate-Sailor for harvesting weather data serves as base for fixing requirements. According to the demands of the frequency of the measurement and monitoring, Climate-Sailor has to proceed with 30 m/s at 20 km operating height. Climate-Sailor is basically a machine supported glider with a wingspan of 16.24 m and a wing surface of 14.62 m^2. The structure of Climate-Sailor is shown in Figure 1.2.

1.3 Operating conditions

At a cruising speed of 30m/s, Climate-Sailor works at a height of 20 km and observes and collects information about meteorological data. It can also be used for scientific research and civilian applications. Climbing and cruise operation mode of Climate-Sailor are necessary for working out the demands on the drive. The first operation mode is climbing which covers the period when Climate-Sailor is ascending from ground level to cruising height (20 km). In order to overcome the strong wind in the troposphere, a stable weather period is necessary. Another solution is to lift the UAV by an air balloon into the stratosphere and then the UAV starts to work. The problem of peak power demand during climbing mode after UAV launching and low power requirement while cruising in good weather conditions is solved through utilization of battery modules. A Maximum Power Point Tracker (MPPT) keeps tracking the maximum power output of the solar cells regardless of varying working conditions such as incident solar radiation, shading and temperature variations.

Compared to fuel-powered aircrafts, a solar-powered aircraft presents a different design challenge; the surface area used for the photovoltaic arrays is directly affected by the size and layout of the aircraft. Apart from the power system, the heart of a renewable energy aircraft is its propulsion system. The design of the propulsion system has to meet the requirements of the three operational states during the full running mode which are take off, cruise and high winds situation. The aircraft spends the majority of its flight time in steady flight mode, i.e. constant velocity. Thus, the propulsion system should be optimized at its required operation point for steady flight. The main parameters of the electrical propulsion system for Climate-Sailor are shown in the following list.

- DC-link voltage: 270 V
- Take off speed: 10 m/s
- Climbing-up speed: 20 m/s
- Cruise altitude: 20 km

– Cruise speed: 30 m/s

– Rated output power of the electrical machine: 1.5 kW @ 8000 rpm

The conclusion of [11] certifies that in most case, high voltage DC will definitely lead to low power loss and can save cable weight in the airplane. Moreover, 270 V can be obtained directly from DC/DC converter connected to a battery as shown in [12].

High efficiency electrical motors and propellers as well as the availability of lightweight photovoltaic film cells and components for a 270 V DC power supply system greatly increases the realizability for constructing a UAV.

2 Concept of the electrical propulsion system

The architecture of a UAV system is presented here as the interaction among levels of the UAV system, including solar power supply and battery, MPPT and power management system and electrical propulsion layer, mechanical structure, high-level decision making and control of flight, user interface, physical and air-to/from-air/ground communication data-link layers.

The electrical propulsion system in a solar UAV converts electrical power to mechanical power for driving a propeller. Components of the electrical propulsion system include the power supply, motor converter, driving motor, gearbox, and a propeller. Figure 2.1 depicts the structure of the electrical propulsion system. The performance of the core parts of the energy system, i.e. the motor control strategy and the motor itself as shown in the dashed box, are investigated in this thesis.

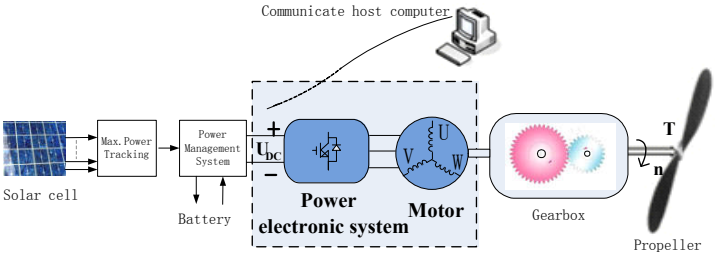

Fig. 2.1: Block diagram of the solar UAV electric propulsion system model

This thesis focuses on the development of electrical machines and power electronic system in the electrical propulsion system of Climate-Sailor UAV.

2.1 Selection of electrical machine

The efficiency and weight of the propulsion drive motor will directly affect the size and weight of the aircraft itself, the battery capacity, and the cruise duration. Therefore it is necessary to select an lightweight and efficient motor. Following motor types were discussed:

The switched reluctance machine has been addressed as a possible magnet-free alternative and offers controllable flux and zero-field coasting. Though both

the induction motor and switched reluctance motor offer the advantage of more flexibility of flux control strategy [13], they cannot offer the same absolute efficiency at maximum torque at the extremities of the speed range [14][15] at weight optimized design.

Compare to Induction Motor (IM), Permanent Magnet (PM) Motors can achieve higher efficiency and torque density. Since the squirrel cage in is not needed for PM motors, there is no rotor losses in IM. However, the current needed to meet torque requirements will increase which leads to more losses in the stator[16]. Due to small size, less maintenance and price competitiveness, PM Motors are now becoming more important for automotive and civil applications. In general, PM motors outperform conventional DC motors with better speed-torque characteristics, efficiency, longer operating life, and increased reliability. The small size reflects high torque-to-mass ratio and high power density which is extremely important to aircraft markets [17].

In Permanent Magnet Synchronous Motors (PMSM), the magnets in the rotor produce a rotating magnetic field in the stator. For the control system commonly field oriented control is applied, which is based on a rotor fixed coordinate system. Stator current is separated into direct (I_{d}) and quadrature (I_{q}) components. A common control strategy is the maximum-torque-per-ampere (MTPA) aproach, which includes the case of $I_{\mathrm{d}} = 0$ for machines that have equal L_{d} and L_{q} inductances [18]. PMSM offers good dynamic behaviour and minimum torque ripple. Therefore, PMSM with its complex control strategy is primarily applied for accurate servo systems and applications requiring smooth torque generation, such as robotics or electric vehicle drives [19].

The common strategy of controlling BLDCM has two active phases during one commutation period which is 60° wide (electrical angle). Back electromotive force (back EMF) is directly proportional to the motor speed and the developed torque is almost directly proportional to the phase current, so BLDCM have good speed regulation performance at low computational effort. Apparently, a BLDCM is the best choice for the electric propulsion system.

The Surface Mounted non-salient Permanent-magnet configuration (SMP) has been studied extensively due to its simple control strategy reasoned in equal inductances along both d and q axes [20]. However, this structure will commonly lead to larger air gaps. Further, the existence of a bandage fixing the surface magnets increases the complexity of the mechanical processing [21]. Currently, Interior Permanent Magnet configurations (IPM) feature high torque density and easier manufacturing and have gradually gained recognition [22]. In [23], one obvious benefit of utilizing an IPM rotor is that the magnets are located inside the rotor and thus the permanent magnet eddy current losses may be remarkably reduced as the flux pulsations attenuate before penetrating into the magnet material. The usual structures of SMP and IPM motors with single tooth windings are shown in Fig. 2.2.

IPM was selected in this thesis and a new IPM rotor structure with a different arrangement of the magnetic field and reduced number of magnet blocks was proposed. The comparison of the conventional structure and the proposed one will be analyzed in the 3$^{\mathrm{rd}}$ chapter.

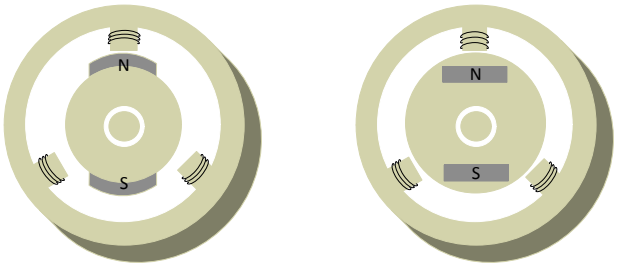

(a) SMP rotor (b) IPM rotor

Fig. 2.2: Structure of BLDC motors

2.2 Converter technology

2.2.1 Converter technology

A BLDC motor is using the electronic commutation instead of commutator and brushes in conventional DC machines. The electronic control device will process the feedback information of the rotor position and generate control signals for the power electronic switches. This eliminates failures caused by the brush as well as reduces maintenance cost.

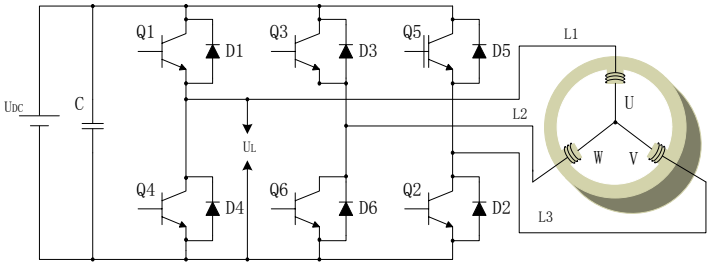

Fig. 2.3: Three phase converter topology

Compared with PMSM, a BLDC motor only requires a rotor position sensor or device to indicate the rotor position at the commutation points to drive the electronics while its starting and operating. In one 360° electrical period, a BLDC motor has 6 commutation states that last for 60° electrical each. Hence, the power devices are commutated sequentially every 60°.

Considering the cost of power-electronics converters and the requirement for the control strategy, the topology of 2-level 3-phase converter is used for this thesis. The structure is shown in Fig. 2.3. The voltage source topology requires a symmetric Pulse Width Modulation (PWM) scheme for switching control.

The turn-on and turn-off sequence is controlled through the gate signals of the semiconductors and generated by a micro-controller stage. Through 3 phase bridge semiconductor, DC power supply is transferred into AC current signals flowing in the coils.

2.2.2 Sensorless technology

For the solar UVA, the environmental conditions comprise rapid change of temperature, illumination intensity, wind force, and other uncertainties. To improve drive system stability, a sensorless control strategy based on the EMF in the disconnected coil is applied.

In order to sample the 3 phase voltages and DC voltage and transmit these signals to the micro-controller, an isolation circuit has to be applied. Galvanic isolation circuits are widely used in traditional industry, home appliance, solar renewable system, etc. Common methods are transformer, capacitive coupling and optical coupling. However, transformer and capacitive coupling are only applicable in AC circuits [24].

A commonly used isolation amplifier is the ISO122 to realize an analog transmission. This kind of the components has excellent offset, gain, accuracy and stability over time and temperature, but the bandwidth around 50 kHz can not meet the speed requirement in the present application. On the other hand, using a high stability isolated error amplifier ADUM3190 with faster transient response, renders a low accuracy of linearity.

In the thesis, a high speed, good-linearity analog isolation circuit to sample the voltages of a 270 V Brushless DC Motor to realize sensorless control strategy is proposed. The proposed linear optocoupler consists of a Light-Emitting Diode (LED) and photodiodes. [25] [26] describe the application of this analog isolation circuit with good linearity. In [27] [28], the application of a feedback signal controlling the optical flux is used to improve linearity. For increased voltage isolation requirements, optocouplers with closed loop optical transmission ssytem have been applied [27].

A fast response time of the circuit is necessary to obtain the position information from voltages with PWM. Good linearity ensures the accuracy of the voltage signals. The key concept is to combine a PI controller with fast operational amplifiers to the built-in linearizing feedback photodiode loop of linear optocoupler.

2.3 Mechanical behavior of BLDCM

The mechanical behavior of electric machine has a greater impact on the aviation application field. The vibration of the motor could lead to its structure damage and failure. Comparing with traditional application, aircraft application deserves closer attention. The vibration and noise of BLDCM with two different IPM rotor structures caused by electromagnetic force are analyzed. An analytical method was also applied and the results of modal analysis were experimentally verified to provide the hints of inherent characteristics of motor stator.

2.4 Outline

Chapter 3 presents the design procedure of two BLDCM for electric propulsion system applications.

Chapter 4 presents the comparison of simulated results and experiments of the performance of the conventional and proposed structure BLDCMs.

Chapter 5 introduces the electrical converter for two BLDCM including the proposed sensorless control strategy and the losses consumption of main electronics.

Chapter 6 mainly analyzes the acoustic behavior of BLDCM and modal analysis of the stator.

3 Electromagnetic design of the motor for the propulsion system

The main advantage of a BLDCM electric drive system is the high efficiency reducing the weight of the power supply system and therefore increasing the payload capacity of the UAV. A new structure for an IPM rotor is proposed. Both conventional and proposed machines use the same stator, but the rotors have two different IPM structures with the same rotor external diameter and shaft diameter. Compared to the conventional IPM motor, the magnetic and mechanical characteristics of the proposed IPM structure will be analyzed.

3.1 Motor specification

Based on the aircraft operation condition, both electrical and mechanical parameters should meet the following requirements:

- 270 V DC Link voltage
- Rated torque 1.8 Nm
- Rated speed 8,000 RPM
- Max. stator diameter 110 mm
- Max. motor length 120 mm
- Air cooling
- Winding isolation class H 180 °C (for lab test, in case of motor failure)

3.2 Motor design

A manual design process of the motor was executed first, then the results were simulated in SPEED anaytical software and optimized and verified in MAXWELL Finite Element Analysis (FEA) software.

3.2.1 Slot/Pole selection

In order to meet the low mass requirement, a rather high pole number motor is considered. However, the pole number is limited by a compromise between reduced mass and increased iron loss for large pole numbers [29]. Considering the complex manufacturing of high number of slots and its winding pitch of 120 degree electric angle and the fundamental winding factor $k_{\mathrm{Nm}} = 0.866$ [30] [31], the popular combination of 12 slots and 8 poles was selected.

The concentrated winding can be applied in the above configuration. Since short end-windings inherently result in low copper losses and fractional slot windings have low cogging torque than the integer slot motor with same slot/pole [32], single tooth winding configuration was used. A three phase BLDCM was chosen in this application due to reliability of the control algorithm and the cost of the power electronics [33].

3.2.2 Selection of interior vs. surface mounted magnets

Surface-mounted permanent magnets and interior permanent magnets for the rotor structure are investigated. The SPM structure is often used for the common control strategy of 2 simultaneously conducting phases and 6 commutation states [34].

As shown in Fig. 3.1, FEM simulated back EMF waveform with similar RMS values at 9,000 rpm are compared. Both, SPM and IPM motors use a conventional magnet structure with 8 magnet blocks and 8 poles. It is verified that the SPM structure has a more trapezoidal back EMF waveform. As it is stated above, the SPM structure will bring more difficulties to mount the magnets symmetrically and tightly on the rotor surface. This increases the width of the air gap and decreases the utilization of the permanent magnet.

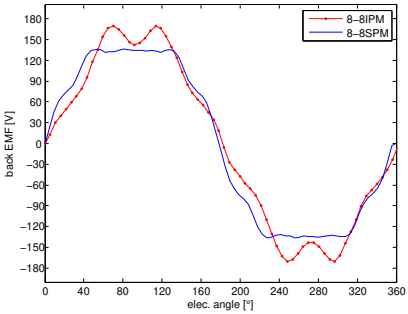

Fig. 3.1: FEM based comparison of back EMF waveforms with interior and surface-mounted permanent magnets

Different from SPM, L_{d} is usually smaller than L_{q} in an IPM motor. During phase advanced control, the average value of I_{d} during one 60° (electrical) period becomes negative, leading to an overall increase of the torque at a given current,

taking into account the negative difference of the inductance in equation (3.1) for sinusoidal currents. Considering the simplified mechanical installation and the higher torque produced by IPM structure during phase advanced control, interior permanent magnet structure is adopted [35].

$$T_{\mathrm{em}} = \frac{3}{2} p \cdot [\psi_f i_{\mathrm{q}} + (L_{\mathrm{d}} - L_{\mathrm{q}}) i_{\mathrm{d}} i_{\mathrm{q}}] \tag{3.1}$$

where T_{em} is the electromagnetic torque, p is the number of pole pairs, I_{d} and I_{q} are the respective stator current components in d-axis and q-axis direction, L_{d} and L_{q} are the respective inductances, and ψ_f is the synthetic flux linkage in the air gap.

3.2.3 Design of stator and rotor

Due to the limitation of the installation position and space in the solar aircraft, the frame dimension of the motor is fixed. The preliminary selection of frame size automatically fixes the outer diameter of the stator. The inner diameter of the stator depends on the air gap and rotor diameter. Equation 3.2 shows the analytical method to calculate the diameter of the rotor [36].

$$D'_{\mathrm{i}} = \sqrt[3]{\frac{P'}{\pi^2 \alpha_{\mathrm{i}} \frac{2}{3} \hat{A}'_{\mathrm{s}} B'_{\delta} \lambda n_{\mathrm{N}}}} \tag{3.2}$$

where,

α_{i}: pole arc coefficients

$\hat{A}'_{\mathrm{s}}$: peek value of current loading (A/m)

B'_{δ}: flux density in the air gap (T)

D'_{i}: the rotor diameter

λ: the ratio of motor length L_{stk} and rotor diameter D'_{i}

P': rated power/motor efficiency

n_{N}: rated speed

In the equation, the size of the motor depends on A'_{s} and B'_{δ}. By increasing the value of A'_{s} and B'_{δ}, the motor size can be reduced.

For PM motors, an important parameter for the B'_{δ} value is the characteristic of the magnetic material itself, e.g. NdFeB has typically a residual flux density of 1.2 – 1.3 T at 20 °C and Ferrite magnets have smaller flux densities of 0.2 – 0.4 T. In order to obtain a larger flux density in the air gap, NdFeB is selected but the cost will increase. However, higher B'_{δ} will increase the saturation in the stator and rotor core, specially in the teeth area. Since the iron losses are approximately proportional to the square of the flux density, a higher B'_{δ} will lead to a temperature rise of the motor.

The current loading $\hat{A}'_s$ is defined as in equation 3.3:

$$\hat{A}'_s = \frac{N_c Z \hat{I}}{\pi D'_i} \tag{3.3}$$

where

N_c: the number of turns per slot

Z: the number of slots

$\hat{I}$: peak value of the phase current.

The current loading describes the number of winding conductors along the rotor circle. Higher A'_s values will lead to a higher risk of irreversible demagnetization of the rotor's magnets resulting in deterioration of the working characteristics of the motor. If the current density of the winding is kept constant, a higher A'_s leads to an increase of the number of the wires in the slot resulting in increasing copper consumption, copper loss and temperature rise. If the dimension of the tooth width is constant, a higher B'_δ will lead to high tooth flex density B'_T. Since the frequency of the motor is rather high, maximizing B'_δ is not recommendable. The winding insulation class H is selected, so higher A'_s is allowed to keep the motor size small. Moreover based on the magnetic characteristic of NdFeB magnet material, the values are chosen as follows:

$\hat{A}'_s = 36\,A/mm$

$B'_\delta = 0.6\,T$

Considering the cost, silicon-iron M270-35A was selected as the lamination material of the stator and rotor [37]. The mechanical values of the stator and rotor parameters are shown in Tab. 3.1.

Tab. 3.1: Dimensions of the stator and rotor design

stator radius	air gap	rotor radius	motor length	tooth width
R_s	δ	R	L_{stk}	T_w
45 mm	0.5 mm	30 mm	59.85 mm	5.6 mm

3.2.4 Design of stator teeth

Theoretically the working point should be assumed to be operating at a flux density above the knee value obtained from the B-H characteristics of the magnet. Considering the size and width of flux path, the values of the flux density located in different parts of the stator are certainly different. It is obvious that the greater flux density happens at the stator teeth and rotor bridge area. The structure of the slots in the stator is shown in Fig. 3.2.

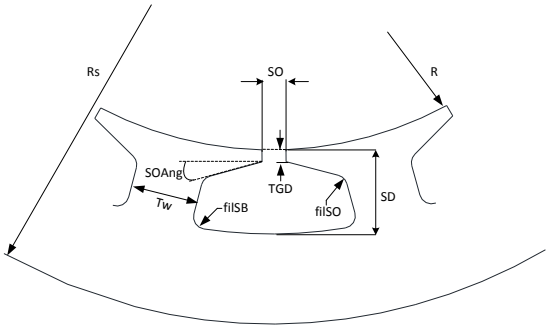

Fig. 3.2: Stator dimensions

3.2.5 Design of interior permanent magnetic structure

In this part, the proposed magnet arrangement will be introduced. Both BLDCMs use the same stator, but the two rotors have different IPM structures with the same rotor external diameter and shaft diameter. The conventional rotor utilizes 8 magnet blocks for 8 poles and will be denoted '8-8' throughout this document. In the proposed IPM structure, there are only 4 magnet blocks for 8 poles and therefore it will be referred to by '4-8'. To achieve this behavior, the magnetization direction "South pole" of all magnets in the proposed structure point to the rotor center. The aforementioned preliminary analysis results of the two rotor structures are shown in Fig. 3.3.

3.2.5.1 Determination of magnet dimension

Compared to ferrite magnets, the rare earth magnets such as Samarium-Cobalt ($SmCo_5$) and NdFeB feature much higher specific energy. Vacodym 655 HR NdFeB is selected due to its high specific energy and high temperature resistance capability, and for economic reasons. The parameters of 655 HR NdFeB are shown in Table 3.2.

Tab. 3.2: Parameters of magnet material Vacodym 655 HR

Remanence	Coercitivity	Temperature coefficient $TK(B_\mathrm{r})$	
B_r	H_CB	$20-100\,^\circ\mathrm{C}$	$20-150\,^\circ\mathrm{C}$
1.28 T	990 kA/m	$-0.090\,\%/^\circ\mathrm{C}$	$-0.100\,\%/^\circ\mathrm{C}$

In order to compare the performance of the two motors, both shall generate the same RMS value of the back EMF voltage in the stator winding. Since there is

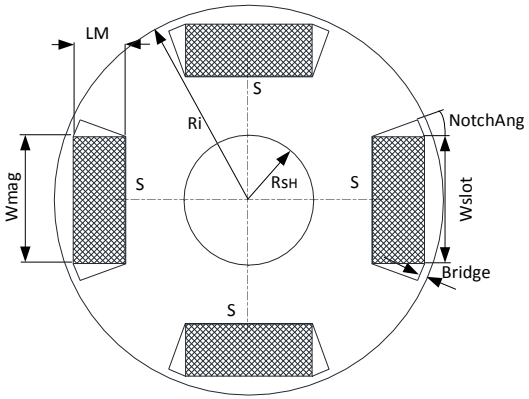

(a) Proposed '4-8'-rotor structure with 4 magnet blocks and 8 poles

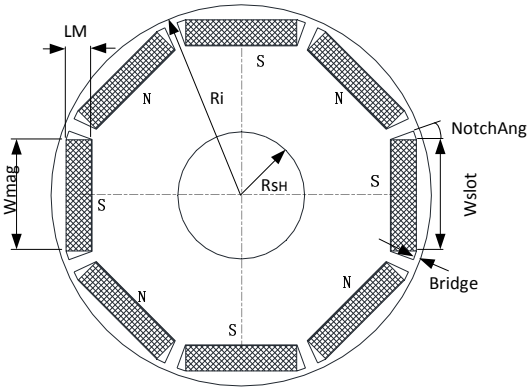

(b) Reference '8-8'-rotor structure with 8 magnet blocks and 8 poles

Fig. 3.3: Comparison of the two rotor geometries

only one magnet block per pole pair in the magnetic circuit of the proposed magnet structure, the magnet thickness increases to 2 times of the magnet thickness of the conventional structure. From Tab. 3.3 can be seen, that the simple construction with 4 magnets only leads to an increase of magnet volume by 11.4 %. From the mechanical point of view, the proposed rotor structure has a simpler installation procedure.

Tab. 3.3: Dimension of magnet design

magnet blocks	pole pairs	LM	W_mag	magnet length	bridge
4	4	8 mm	19.5 mm	59.85 mm	1.2 mm
8	4	4 mm	17.5 mm	59.85 mm	1.0 mm

3.2.5.2 Demagnetization behavior

Irreversible demagnetization of permanent magnets has to be avoided. It is ususally caused by armature overcurrent, excessive temperature or unexpected operation conditions. When irreversible demagnetization occurs, the flux density of PM is permanently degraded. Output power and torque may not satisfy the operation condition and can lead to serious problems [38]. Two reasons of irreversible demagnetization are increases in temperature or armature reaction.

Many researchers investigate the influence of the internal characteristics of PM synchronous motors on irreversible demagnetization. The main reason for irreversible demagnetization is an over current due to short circuit, locked state of the motor, over load, or winding short fault [39].

Large short current caused by inverter faults, is one of the most common reason for the demagnetization. If this situation is caused by the hardware failure, the damage of the system is irreversible. The aircraft can not work back to the state of cruise and will drop down. The software failure will produce large short circuit current which will lead to irreversible demagnetization. Therefore, in this case the short circuit situations are limited by the protection strategy of the power electronics system. The other fault of the drive system, which causes air crash, is a three phase short circuit.

The most challenging operation point occurs when the motor runs at overload situation. Since the motor has to continue to cruise even when overload situation occurs, the effect of demagnetization under overload situation will be analyzed by FEA in section 3.3.5.

3.2.5.3 Bridge design

The bridge is the mechanical weak point in the rotor part due to interior permanent magnet structure. The thickness of the bridge determines the behavior of the leakage flux, thus the magnetic performance is strongly affected [40]. A thicker bridge will result in better ability to stand the centrifugal force which is proportional to the square of the rotating speed, depicted in equation 3.4. At the

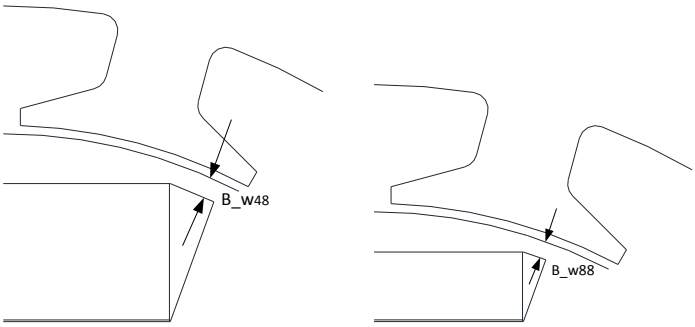

(a) 4 magnet blocks (b) 8 magnet blocks

Fig. 3.4: Bridge structure in the rotor

same time a thicker bridge will lead to an inferior electromagnetic characteristic due to an increased leakage flux.

$$F_{\text{cen}} = \frac{mv^2}{r} \tag{3.4}$$

where F_{cen} is centrifugal force, m is mass, v is rotating speed and r is the radius of the rotating mass. The maximum centrifugal force occurs at 120 % of the highest speed in the application.

Different types of bridges have been studied recently, e.g. H-bar, dual bridge or V-shape IPM [41] [42]. Although the dual bridge has less leakage flux, this type increases the machining difficulty. In this thesis the simple I-bar bridges were used for both rotors. The structures are shown in Fig. 3.4. It is very common to arrange holes or cut-outs in the rotor yoke and in proximity to the bars, e.g. in V-shape magnet arrangements, to increase the stiffness of the rotor core and optimize flux leakage. Considering the rotor diameter and the available space around the bridge in the design, holes or cut-outs are neglected for this thesis.

In the PM rotor, the centrifugal forces are generated in the radial direction and the electromagnetic forces are dominantly also in the radial direction of the rotor. But the attraction forces due to the permanent magnets have opposite direction against these two forces, which are vertical to the boundary of the magnets. Based on the different interaction forces, the FEA analysis of the mechanical stress distributed on the different rotor structures will be presented in the following section 3.3.3.

3.2.6 Winding design

The fractional slot winding with a non overlapping concentrated winding was chosen due to its short endwindings and high efficiency [43] [44]. In this thesis a 3 phase motor with single tooth winding is used. Fig. 3.5 shows the EMF vector diagram of the slots which are 120° apart from each other. Fig. 3.6

shows mechanical connection of coil sides for the 3 phases. The numbers (first layer) and the number with apostrophe (′) (second layer) denoted at each phase represent the slots to be used for the corresponding phase.

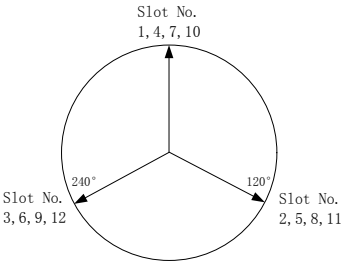

Fig. 3.5: Star of slots

The details about the harmonic orders in the stator's MagnetoMotive Force (MMF) are shown in Fig. 3.7. 4^{th} order is equal to the numbers of pole pairs and is the fundamental waveform. MMF has 2^{th}, 4^{th}, 5^{th}, 7^{th}, 8^{th}, 10^{th},and 11^{th} harmonics component.

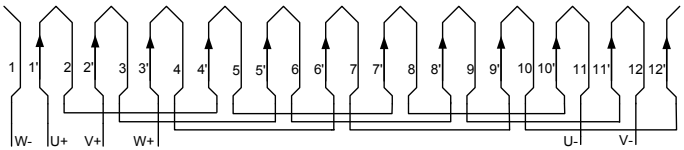

Fig. 3.6: Winding layout

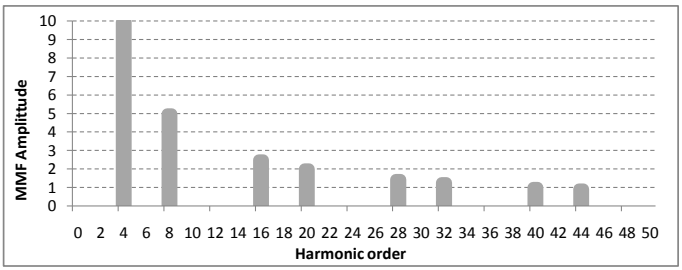

Fig. 3.7: Spatial harmonics due to winding distribution referred to rotational speed

A slot fill factor of 35 % is considered to allow for the winding's mechanical processing. For the rated electric current density J_{N} a rather high value was

chosen, considering forced air cooling. This high value is necessary to satisfy the demanded small size of the motor.

$$J_{\mathrm{N}} = 13.5\,\mathrm{A/mm^2} \tag{3.5}$$

3.2.7 Design of the Hall effect sensor circuit

The method of rotor position detection of BLDCM to control the inverter transistors can be classified into two categories. One method is using Hall effect sensors [45] [46] [38]. The other one is the sensorless approach which is commonly using the back - EMF zero - crossing method [47] [48] [49]. Considering the dynamic states, especially start - up, and the simplicity of the implementation, Hall effect sensors were included in the design and the corresponding method was used to verify the design of the motor. The isolation circuit for the sensorless control strategy will be investigated in section 5.2.

3.2.7.1 Principle of commutation

The commutation signals for BLDCM are only required every 60° electric angle. Encoders can provide more precise position information for sinusoidal control but come at a higher price. For the implemented 6 commutation state control method encoders are not necessary. Therefore a Hall effect sensor circuit was chosen for position sensing.

Two different Hall effect sensor circuit options will be described here. In order to save the cost of additional magnets and the compactness of the motor structure, one method is to sense the magnetic field of the rotor directly by the Hall effect sensors. However, due to the armature effect, the distortion of the magnetic field could reduce the accuracy of output signals of Hall sensors. On the other hand, insufficient space between the stator stack and end-plate of the housing limit the feasibility of this approach. As an alternative, an external magnet disc was mounted to the shaft. For a correct angular placement of the individual Hall effect sensors, a corresponding PCB has been designed.

3.2.7.2 Distribution of Hall effect sensors for fractional slot armature windings

The output signals of 3 Hall effect sensors H1, H2 and H3 are used to indicate which of the motor's phases to use for generating torque in the current rotor position. Thus, a change in one of the signals can be used to trigger the commutation from one phase to the next by selecting a different set of active transistors. The number and allocation of the Hall sensors should satisfy this demand. According to equation 3.6, using $p = 4$ pole pairs, the mechanical angle θ_{m} between each of the phases in the symmetric 3 phase system is 30°, thus three Hall sensors are selected and located at 30° mechanical angle from each other.

$$\theta_{\mathrm{m}} = \frac{\theta_{\mathrm{e}}}{p} \tag{3.6}$$

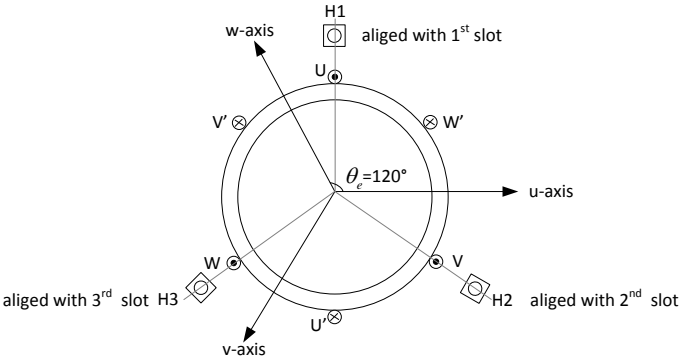

Fig. 3.8: Location of Hall sensors corresponding to stator slot

Where θ_e is the electric angle. The three Hall sensors are displaced by a mechanical angle of 30° from each other and are aligned to the center line of corresponding slots, as shown in Fig. 3.9.

As it is shown in Fig. 3.9, the magnet ring plate should provide magnetic fields which are perpendicular to the surface of the Hall sensors. The 4 North and 4 South poles of the Ferrite magnets are arranged alternately to produce an 8 - pole alternating perpendicular magnetic field around the circumference of the magnetic ring. For the mechanical construction an iron plate for magnets installation was used. Then 8 precut parts of rubber compound ferrite magnets were glued into this groove. The iron plate also provides the return path for the magnetic flux.

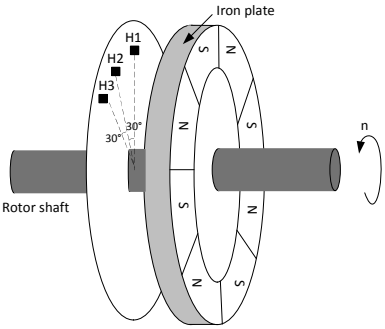

Fig. 3.9: Mechanical installation location of Hall sensors and exciting magnetic field

The sensor's output will become 'high', when a North pole of sufficient strength is placed above the sensor. Correspondingly a South pole will lead to a 'low' output. From Hall sensor data sheet, the rise time and fall time of output signals is 400 ns [50]. When the motor runs at 9000 rpm, the delayed electric

angle caused by the these times is 0.0864°. By rotating the magnet plate with motor shaft, the combination of Hall signals will indicate the position of the rotor from 0° to 360° electric angle in steps of 60°. The output signals of the 3 Hall sensors according to the rotor position are shown in Fig. 3.10.

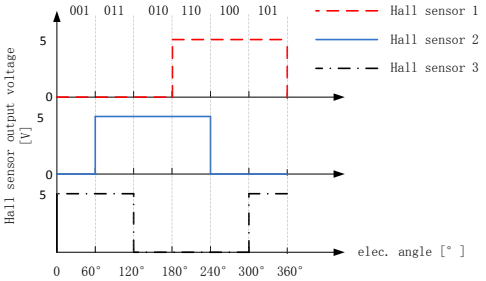

Fig. 3.10: Output signals of Hall sensors for one electrical period

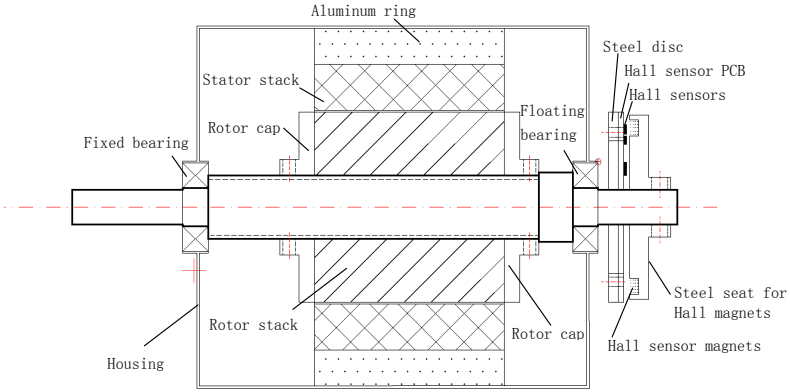

Fig. 3.11: Motor structure in cross sectional view

3.2.8 Structure of the motor

The cross section of the designed BLDCM is shown in Fig. 3.11. It contains most mechanical parts of the motor which are stator and rotor stacks, shaft, two bearings and the Hall sensor assembly for position sensing.

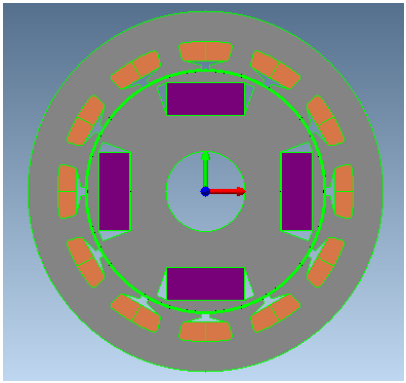

(a) 4 magnet blocks

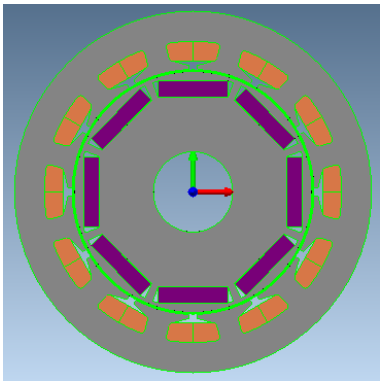

(b) 8 magnet blocks

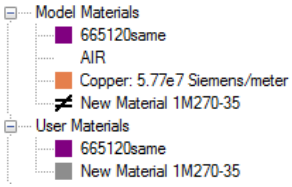

(c) material

Fig. 3.12: Geometry of the 2 motors for FEM analysis

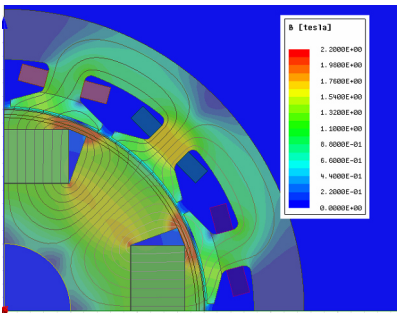

(a) 4 magnet blocks

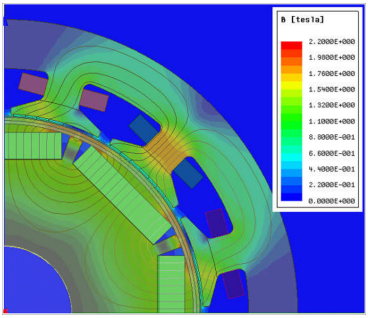

(b) 8 magnet blocks

Fig. 3.13: Distribution of magnetic flux density(at 0° elec. angle)

3.3 Verification of the design by FEA and test

Once all the parameters have been determined, the motor has to be verified by FEM analysis. This section presents the result of FEM analysis for the basic parameters of the two BLDCMs. Particular attention was paid on the comparison of the two motors' performances; the influence of different factors on the parameters were also analyzed.

The 2D machine geometry was built up and imported into FEA software and all energetically active parts of the machines were assigned with the specific material properties, as shown in Fig. 3.12.

3.3.1 Flux density

Fig. 3.13 shows the results of the static no-load magnetic field simulation of the two motors. For the proposed 4-8 IPM structure, the rotor also produces 8 poles as does the reference 8-8 design.

A comparison of the air-gap flux densities B_δ, calculated by SPEED and FEM software, will be shown first to undermine the necessity for FEM calculations. In Fig. 3.14, the distribution of $|B_\delta|$ along the air-gap is shown for one electrical period. The calculation was performed in SPEED software based on analytical formulae and in FEM software for the proposed 4-8 BLDCM with 4 magnet blocks. It is obvious that the motor design software SPEED 9.1 using quasi analytical calculations is not able to predict flux densities accurately. Therefore simulated values to verify the design have been calculated by FEM software in this thesis.

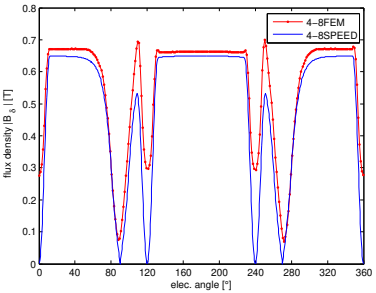

Fig. 3.14: Comparison of the absolute air-gap flux density $|B_\delta|$, calculated by FEM and SPEED software for the 4-8 BLDCM

After the dimensions of the motor were imported and the material properties were assigned, static analysis was conducted in ANSYS. In Fig. 3.15 the distribution of the absolute air-gap flux density $|B_\delta|$ is shown for the proposed and the reference design.

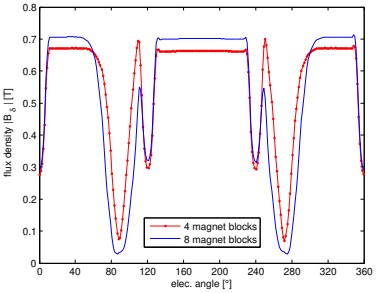

Fig. 3.15: Comparison of the absolute air-gap flux density $|B_\delta|$, calculated by FEM software for the proposed 4-8 and the reference 8-8 BLDCM

The average flux density in the air gap is 0.558 T and 0.533 T for BLDCM with 4 magnet blocks and 8 magnet blocks, respectively.

3.3.2 Back-EMF waveform

Both rotors are designed to induce the same RMS values of the back-EMF voltage in order to make the performance of two motors comparable. The other important consideration is to reduce the 2_{nd} harmonics order for the proposed motor structure. The simulated back-EMF waveforms at a speed of $n = 9000$ rpm are shown in Fig. 3.16. Obviously, the two rotors have a similar back EMF voltage form.

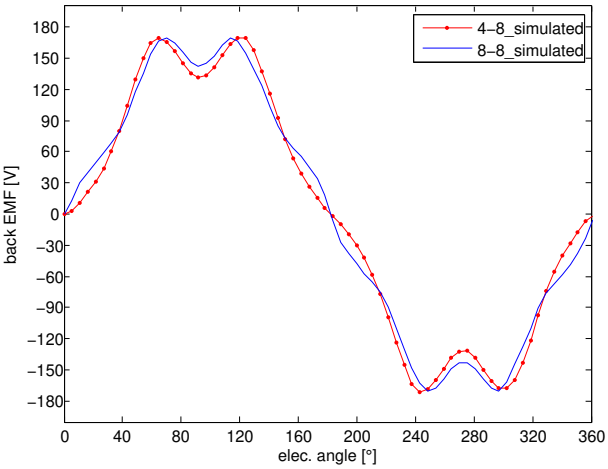

Fig. 3.16: Simulated back-EMF at 9000 rpm

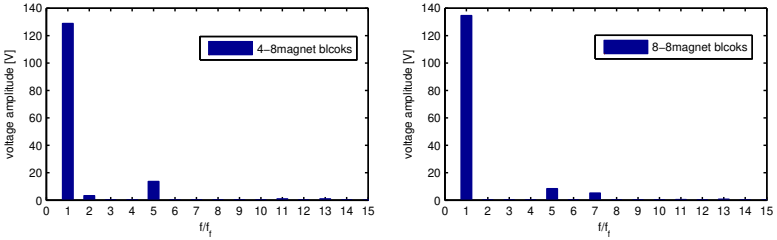

(a) 4 magnet blocks (b) 8 magnet blocks

Fig. 3.17: EMF harmonics at 9000 rpm

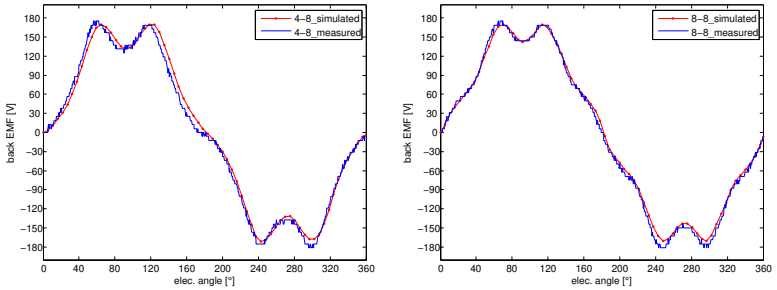

(a) 4 magnet blocks (b) 8 magnet blocks

Fig. 3.18: Comparison of back-EMF voltage, simulated and measured waveform

Through FFT data processing, the harmonic orders contained in the back-EMF waveform were calculated and are shown in Fig. 3.17. Both structures develop a 5^{th} harmonic, but for the 8-8 design it is considerably higher. For the 4-8 BLDCM the 7^{th} order harmonic is almost invisible but a 7^{th} order harmonic is introduced.

The experimental back-EMF waveforms of both IPM machines correspond well to the simulation results shown in Fig. 3.18. According to Table 3.4, the measured RMS values of the back-EMF voltage for both structures are larger than the simulated values: 1.4 % increase for the 4 magnet blocks design and 3.7 % increase for the 8 magnet blocks design. This is assumed to be mainly due to the different operating temperature of the magnets. In FEM simulation, the magnet temperature was set to 120 °C. However, during the experimental test, the magnet temperature must be assumed to be close to the ambient temperature.

Tab. 3.4: Comparison of back-EMF voltage values for simulated and measured values

	4 magnet blocks	8 magnet blocks
FEM simulated value	115.0 V_{RMS}	115.4 V_{RMS}
Experimental value	116.6 V_{RMS}	119.9 V_{RMS}

3.3.3 Mechanical stress of the bridge

The mechanical stress inside the two rotors, especially around the bridge parts, was analyzed in FEM. In order to ensure that the magnets can be properly inserted to the magnet slot in the rotor, a dimensional tolerance between permanent magnet and rotor core of 0.1 mm is reserved. Commonly, this space is filled with industrial adhesive to increase the solidity between the magnet and the rotor core. With time elapsing, the bonding strength could become weaker though.

Many publications only studied the mechanical characteristic of a 2D rotor model. It is common that the effect of shaft dynamical forces is neglected [51]. For this thesis 3D rotor models with shaft mechanical characteristics were set up. Mechanical transient analysis was carried out in ANSYS Workbench. Two boundary conditions were applied as follows: transient rotation velocity; cylindrical support for two bearings.

Since the centrifugal force is depending on speed, the maximum value of stress occurs at the speed of 10800 rpm corresponding to the usual overspeed calculation of 120 % idle speed 9000 rpm. Fig. 3.19 and Fig. 3.20 show the simulated mechanical stress distribution from the FEM analysis. In both rotor structures, mechanical stress is concentrated on the corner around the bridge. The maximum values are 56.47 MPa and 66.66 Mpa for conventional and proposed rotor, respectively.

Therefore, maximum stress in the bridge is much lower than the yield strength (450 Mpa) of the rotor core material. From these numbers it can be seen that the bridge design has enough allowance.

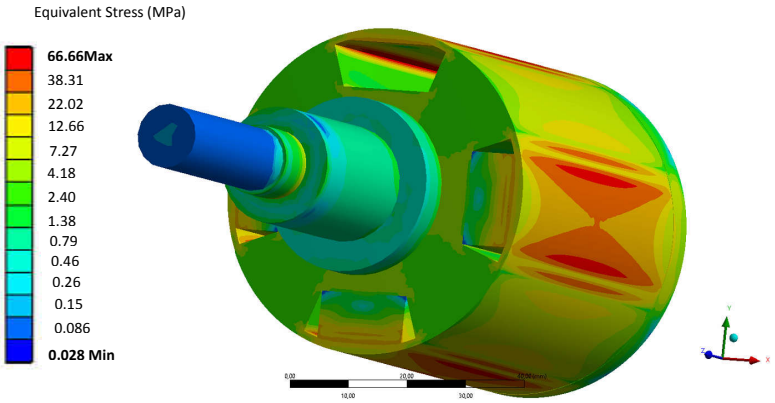

Fig. 3.19: Equivalent stress of rotor with 4 magnet blocks at 10800 rpm

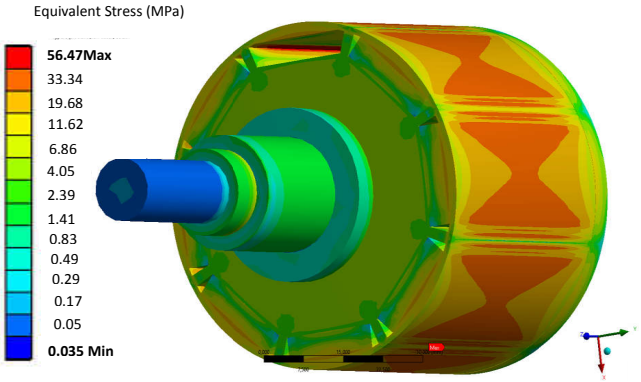

Fig. 3.20: Equivalent stress of rotor with 8 magnet blocks at 10800 rpm

3.3.4 Inductance study

The analysis of the inductance characteristics for the two motors is important and necessary for the investigation of the control strategy. Several inductance studies based on different rotor structures were analyzed, such as flat-shaped IPM, V-shaped IPM [52] and U-shaped IPM [53].

3.3.4.1 Influence of rotor position on inductance

An AC inductance test at rated frequency is widely used for determination of the inductance [54] [55] [56]. In order to realize this method, the rotor shaft is locked to eliminate back EMF content and V and W phase armature windings were connected in parallel and linked to the U winding in series. Through above method, an inductance L can be derived from the voltage equation of the BLDCM, as follows in equation (3.7):

$$L = \frac{2}{3} \frac{\sqrt{\left(\frac{U_1}{I}\right)^2 - R^2}}{2\pi f} \tag{3.7}$$

where U_1 and I are RMS values of injected voltage and current, respectively. R is the total resistance of the windings in this connection. f is the frequency of the injected voltage. The inductance L can be thought to be the stator-side inductance of one phase, but taking the mutual inductances into account.

Fig. 3.21 shows the principle circuit connection of the AC standstill test. An AC current is selected in relation to the rated current. This current is injected at a fixed frequency and the voltage is measured. To measure the inductance at different rotor angles, the locked rotor position can be varied by an indexing head in steps of 1° mechanical angle.

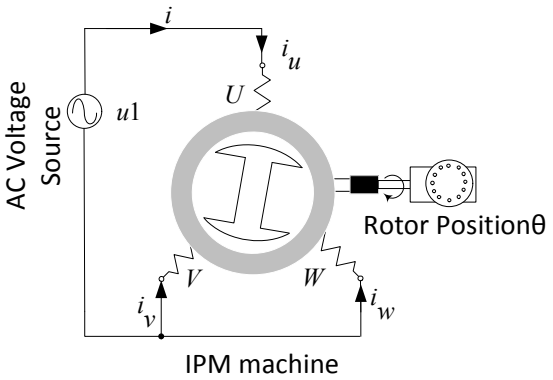

Fig. 3.21: Schematic diagram for inductance measurement

The test was done by applying the circuit setup as in Fig. 3.21. By changing the position of the locked rotor, the inductance was calculated for each rotor position. The AC-current of $2\,\mathrm{A_{RMS}}$ is about 44 % of the rated current. It was injected at rated frequency of 533 Hz.

Fig. 3.22 depicts the variation of the absolute inductance during one mechanical revolution in the experiment. The inductance of the conventional IPM machine has 45° mechanical symmetry, as shown in Fig. 3.22(b). The maximum inductances occur in the q-axis. Analogously, the minimum values correspond to the

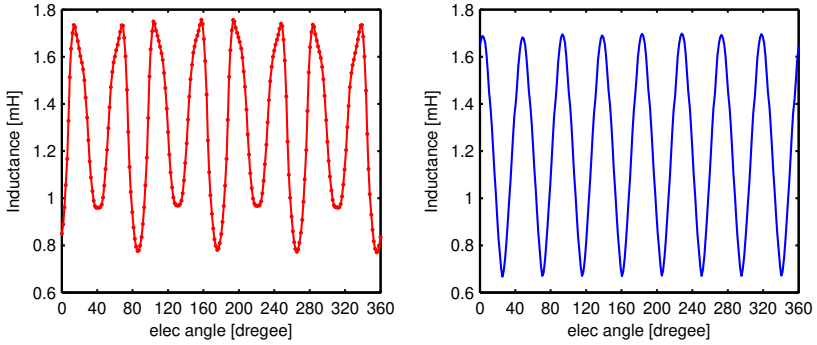

(a) 4 magnet blocks (b) 8 magnet blocks

Fig. 3.22: Measured inductance with rotor position

d positions. For the conventional IPM machine, L_d and L_q are equal for all poles.

The proposed IPM machine with 4 magnet blocks shows a 90° mechanical symmetry as in Fig. 3.22(a). The q inductances is still equal for all poles, but in the d axis 2 different values occur depending on the rotor position. The lower L_d corresponds to a position, where the magnets are aligned with the stator teeth. The higher L_d value occurs when the axes of the magnets are aligned with the slot instead.

The value of the inductance is influenced by the current magnitude which flows through the coils. In order to study the effect factors on the d and q inductance, the following analysis was conducted.

3.3.4.2 Effect of the saturation on L_d and L_q

The voltage equation of the motor can be expressed as in equation (3.8). In this equation, $\boldsymbol{L}$ depends on the rotor position. To remove this dependency, unsymmetrical machines are best described in a rotor oriented dq-coordinate system. The accuracy of L_d and L_q will further affect control precision. The voltage equations in the dq-coordinate system for a PM rotor with a locked rotor are given in equation (3.9).

$$\vec{u} = \vec{i}R + \boldsymbol{L}\frac{d\vec{i}}{dt} + \frac{d\vec{\psi}_R}{dt} \tag{3.8}$$

Where $\vec{u}$ is the phase voltage, $\vec{i}$ is the phase current, and $\vec{\psi}_R$ is the flux linkage of the rotor.

$$\begin{aligned} u_\mathrm{d} &= i_\mathrm{d}R - \omega L_\mathrm{d} i_\mathrm{q} \\ u_\mathrm{q} &= i_\mathrm{q}R + \omega L_\mathrm{d} i_\mathrm{d} + \omega\psi \end{aligned} \tag{3.9}$$

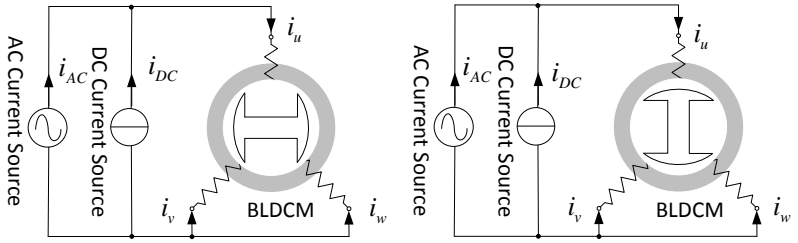

(a) L_q measurement at aligned q-axis (b) L_d measurement at aligned d-axis

Fig. 3.23: d and q inductance test setup

Where ud and u_q is the synchronous direct and quadrature voltage, respectively. i_d and i_q is the synchronous direct and quadrature current, respectively. L_d and L_q is d- and q-inductance, respectively.

As the d and q voltage in equation (3.9) shows, the d-inductance can be easily calculated when the q-axis current is 0, and therefore the voltage U_q also becomes 0.

$$L_\mathrm{d} = \frac{2}{3}\left.\frac{\sqrt{\left(\frac{U_1}{I}\right)^2 - R^2}}{2\pi f}\right|_{\text{d-axis } \| \text{ phase U-axis}} \tag{3.10}$$

Likewise, the q-inductance can be calculated when the d-axis current becomes 0.

$$L_\mathrm{q} = \frac{2}{3}\left.\frac{\sqrt{\left(\frac{U_1}{I}\right)^2 - R^2}}{2\pi f}\right|_{\text{q-axis } \| \text{ phase U-axis}} \tag{3.11}$$

where U_1 is the RMS value of the AC voltage and I is the RMS value of the AC current.

After turning the rotor by an electrical angle of 90°, the stator phase U axis is aligned with the q-axis, therefore the d- axis current component of the current will be 0. Since the stator system is aligned with d- and q-axis respectively, it is sufficient to inject a simple AC current to the three-phase winding system.

In this section, the saturation effect on the inductance value will be investigated. The saturation occurs because of the change of the flux in the direction of d- and q-axis. The study of the differential and absolute inductances is essential for a high performance control system [57].

By varying the current about a working point, the differential d- and q-axis inductances L_diff at different currents can be calculated from equation (3.12).

The FEM simulated results of the influence of DC bias current on L_d and L_q are shown in Fig. 3.26.

$$L_{\text{diff}}\big|_{I=\frac{I_1+I_2}{2}} = \frac{\Delta\Psi}{\Delta I} = \frac{\Psi_1 - \Psi_2}{I_1 - I_2} \tag{3.12}$$

where $\Delta\Psi$ is the difference of flux linkage generated from two different currents I_1 and I_2 in FEM.

In this section only the effect of saturation on the larger L_d value in the motor with 4 magnet blocks was analysed for the proposed motor.

The simulated d-axis inductance of the machine with the 4 magnet blocks rotor is larger compared to the conventional rotor structure, which is 1.11 mH and 0.80 mH respectively, as shown in Fig. 3.26(a). The possible reasons for the significantly different behavior in d-axis direction may be explained as follows: since in one magnetic circuit the thickness of the magnets are the same for both rotor, it should have not effect. But the wider magnet span in the 4 magnet blocks configuration increases the cross sectional area and therefore it reduces the magnetic reluctance, thus a larger value of L_d is obtained. As it is observed from Fig. 3.26(a), L_d decreases along with an increasing d-axis bias current. Fig. 3.26(b) shows that the characteristics of q-axis inductance L_q are symmetric to q-axis bias current for both motors. With increasing absolute value of the q-axis DC bias current, the q-inductances of both motors saturate softly when the rated current of 7.5 A is exceeded.

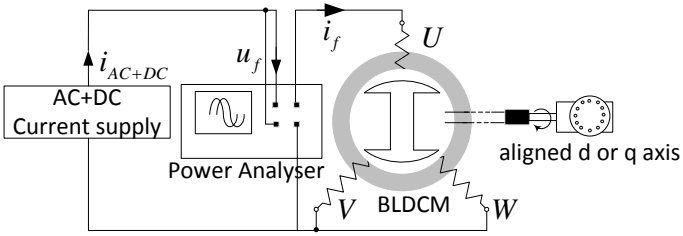

Fig. 3.24: Schematic block for inductance measurement

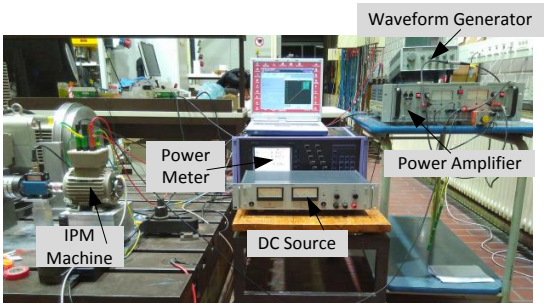

Fig. 3.25: Test setup for differential inductance measurement

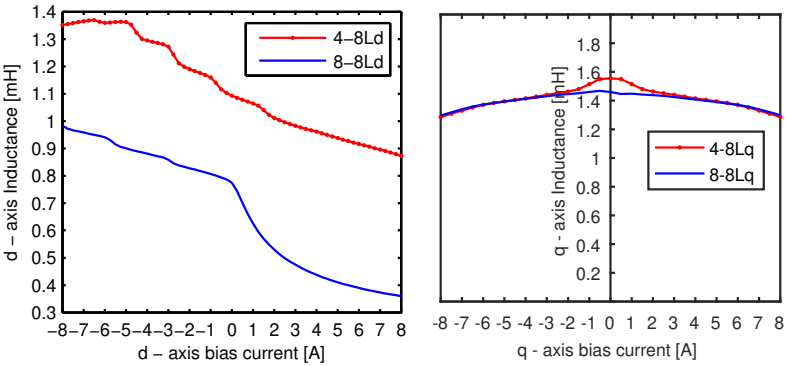

(a) d differential inductances (b) q differential inductances

Fig. 3.26: Simulated d and q differential inductances

In order to verify the FEM results, a test setup to analyze the bias effect on d- and q-axis inductance was built, as shown in Fig. 3.25. The functional principle of the circuit is shown in Fig. 3.24. To eliminate the effect of AC current component during the test, RMS value of AC current is set as 0.1 A. The frequency is set to the rated frequency 533 Hz. Different d- and q-axis DC-bias currents were applied to extract the characteristic of the differential inductances. For this investigation the currents flowing into the stator coils do not just contain an AC current component but also a DC current. Therefore an AC current and a DC current supply were connected in parallel and connected to the stator winding terminal of the machine. A power analyser was used to measure the fundamental RMS terminal voltage U_1 and current I_1 across the connected coils, the frequency of the AC signal, and also the resistance of the circuit at different DC bias currents. L_d and L_q are consequently calculated from these quantities.

Fig. 3.27 shows the measured results of the differential d- and q-axis inductance. The simulation results and test results of L_d have the same variation trend as shown in Fig. 3.27(a), but the differences of the simulated and experimental d inductance may be caused by the temperature difference of the magnets for simulation and test.

Fig. 3.27(b) shows the measured results of the differential q-axis inductance. The simulation results and test results have a similar variation trend. The differences of the simulated q inductance are about 1.5 % from the experimental values.

The comparison of simulated and measured values of L_d and L_q are shown in Table 3.5. The difference may be caused by inaccurate extrapolation of the magnetizing curve of the silicon steel sheets when B is exceeds 1.8 T which is the maximum value given in the datasheet. Also, the the FEM simulation was conducted in 2D and therefore the magnetic effects of the end windings were neglected. In conclusion, the proposed rotor structure with 4 magnet blocks has a larger L_d, but L_q values of both motors are comparable.

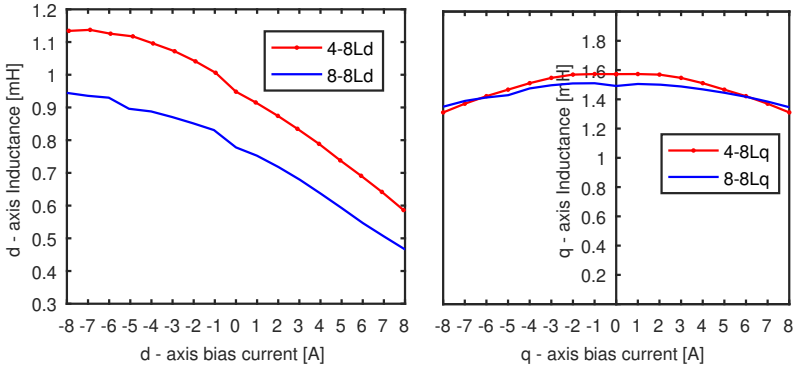

(a) d differential inductances (b) q differential inductances

Fig. 3.27: Measured d and q differential inductances

Tab. 3.5: Comparison of inductance

Inductance	Rotor type	FEM result	Measurement	Difference
L_d	4 magnet blocks	1.12 mH	0.92 mH	+22 %
	8 magnet blocks	0.81 mH	0.78 mH	+3.8 %
L_q	4 magnet blocks	1.44 mH	1.57 mH	-8.3,%
	8 magnet blocks	1.55 mH	1.49 mH	-4 %

3.3.5 Demagnetization analysis

During the climbing stage of the solar powered UAV, the drive system should be able to withstand overload situations when there are strong winds. Therefore, the power electronics system was designed to work under this overload situation. The other point necessary to consider is the demagnetizing effect of an overload current on the permanent magnets. The current waveform during the overload operation is shown in Fig. 3.28. The RMS value of the overload current is 15 A, which is 2 times the rated current.

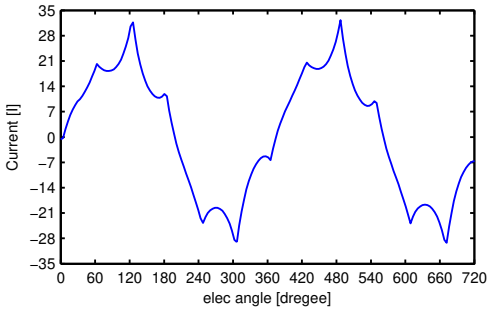

Fig. 3.28: Phase current waveform at overload situation

When a 3 phase short circuit happens, the short current at d axis calculated from the d-inductance, q-inductance and flux linkage is 38 A. It is larger than the overload current, so the effect of the short circuit current on demagnetization behavior was analysed.

Fig. 3.29 shows the influence of the temperature on the flux density and polarization for Vacodym 655 HR. When the value of the magnet field is below -800 kA/m, the magnet will produce irreversible demagnetization working at exactly 120°C.

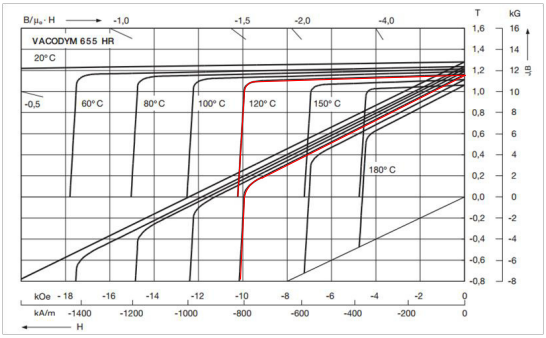

Fig. 3.29: Demagnetization curve of Vacodym 655 HR (Flux density and polarization at different temperatures)

Under this situation, the magnet field of the magnet are shown in Fig. 3.30 and Fig. 3.31 for the motor with 4 magnet and 8 magnet, respectively.

As it is shown, the irreversible demagnetization area only has small effect the edge of the magnet marked as dark blue color for the short circuit situation. Therefore, the overload current will not cause large scale of the irreversible demagnetization. Both motors could sustain it and work back to normal operation.

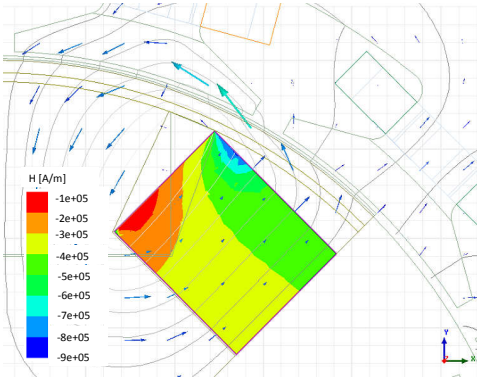

Fig. 3.30: Demagnetization behavior in 4-8 motor short circuit situation

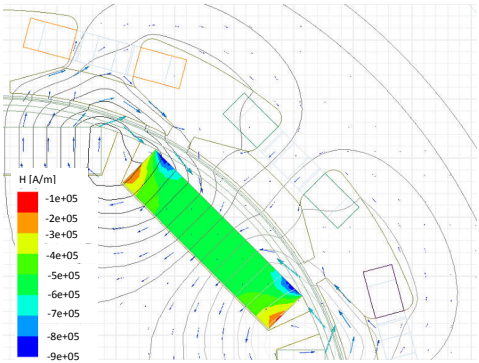

Fig. 3.31: Demagnetization behavior in 8-8 motor short circuit situation

3.4 Summary of the design

In this chapter, the design of a 1.5 kW, 3 phase BLDC machine with two different magnet structures for the rotor has been introduced. The magnet structures, stator core, stator winding connection, and air gap were optimized by three principles. The first requirement was a high torque density performance. Secondly both motors should have the same back EMF voltage. The third one was to reduce cost by rational use of permanent magnet material.

After the geometric design of the motor, FEA validation was conducted to analyze the parameters of both BLDCMs. In this analysis the mechanical performance of the bridge structure was verified in FEM analysis. Then the demagnetization behavior of both IPM structures was analyzed. Finally, an AC+DC standstill frequency test method was applied to both IPM structures, to determine values for L_{d} and L_{q}, and the influencing factors on the inductance values were studied and tested.

4 Test and verification

This chapter describes the tests carried out and an evaluation of the performance of both rotors. The basic characteristics of the motors were already shown in preceding chapters, such as inductance behavior and mechanical properties. This chapter focuses on the operating characteristics of the motors. Results of no load tests, different load operating points, an efficiency analysis, and thermal tests will be presented.

4.1 Description of the test bench

A test bench was built to carry out the static and dynamic tests, as shown in Fig. 4.1.

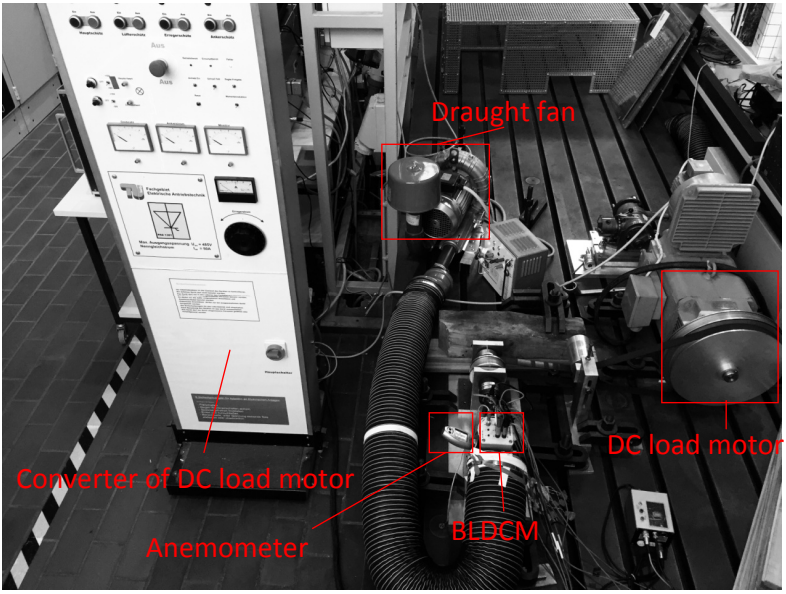

Fig. 4.1: Test bench setup

The test bench consists of the following parts:

• SIEMENS 1 GG5132-0KK10-6JA1-Z load machine

• EA/TU-BERLIN Converter for load machine

• LORENZ DR-2643 torque and speed sensors

– Accuracy class: $\pm(0.1\,\% * 5\,N.m + 0.02\,\% *$ of measured value)

• EFFEPIZETA s.r.l. D09184 - 2007 fan

• ZES Zimmer LMG 670 Power Analyzer :

– Accuracy frequency input: $\pm 50\,ppm$

– Accuracy analog input: $\pm(0.05\,\%$ of reading+$0.05\,\%$ of full scale value)

– Accuracy electric power: $\pm(0.024\,\%$ of measuring range limit + $0.03\,\% *$ of measured value)

• Labview interface platform

The Labview interface platform was developed to realize real-time observation of currents, voltages and speed as well as transmitting and receiving of control instructions. Through CAN bus communication, different operational parameters of the BLDC machines were changed. These include speed setpoint, current setpoint, phase advance angle and PWM duty cycle, depending on the operational state. In addition, with combination of controlling the SIEMENS load machine through a DAQ USB-6356 device and the BLDC machine by CAN bus, serial testing of different load points can be conducted also. The transient data as well as calculated values obtained from power meter LMG670 are used to analyze and evaluate the performance of both BLDC machines.

One stator and two rotors have been built. The proposed IPM rotor with 4 magnet blocks and a conventional one with 8 magnet blocks were shown in Fig. 4.2 and the stator structure was shown in Fig. 4.3.

4.2 Resistance

The resistance of the phase winding is calculated as:

$$R_{20} = \frac{\rho_{20} N L_{\mathrm{av}}}{2ma^2 n_{\mathrm{br}} S} \tag{4.1}$$

where

ρ_{20}: the specific resistivity of the wire's material at 20 °C

N: the total number of wires in all slots

L_{av}: the length of wire for one single coil

m: the number of phases

a: the number of parallel branches

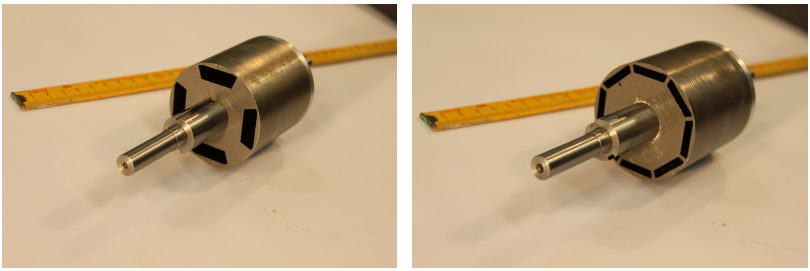

(a) Rotor for BLDCM with 4 magnet blocks (b) Rotor for BLDCM with 8 magnet blocks

Fig. 4.2: Mechanical structure of proposed and conventional rotors

n_{br}: the number of parallel wires per strand

S: the cross sectional area of the wire

The calculated value is 516.22 mΩ. At 19.5 °C, the measured phase resistances of U, V, and W are 473.4 mΩ, 481.9 mΩ and 484.7 mΩ, respectively. The uncertainty of resistor measurement is $\pm 0.7\,m\Omega$ calculated from equation 4.2. These resistance values were also used in preceding FEM simulations.

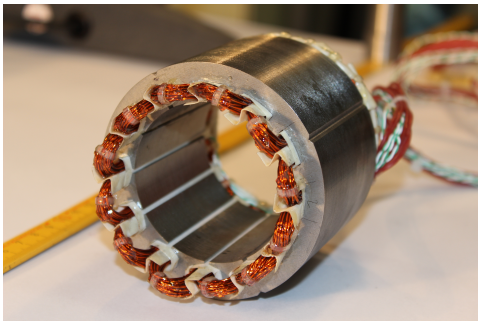

Fig. 4.3: Stator of both BLDCM

4.3 Cogging torque

For cogging torque measurement, the motor shaft is connected with a torque indexing head. In the process of turning the shaft in intervals of 1.875° mechanical angle, the torque value at each position was measured and recorded from the torque sensor.

Fig. 4.4 shows the simulated and measured cogging torque. The IPM machine with 4 magnet blocks has a lower cogging torque than the 8 poles structure. The

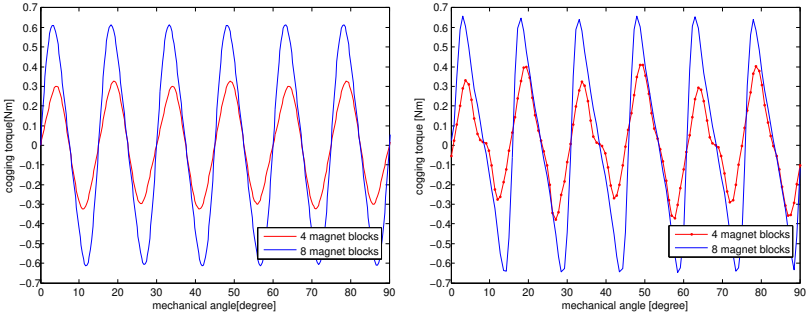

(a) Simulated curves (b) Measured curves

Fig. 4.4: Cogging torque of both BLDCM

average peak value of the cogging torque is 45.4 % lower in the 4-8 than in the 8-8 design. The uncertainty of the measurement is 0.06 Nm.

For the magnet arrangement of 4 magnet blocks, the cogging torque has a 30° mechanical symmetry. However, for the motor with 8 magnet blocks 8 pole pairs has a 15° mechanical symmetry.

4.4 No load test

The simulation of no load and load test is conducted through the combination of 2D motor FEM analysis and external circuit with DC power supply and converter in MAXWELL. The external circuit is shown in Fig. 4.5.

A no load test on a BLDCM gives information about the idle speed and idle losses. By applying an increasing phase voltage to the stator by adjusting the duty cycle without mechanical load ($T_L = 0$), the idle speed and idle loss for both motors at rated 270 V DC were calculated in FEM simulations. Apart from copper loss and core loss, the mechanical loss including bearing loss and windage loss is also calculated in FEM simulation. The comparison of FEM and experimental results are shown in Tab 4.1.

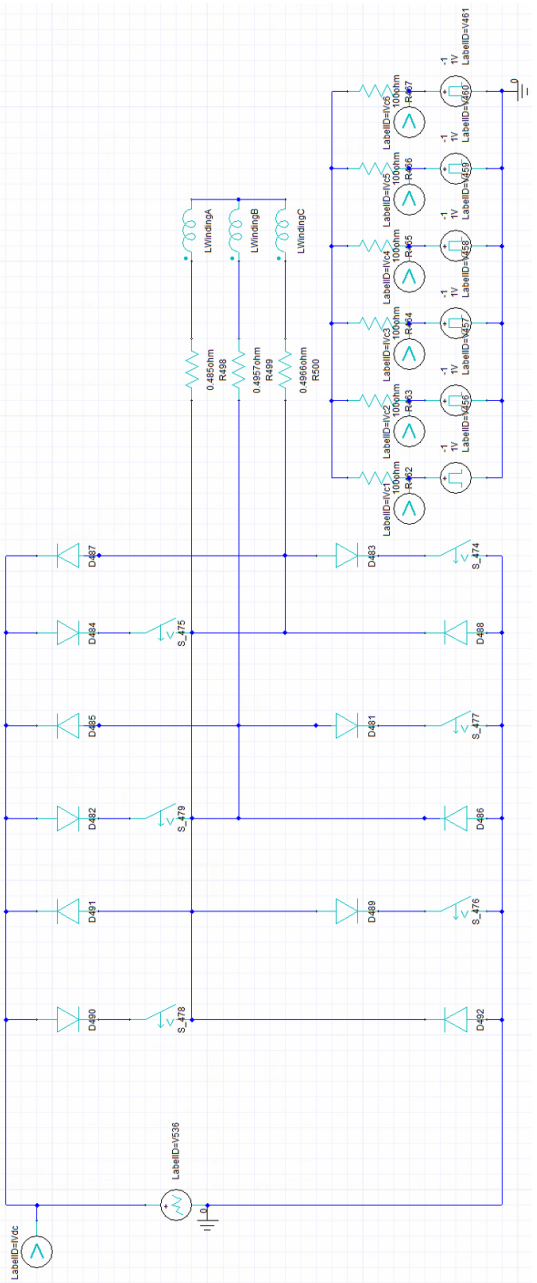

Fig. 4.5: External circuit connected with 2D motor FEA module

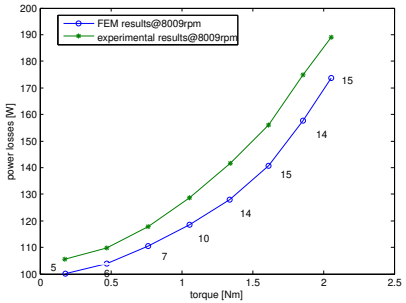

(a) 4-8 magnet blocks

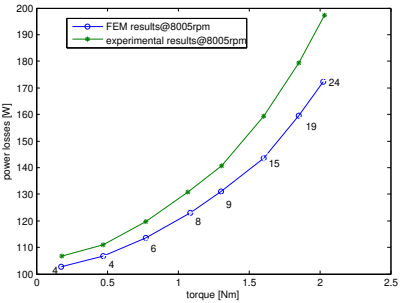

(b) 8-8 magnet blocks

Fig. 4.6: Differences of power losses of the motor in FEM simulated and experimental at rated speed. Numbers in the graphs indicate loss difference(W) from experimental to simulated values.

Tab. 4.1: Simulated and experimental comparison of idle losses of 270 VDC

	rotor structure	idle speed (rpm)	idle losses (W)
Simulation results	4-8 magnet blocks	8851	103.76
	8-8 magnet blocks	8638	104.06
Experimental results	4-8 magnet blocks	8715	107.13
	8-8 magnet blocks	8559	113.52

4.5 Load test

To verify the accuracy of the power losses and efficiency results from FEM simulation, load operation was also conducted on the test bench. To conduct the tests, the load machine is driven at fixed speed and the closed loop controller for the phase current is used for the BLDCM.

The phase advance angle is applied to maximize the motor efficiency at each measured point. It means that the speed is set to constant and adjusting the current by advance angle to reach the maximum efficiency of BLDCM. However the field-weakening control of BLDCM is difficult and has limitations. It can realized through the effect of the Ldi/dt part in the phase voltage equation. The advance angle is corresponding to the reference speed which can be calculated and applied to the commutation strategy.

Fig. 4.6 shows the simulated and experimental results of different load torque points at rated speed of about 8000 rpm. The numbers at the FEM curves show the differences of power loss (W) of the motor from experimental to simulation

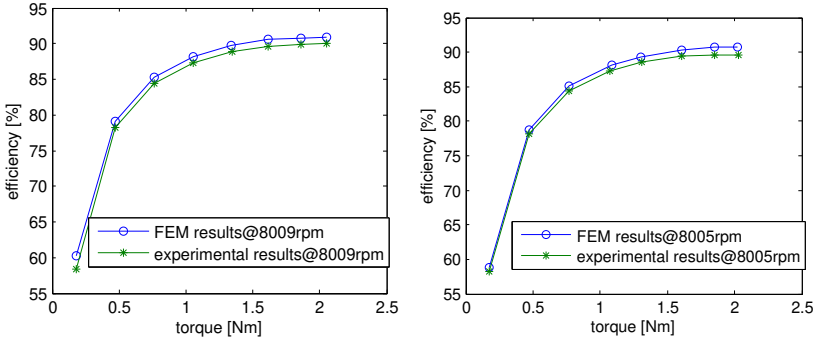

(a) 4-8 magnet blocks

(b) 8-8 magnet blocks

Fig. 4.7: Comparison of FEM simulated and experimental motor efficiency at rated speed

result for each load point. The power loss of the motor from FEA calculation includes core, copper, bearing, and windage losses. The differences increase along with the torque for both motors. Different reasons could account for that difference: material parameters not accurate or extrapolation necessary, parameters for calculation of friction and windage losses inaccurate.

Also the magnet temperature was not part of the simulation, so the magnet temperature is different in simulation and experiment. Comparing both motor efficiencies from the experimental values reveals only a small difference, which is increasing with load up to 0.5 % at 2 Nm in Fig. 4.7.

Further it can be seen, that the motor with 8 magnet blocks generates higher losses than the one with 4 magnet blocks. This can be explained by the higher no-load flux density of the 8-8 design. With higher flux densities the core losses increase, which has a larger effect than the corresponding reduction of copper losses since the core losses dominate the losses according to Fig. 4.9.

From an efficiency perspective, the difference between FEM calculation and experiment is almost constant around 0.8 % for the 4-8 rotor and continuously increasing with load for the 8-8 rotor reaching a maximum difference of 1.2 % at 2 Nm.

By operating BLDCM at different speed levels, the characteristics of torque and current of both motors can be derived. The results are shown in Fig. 4.8. Except the working points at 8000 rpm, all T - I curves have good linearity for both motors. For both BLDC machines the gradient decreases for currents larger than 5 A at 8000 rpm. This is due to operation at the voltage limit with elevated phase advance angles. The T - I curves are compared for for both BLDCM at 1000 rpm and 8000 rpm in Fig. 4.8(c). At low speed it can be seen that the gradient for the 8-8 rotor is steeper due to the higher flux density in the airgap. At 8000 rpm however, the curves become almost equal, which is supposedly due to the necessity for a larger phase advance angle in the 8-8 design.

The experimental recording of power losses for both motors was completed. The copper losses take a rather low percentage of the total power losses when motor

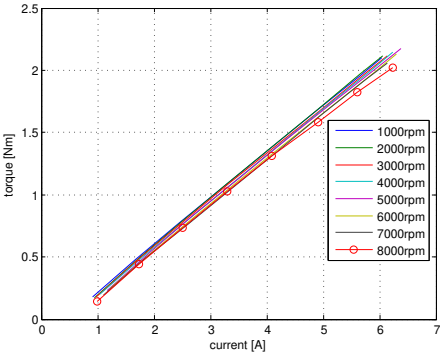

(a) 4-8 magnet blocks

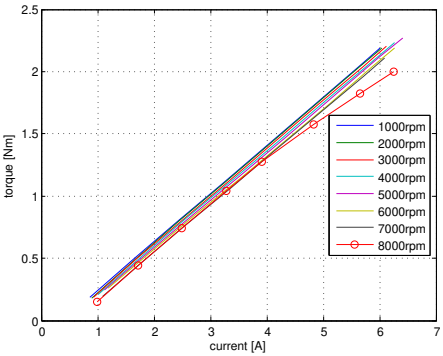

(b) 8-8 magnet blocks

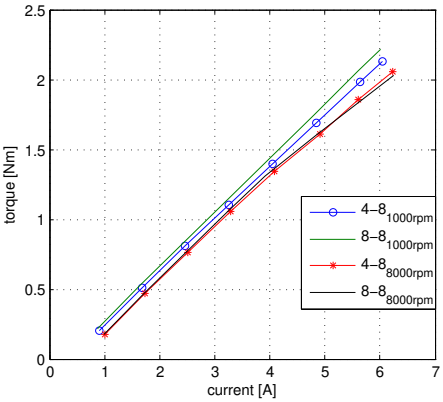

(c) comparison of two motors

Fig. 4.8: Experimental comparison of torque and current characteristics

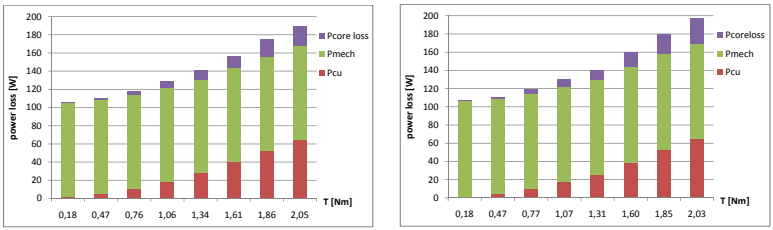

(a) 4-8 magnet blocks (b) 8-8 magnet blocks

Fig. 4.9: Percentage of losses in total power losses

runs at high speed. Fig. 4.9 shows the amount of the calculated copper loss inside the total losses at 8000 rpm. At 2.05 Nm the copper losses make up about 1/3 of the total losses for both machines (4-8: 34 %; 8-8: 33 %).

Fig.4.10 shows that the total power losses have a good linear relationship with the square of the phase current. The BLDCM with 8 magnet blocks produces more power loss at high phase currents, as shown in Fig. 4.10(c). Due to the almost equal ratio of torque to current for both motors (Fig. 4.8(c)), this is equally true for high torque values. At the maximum load point, the BLDCM with 8 magnet blocks generates around 7 W higher losses than the motor with 4 magnet blocks.

A contour plot can be used to examine the efficiency of the machines for all operating points at once. These efficiency maps are shown in Fig. 4.11. As it is shown in Fig. 4.11(c), the BLDCM with 8 magnet blocks has a higher efficiency than the one with 4 magnet blocks for most of the working range, but 8000 rpm there is a slight advantage for the 4-8 design.

Accuracy and Precision of the load test measurement:

For each load point, the measured data was recorded more than 100 times by the Power Analyzer [58]. Fig. 4.12 shows the probability distribution of the efficiency for one measured load point. As it is shown in the graph, the standard deviation of the efficiency is 0.2696 %.

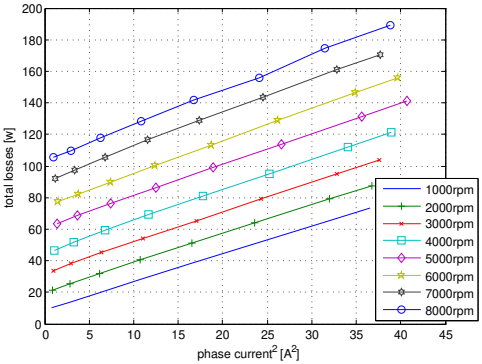

(a) 4-8 magnet blocks

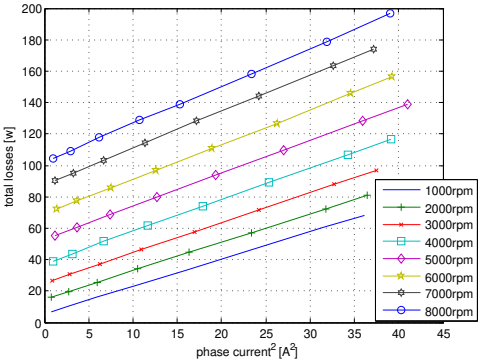

(b) 8-8 magnet blocks

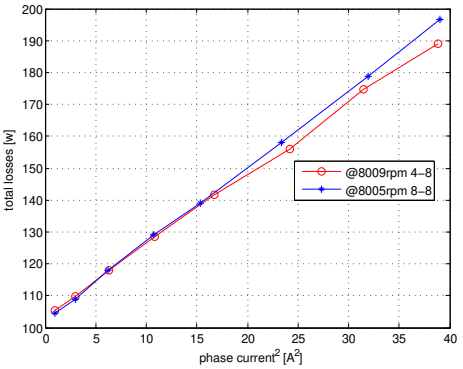

(c) losses comparison at rated speed

Fig. 4.10: Experimental comparison of power losses

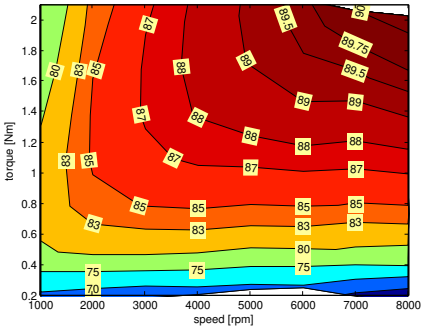

(a) efficiency map of 4-8 rotor

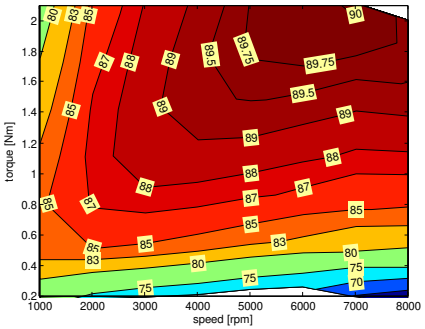

(b) efficiency map of 8-8 rotor

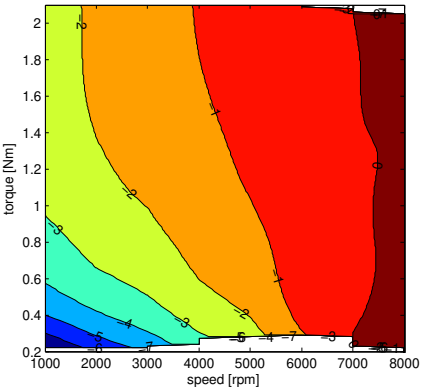

(c) difference of efficiencies; negative numbers indicate a higher efficiency for the 8-8 rotor

Fig. 4.11: Experimental map of motor efficiencies

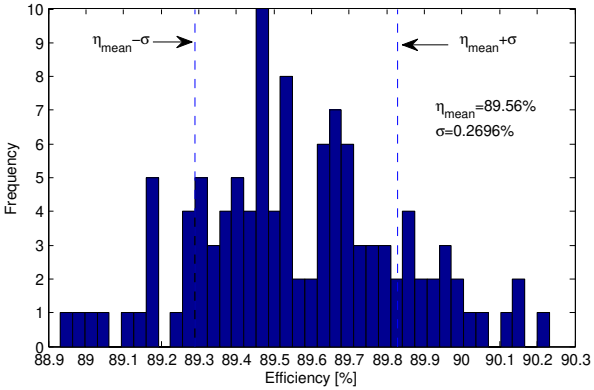

Fig. 4.12: Histogram of one measured point

Based on the uncertainty of the torque sensor and the Power Analyzer, which measures the value of the electric power, torque and speed, the uncertainty calculation of the efficiency will be discussed. Assuming all the variables are uncorrelated, the uncertainty u_c of the calculated value according to f from the measured resources can be expressed as in equation 4.2:

$$u_\mathrm{c} = \sqrt{\sum_{i=1}^{N} \left(\frac{\partial f}{\partial x_\mathrm{i}} u(x_\mathrm{i})\right)^2} \tag{4.2}$$

where $u(x_\mathrm{i})$ are the error limits of the variables and contribute to the total uncertainty.

The uncertainty of the motor efficiency is calculated from the uncertainty of the corresponding measured values. The uncertainties of these are: u_T of the torque sensor itself, u_TZ of the AD-conversion of the torque value , u_nZ of the speed measurement and u_PZ of the electric power measurement. These are expressed in equation 4.3 – 4.6:

$$u_\mathrm{T} = \frac{2\pi}{60}\frac{n}{P_\mathrm{e}}\left(0.1\% \cdot T_\mathrm{f.s.s} + 0.02\% \cdot T_\mathrm{measured}\right) \tag{4.3}$$

$$u_\mathrm{TZ} = \frac{2\pi}{60}\frac{n}{P_\mathrm{e}}\left(0.05\% \cdot T_\mathrm{f.s.z} + 0.05\% \cdot T_\mathrm{measured}\right) \tag{4.4}$$

$$u_\mathrm{nZ} = \frac{2\pi}{60}\frac{T}{P_\mathrm{e}}\left(0.005\% \cdot n\right) \tag{4.5}$$

$$u_\mathrm{PZ} = -\frac{2\pi}{60}\frac{nT}{P_\mathrm{e}^2}\left(0.024\% \cdot I_\mathrm{f.s.z} \cdot U_\mathrm{f.s.z} + 0.03\% \cdot P_\mathrm{e}\right) \tag{4.6}$$

where $T_{\mathrm{f.s.s}}$ is the full scale value of the torque sensor (5 Nm), $T_{\mathrm{f.s.z}}$ is the theoretical full scale value of the torque reading of the Power Analyzer (13 Nm). The power measuring range is derived from the maximum instantaneous values of the current $I_{\mathrm{f.s.z}}$ and voltage $U_{\mathrm{f.s.z}}$. P_{e} is the electric Power.

The standard uncertainty u_{SD} is calculated from equation 4.7.

$$u_{\mathrm{SD}} = \pm\sqrt{u_{\mathrm{T}}^2 + u_{\mathrm{TZ}}^2 + u_{\mathrm{nZ}}^2 + u_{\mathrm{PZ}}^2} \tag{4.7}$$

The hereby calculated absolute value depends on the working point. For the above measurement it is ±0.477%, so the efficiency for that point can be stated as $\eta = (89.6 \pm 0.477)\%$. Torque measurement contributes the most inaccuracy to the measurement of the efficiency.

4.6 Thermal test

In order to get a better understanding of the capacity and limitation of these motors, thermal characteristics of the winding are presented in this part. To emulate cooling at working height, an EFFEPIZETA SCL K05 - MS FAN motor with ventilating pipe is adopted as air cooling system. The pipe is connected to the non- driven end cover of the tested BLDCM. The test bench setup for the thermal test is shown in Fig. 4.1.

In this application, plate fin heat sinks is applied for the forced convection cooling system. The effect of this cooling system is explained as follows [59]. Channel-Reynolds number is expressed as in equation 4.9:

$$Re'_{\mathrm{b}} = Re_{\mathrm{b}}\frac{b}{L_{\mathrm{h}}} \tag{4.8}$$

where Reynolds number $Re_{\mathrm{b}} = Vb/v_1$, b is the width of the fin channel, V is the wind speed, v_1 is the kinematic viscosity, and L_{h} is the length of the fin.

$$Re'_{\mathrm{b}} = Re_{\mathrm{b}}\frac{b}{L_{\mathrm{h}}} \tag{4.9}$$

The dimensionless average heat transfer rated Nu_{b} is expressed in terms of the Nusselt number Nu_{i} defined as:

$$Nu_{\mathrm{b}} = \frac{tanh[\sqrt{2Nu_{\mathrm{i}} \cdot \frac{\lambda_{\mathrm{f}}}{\lambda_1} \cdot \frac{H1}{b} \cdot \frac{H1}{t} \cdot (\frac{t}{L_{\mathrm{h}}} + 1)}]}{\sqrt{2Nu_{\mathrm{i}} \cdot \frac{\lambda_{\mathrm{f}}}{\lambda_1} \cdot \frac{H1}{b} \cdot \frac{H1}{t} \cdot (\frac{t}{L_{\mathrm{h}}} + 1)}} Nu_{\mathrm{i}} \tag{4.10}$$

where:

tanh is Hyperbolic tangent, $H1$ is the high of the fin, t is the width of the fin, λ_1 is the thermal conductivity of the aluminum, λ_{f} is the thermal conductivity of the air.

$$Nu_{\mathrm{i}} = [(\frac{Re'_{\mathrm{b}} \cdot P_{\mathrm{r}}}{2})^{-3} + (0.664\sqrt{Re'_{\mathrm{b}}}P_{\mathrm{r}}^{\frac{1}{3}}\sqrt{1+\frac{3.65}{\sqrt{Re'_{\mathrm{b}}}}})^{-3}]^{-\frac{1}{3}} \tag{4.11}$$

Heat transfer coefficient of h the fin heat sink can be derived:

$$h = Re'_{\mathrm{b}}\lambda_{\mathrm{f}}/b \tag{4.12}$$

Thermal resistance of the housing with fin heat sink is defined by:

$$R_{hs} = \frac{1}{hA} \tag{4.13}$$

where A is the total area of the housing considering the fin heat sink.

Before the thermal test in the laboratory, the winding resistance and the back EMF are measured at a room temperature T_{A} of 19.5 °C. Then the motors operated as close as possible to rated working condition until the change of the temperature in the winding was less than 1 °C per hour. The air speed at the air outlet was 11.9 m/s at ground level by measurement. During the experiments, the motor with 4 magnet blocks run at 8000 rpm and the output mechanical torque was 1.89 Nm. The motor with 8 magnet blocks run at 8008 rpm and mechanical torque was 1.87 Nm. The fan motor was turned on at 13 min 20 s (4-8) and 5 min 5 s (8-8) after the start of the measurement.

Since the change of the temperature of is less than 2 K per hour after running for 2.5 hours, the temperature measurement can be carried out. After stopping motor operation, the measured temperatures decay quickly. International Standard IEC 60034-1 [60] allows to estimate the temperature by the resistance method in machines of less than 50 kW if it is measured within 30 seconds from the disconnection instant [61]. Fig. 4.14(a) and Fig. 4.13(a) show the recorded temperatures time course from different parts of winding for both motors at rated operation. Three temperatures are shown in the graphs:

T_{TC}: the winding temperature inside the slot measured by an inbuilt thermocouple

T_{R}: the winding temperature estimated by measuring the resistance of winding after disconnect

T_{end}: the temperature of the end winding measured by an inbuilt thermocouple

As it is shown in Fig. 4.14(b) and Fig. 4.13(b), the first resistance measurement for calculating the temperature were recorded 20 s after the disconnection and further resistance points are measured in 10 s intervals. The temperature difference from slot and end winding is less than 0.5 °C for both motors at the time of disconnection.

Since the value of temperature at the disconnection instant can be estimated with an exponential decay function, the red line in the figures shows the fitting curve and the extrapolated temperature at the time of disconnection. This average winding temperatures calculated by winding resistance are 83.5 °C and 86.7 °C for the motor with 4 magnet blocks and 8 magnet blocks, respectively. These temperatures are approximately 2 °C lower than the values measured by thermocouple in the end winding.

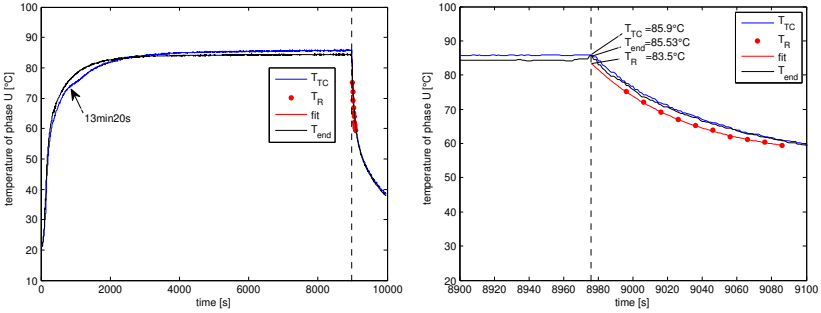

(a) 4-8 structure (b) the extrapolation of the max. temperature

Fig. 4.13: Temperature trend of 4-8 motor with 4 magnet blocks under long time test

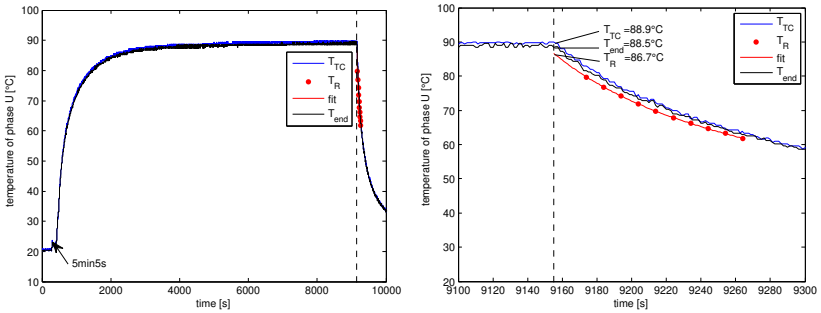

(a) 8-8 structure (b) the extrapolation of the max. temperature

Fig. 4.14: Temperature trend of 8-8 motor with 8 magnet blocks under long time test

Since the power loss of the motor with 8 magnet blocks motor is larger at rated operation, the winding temperature of the motor with 4 magnet blocks is 3 K lower.

Considering the parameters of the air at ground level, the temperature under the housing T_{H}, temperature of the winding T_{W}, and the temperature rise $\Delta T_{\mathrm{f\text{-}H}}$ from the surrounding air of the fin to the surface of the housing are shown in Tab. 4.2.

The test was conducted in the laboratory at an air speed of 11 m/s. The higher temperature of the 8-8 design translates into 64 °C at a working altitude of 20 km, taking into account the adapted properties of the air, ambient temperature and wind speed. At low operating heights the airspeed is assumed to be similar to the conditions in the laboratory. Therefore the maximum temperature occurs at low operating heights, i.e. at start and during climbing. The obtained temperatures are well below the isolation class temperature of the wire (180 °C) and also below

the maximum magnet temperature of 120°C. This gives the possibility to run at overload conditions.

Tab. 4.2: Temperature under different altitude

Flight Altitude	Air Temperature	Air Pressure	Flight Speed	T_A	$\Delta T_{f\text{-}H}$	T_H	T_W
ground level	288.15 K	101325 Pa	11 m/s	292.65 K	48 K	67.5 °C	89 °C
20 km	216.65 K	5529.31 Pa	30 m/s	216.65K	99 K	42.5 °C	64 °C

According to the IEC 60 584, the tolerance of the bedded thermocouple K is ±1.5 °C when the temperature is between 40 and 375 °C. Data Logger Thermometer YC-747UD is used to measure the temperature of thermocouple K bedded in the winding. The accuracy of the YC-747UD is $\pm(0.1\% \, rdg + 0.7°C) = \pm 0.79$ when the temperature is between -100 °C and 1300 °C. The possible deviation is from 0.886 % to 0.889 %.

4.7 Summary

To compare the performance of both BLDCMs, a series of experiments was conducted and presented in this chapter. The BLDCM with 4 magnet blocks has a considerably lower cogging torque than the conventional BLDCM. Through the power loss test, it is verified, that at rated operation, the proposed BLDCM generates less power loss and has a comparable efficiency. Thermal tests were carried out to prove that even with a less powerful cooling system, the magnets are not in danger of running into demagnetization for thermal reasons.

Based on the experimental results of the thermal test, the temperature of the winding is much lower than the designed temperature (180 °C). It is because this design is for the laboratory test and security. And obviously, the motors are oversized.

5 BLDC motor drive system: inverter and control

In this chapter the important design parameter of the inverter driving the BLDCM will be presented, which includes the system structure and performance. Later in this chapter the description of the new analog isolation method for the sensorless control is given.

5.1 Design of voltage source inverter

The basic topology of the inverter is shown in Fig. 2.3. The inverter consists of three phase-legs with transistors paralleling a free-wheeling diode. The principle of driving a BLDC motor is to let the current flow through two phases and keep one of the phases floating. This commutation sequence makes up the six different states available for BLDCM. The applied voltage during each state is commonly modulated by a PWM. First, a prototype of the inverter was built up. This converter includes the following protection and auxiliary functions:

- control sequence of electric relays
- charging and discharging design of DC link capacitor
- overcurrent protection
- overvoltage protection
- overtemperature protection
- sensor control
- sensorless control

The converter was constructed for testing the motor in the laboratory. Therefore it must withstand all motor tests safely. Based on this requirement it was oversized and not optimized for weight or size.

5.1.1 Transistor selection

Based on the rated DC voltage of 270 V, either Metal Oxide Semiconductor Field Effect Transistor (MOSFET) and Insulated−Gate Bipolar Transistors (IGBT) were considered as active devices.

MOSFETs have been developed for high voltage high frequency converter applications due to low loss and high speed switching performance [62]. It has an on-state current carrying capability and off-state blocking voltage capability [63] [64].

Due to high voltage and current ratings, and low conduction loss of IGBT, it has become more attractive in the high voltage and high current applications than the MOSFET [65] [66].

Considering the price, efficiency, application requirement, and selectivity of the available products on the current market, IGBTs are selected as the main power devices for the 270 V propulsion drive system.

In order to protect IGBT chips and reduce the complexity of testing, it is more reliable to chose an integrated IGBT module. Based on this, the Semikron SKiiP module 28AC065V1 was chosen. It offers six 600 V ultrafast Non punch through (NPT) IGBTs for a 3-phase system as well as robust and soft freewheeling diodes in Controlled Axial Lifetime (CAL) technology [67]. NPT IGBTs is based on n-substrate with a lightly doped p layer implanted. It has lower switching losses, higher V_{CEsat}, and robustness. By locally influencing the carrier lifetime along the current path between anode and cathode, the softness and low reverse recovery charge of the CAL diode is achieved, intentionally lowering it at the p-n junction, shown in Fig. 5.1. This non-uniform behavior is reflected in the naming of the diode: Controlled Axial Lifetime or CAL [68]. This module also integrates a Positive Temperature Coefficient (PTC) temperature sensor to monitor the heat sink temperature enabling an over temperature shut down. It is placed near the IGBT chips for easy readout. All components integrated in one package greatly reduce handling and the reduced number of parts increases the reliability.

5.1.2 Switching frequency

The switching frequency is an important control parameter for the motor inverter. For space vector Pulse-Width Modulation (PWM) and discontinuous Pulse-Width Modulation control algorithms [69], in order to decrease electromagnetic interference through introducing specific-order current harmonics, random PWM is introduced [70] [71]. Inverter loss, particularly switching loss, varies directly with switching frequency. Therefore, the switching loss cannot be predicted as the switching frequency is varied randomly, which makes efficiency calculation difficult [72].

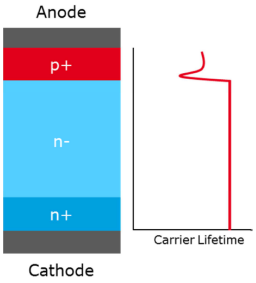

Fig. 5.1: Schematic of CAL diode principle [68](refer to D1, D3, D5 and D2, D4, D6 in Fig. 2.3)

For the six commutation states algorithm, a constant switching frequency f_{PWM} is used. The fixed frequency will reduce the complexity of the control strategy.

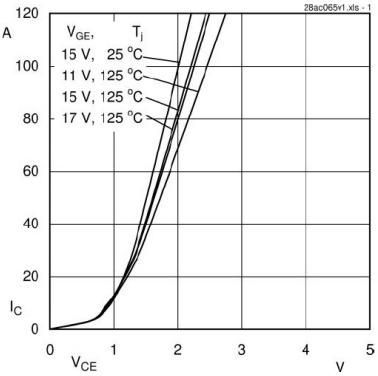

Fig. 5.2: The output characteristic of IGBT [67]

The torque ripple usually comes from three parts: the motor structure, the contol strategy and the PWM of the inverter. The torque ripple caused by motor structure occurs usually at fundamental frequency and its harmonics [73]. Through improving the motor structure inherently, the torque ripple can be reduced to a certain extent which is discussed in the last chapter. It is clear that higher switching frequencies will reduce the torque ripple caused by PWM [74] but lead to an increase of the switching losses.

The other consideration for selecting the switching frequency for this application is to assist in the realization of the sensorless control strategy. To detect the zero-crossing point of the back EMF voltage, the voltage of the floating phase is measured and compared to $U_{\mathrm{DC}}/2$. This voltage has to be measured during the on-state of the PWM period, thus the measurement has to be synchronized to the PWM and typically one value will be obtained during each PWM cycle.

To accurately detect the point at which the value equals 50 % of the DC-link voltage, a high f_{PWM} needs to be selected.

Hence, a switching frequency of 25 kHz which is roughly 47 times of the electric frequency at rated speed should be sufficient. The limitation of sensorless circuit on switching frequency is described in the next part.

5.1.3 Loss analysis

The majority of the power losses is caused by the power semiconductors which are generated inside the semiconductor chips. The loss model used in this thesis takes into account the conduction losses and the switching losses for different working states [75] [76] [77]. The estimated losses are based on the data sheet parameters of the IGBT module which generally are temperature dependent [78]. However, due to the lack of information about switching losses at different temperatures from the data sheet, the worst case condition of the junction temperature (of 125 °C) is assumed for calculating the losses and selecting the cooling system.

5.1.3.1 Conduction Losses

During pulse-width modulation, the power losses can be derived from switching losses, conduction losses, and off-state losses which are negligible and do not need to be calculated [79].

In MOSFETs, the conduction losses P_{cond} occur only due to its on-state resistance. However, different from MOSFETs, IGBTs' conduction losses are calculated using an approximation of a series connection of the on-state constant voltage drop $V_{\mathrm{CE(TO)}}$, which represents the IGBT's collector-emitter voltage during turn-on state at zero current, and the voltage across the turn-on resistance $r_{\mathrm{T,IGBT}}$. For the selected module the on-state voltage drop has a slight positive temperature coefficient, therefore the on-state voltage drop will get larger when the temperature increases. For the inverse diode the same modeling of the losses is possible using $V_{\mathrm{(TO)}}$ and $r_{\mathrm{T,D}}$. For the diodes of the selected module the overall forward voltage drop has a negative temperature coefficient for most of the operating area, i.e. currents below 100 A. The average conduction losses of IGBT and the anti-parallel diode during on-state are given in equation (5.1):

$$\begin{aligned} P_{\mathrm{cond,IGBT}} &= \frac{1}{T_{\mathrm{sw}}} \int_0^{T_{\mathrm{sw}}} p(t)dt \\ &= \frac{1}{T_{\mathrm{sw}}} \int_0^{T_{\mathrm{sw}}} (V_{\mathrm{CE(TO)}} \cdot i_c(t) + r_{\mathrm{T,IGBT}} \cdot {i_c}^2(t))dt \\ &= V_{\mathrm{CE(TO)}} \cdot I_{\mathrm{cav}} + r_{\mathrm{T,IGBT}} \cdot I_{\mathrm{crms}}^2 \end{aligned}$$

and accordingly

$$P_{\mathrm{cond,D}} = V_{\mathrm{(TO)}} \cdot I_{\mathrm{cav}} + r_{\mathrm{T,D}} \cdot I_{\mathrm{crms}}^2 \tag{5.1}$$

where i_c is the current flowing through IGBT, T_{sw} is switching period, I_{cav} and I_{crms} is the average and rms value of the current, respectively. And the parameters of the IGBT are selected based on the data sheet. The output characteristic of IGBT is shown in Fig. 5.2.

5.1.3.2 Switching Losses

The switching loss calculation is depicted in this part. Switching losses of semiconductor switches are linearly dependent on switching frequency. It is more accurate to use the turn-on energy losses $E_{\text{on,IGBT}}$ and switch-off energy losses $E_{\text{off,IGBT}}$ of IGBT to calculate switching losses, as shown in (5.2). It also can be used to calculate switching losses of the diodes based on the reverse recovery energy of diode E_{rr}.

$$\begin{aligned} P_{\text{sw,IGBT}} &= (E_{\text{on,IGBT}} + E_{\text{off,IGBT}}) \cdot f_{\text{sw}} \\ P_{\text{sw,D}} &= E_{\text{rr}} \cdot f_{\text{sw}} \end{aligned} \tag{5.2}$$

where $P_{\text{sw,IGBT}}$ and $P_{\text{sw,D}}$ are the switching losses of the IGBT and diode, respectively.

$E_{\text{on,IGBT}}$ and $E_{\text{off,IGBT}}$ are decided by gate resistor, current and voltage, temperature, as shown in Fig. 5.3. Considering the max. temperature working condition and over load situation, the values are selected based on equation (5.3).

$$E_{\text{on,270V}} = \frac{270V}{300V} \cdot \frac{35A}{100A} \cdot E_{\text{on,300V}} \tag{5.3}$$

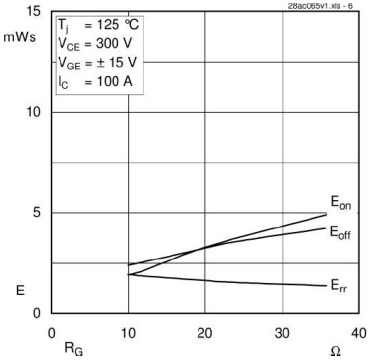

Fig. 5.3: Turn on/off energy of IGBT [67]

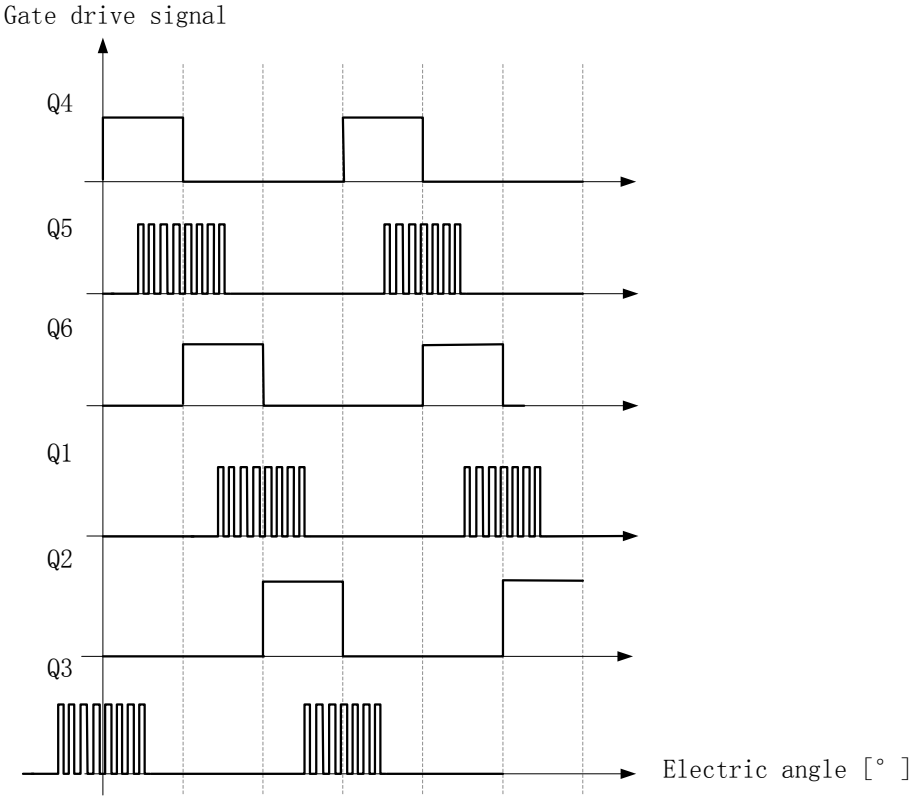

Fig. 5.4: Control strategy of inverter

5.1.3.3 IGBT module Losses

The control strategy of inverter is shown in Fig. 5.4. Q1, Q3,and Q5 are only used for phase transition. PWM control is applied for Q2, Q4,and Q6 for current regulation. Tab. 5.1 represents the power losses of each component during one 120° electric commutation period which includes two 60° electric commutation periods and three commutation moments. As it is shown, IGBT Q1 and diode D2 have the most power losses during 120° electric commutation period which can be calculated from equation (5.4) and (5.5), respectively.

$$P_{\text{loss,Q2}} = P_{\text{con,IGBT}} + P_{\text{sw,IGBT}} + f_1 \cdot E_{\text{turnoff,IGBT}} \tag{5.4}$$

Tab. 5.1: Power losses of components for each commutation state

Component	Commutation moment	60° elec.period	Commutation moment	60° elec.period	Commutation moment
conducting IGBT	Q1, Q6→Q2	Q1, Q2	Q2, Q1→Q3	Q2, Q3	Q2→Q4, Q3
Q2	$E_{\text{on,IGBT}} = 0\vert_{i=0}$	$P_{\text{con,IGBT}}, P_{\text{sw,IGBT}}$			$E_{\text{turnoff,IGBT}}$
D3	$E_{\text{fw,D}}, E_{\text{turn off,D}} = 0\vert_{\frac{\mathrm{d}i}{\mathrm{d}t} \ll \frac{\text{kA}}{\mu\text{s}}}$	—	—	—	—
Q6	$E_{\text{turnoff,IGBT}}$	—	—	—	—
D5	—	$P_{\text{con,D}}, P_{\text{sw,D}}$			$E_{\text{fw,D}}, E_{\text{turnoff,D}} = 0\vert_{\frac{\mathrm{d}i}{\mathrm{d}t} \ll \frac{\text{kA}}{\mu\text{s}}}$
Q1	—	$P_{\text{con,IGBT}}$	$E_{\text{turnoff,IGBT}}$	—	—
D4	—	—	$E_{\text{fw,D}}, E_{\text{turn off,D}} = 0\vert_{\frac{\mathrm{d}i}{\mathrm{d}t} \ll \frac{\text{kA}}{\mu\text{s}}}$	—	—
Q3	—	—	$E_{\text{turnon,IGBT}} = 0\vert_{i=0}$	$P_{\text{con,IGBT}}$	—
Q4	—	—	—	—	$E_{\text{turnon,IGBT}} = 0\vert_{i=0}$

$$P_{\text{loss,D5}} = P_{\text{con,D}} + P_{\text{sw,D}} + f_1 \cdot E_{\text{fw,D}} \tag{5.5}$$

where,

$E_{\text{fw,D}}$ is the free wheeling energy of the diode,

$E_{\text{turnon,IGBT}}$ and $E_{\text{turnon,IGBT}}$ is the energy of turn on and off of IGBT, respectively,

$P_{\text{con,IGBT}}$ and $P_{\text{sw,IGBT}}$ is the conduction losses and switching losses of IGBT, respectively,

$P_{\text{con,D}}$ and $P_{\text{sw,D}}$ is the conduction losses and switching losses of diode, respectively.

Considering the complex of the control strategy of switching the switch IGBT alternately from high voltage side to low voltage side, this control algorithm is not adopted. This converter utilizes only one IGBT at the low voltage half bridge as switching transistor. The total power losses of the integrated IGBT module can be derived from equation (5.6) and is dependent on the duty cycle.

$$\begin{aligned} P_{\text{IGBT\_module}} =& 6 \cdot P_{\text{CM}} + P_{\text{loss,60°}} \\ =& (6 \cdot f_1 (E_{\text{fw,D}} + E_{\text{turnoff,IGBT}}) \\ &+ (\delta P_{\text{con,IGBT}} + P_{\text{sw,IGBT}} + (1-\delta) P_{\text{con,D}} + P_{\text{sw,D}} + P_{\text{con,IGBT}})) \end{aligned} \tag{5.6}$$

Where, δ is the duty cycle.

The total power losses of IGBT module at worst working condition is considered. Assuming that the value of the duty cycle nearly 100 % and the switching frequency 25 kHz, and the maximum peak phase current 30 A were chosen. $E_{\text{fw,D}}$ is negligible. Therefore, the total losses of IGBT module is 156.6 W. The largest power losses of one IGBT is 103.03 W and 53.98 W for diode. Based on the thermal resistance of IGBT and diode, the temperature rise from the junction point to the case of the IGBT $\Delta T_{\text{j-c,IGBT}}$ and to the case of diode $\Delta T_{\text{j-c,D}}$ is 51.55 K and 37.786 K.

5.1.3.4 Gate drive resistor losses

High switching frequency is required and essential for sensorless control in this application. In general, the gate resistance value should be selected based on the range given in the IGBT data sheet. A smaller gate resistor R_{g} will lead to lower switching losses, but results in higher $\mathrm{d}i/\mathrm{d}t$ and $\mathrm{d}v/\mathrm{d}t$ that lead to larger voltage overshoot and EMI emissions. Therefore, it offers less ruggedness and requires thoughtful layout design. [80] suggests that twice of the gate resistance value used inside the IGBT's data sheet is selected as a good starting point for optimization.

Further, the driver must be able to support the peak gate current $I_{\text{g,max}}$ which can be derived from the following equation (5.7).

$$I_{\text{g,max}} = (U_{\text{on}} - U_{\text{off}})/R_{\text{g}} \tag{5.7}$$

where U_{on}, U_{off} is IGBT turn on and turn off gate drive voltage, respectively. I_g is the average current through the gate resistor for each polarity of the current and calculated as given in (5.8):

$$I_g = Q \cdot f_{sw} \tag{5.8}$$

where Q is the electric charge transfer during IGBT turn-on or turn-off. The maximum value of drive current can be obtained from the driver manual [81]. Since a driver can only support a maximum average gate current, this will lead to a limitation of the switching frequency for a given power device.

Considering the above discussion, the gate drive resistance is chosen $R_g = 20\,\Omega$ here which is twice of the minimum gate resistor value from the data sheet. The power losses on R_g are independent on resistance value and can be calculated from equation (5.9).

$$\begin{aligned} P_{g,upper} &= Q(U_{on} - U_{off})(f_{sw} + f_1) \\ P_{g,lower} &= Q(U_{on} - U_{off})f_1 \end{aligned} \tag{5.9}$$

where $P_{g,upper}$ and $P_{g,lower}$ is the power losses of gate resistor with PWM and without PWM, respectively, f_1 is the fundamental frequency. In this system, $P_{g,upper}$ is 0.339 W and $P_{g,lower}$ is 7.1 mW.

5.1.4 Cooling system

In the power electronic system, semiconductor devices are one of the major loss sources and the cooling system contributes to the total volume [82].

Several types of cooling methods and technologies (e.g. natural cooling and forced convection cooling) have been developed in the past [83] [84]. Due to its simple structure, mounting way and low cost, the finned aluminum cooling heat sinks are the most commonly used heat sinks in power electronic converters and also adopted in this application.

The size of the contact area of the power electronics module to the heat sink and the power of the DC fan are two important factors to ensure that the cooling system works under optimum condition.

The proper design is to guarantee the heat generated from IGBT module can be dissipated through the temperature difference between the surface of the IGBT module and aluminum contact of finned heat sink.

$$\Delta T_{heat\_sink} \leq T_{junction\_max} - \Delta T_{IGBT\_module} - T_{Amb} \tag{5.10}$$

where,

ΔT_{heat_sink} is the maximum temperature rise for the heat sink,

$T_{junction\_max}$ is the maximum junction temperature in IGBT,

$\Delta T_{\text{IGBT\_module}}$ is the temperature rise of IGBT module,

T_{Amb} is the ambient temperature.

The temperature rise of IGBT module should be calculated under the worst working condition which produces the maximum power losses, as showed in equation (5.11).

$$\Delta T_{\text{IGBT\_module}} = R_{\text{th(j - s)}} P_{\text{IGBT\_module}} \tag{5.11}$$

Therefore, the thermal resistance of the heat sink can be calculated:

$$R_{\text{th(heat\_sink)}} \leq \Delta T_{\text{heat\_sink}} / P_{\text{IGBT\_module}} \tag{5.12}$$

where the temperatures are in Kelvin.

Based on equation (5.12), the thermal resistance ($0.25\,K/W$) of the finned heat sink $R_{\text{th(heat\_sink)}}$ is chosen for as the results of the combination of the area of heat sink and the fan power [85].

Considering the lab environment, the ambient temperature 40 °C is selected, the temperature rise of the IGBT module is 25.75 K. Based on the temperature rise of IGBT and diode, the maximum junction temperature of IGBT and diode at the worst working situation is 117.3 °C and 103.75 °C which are smaller than the maximum temperature (125 °C) that component can withstand.

Although the converter and cooling system are designed for lab test, the thermal resistance(($0.25\,K/W$)) of heat sink for IGBT module is also calculated working under 20 km altitude. It is based on the calculation method of the thermal resistance of the heat fin in section 4.6. Obviously, the heat emission condition of this converter is not feasible working at 20 km.

5.1.5 Isolation design of PCB

The main electronic Printed Circuit Board (PCB) has to include the following functions: the sampling circuit of the three phase voltages and the DC-link voltage for the sensorless control strategy, a Hall sensor sampling circuit for the sensor based control, a detachable microcontroller board connection, the phase current sensors sampling hardware for the control strategy, the driver for the IGBT module, and over-current/over-temperature protection circuits.

Because of the comparatively high voltage of 270 V for the power circuit, a failure occurring during operation can easily lead to serious consequences, which can even be life−threatening. Therefore the isolation design of this power circuit from the electronic circuit is critical.

According to IEC 60664, the clearance is achieved by keeping a minimum distance 0.5 mm and minimum creepage is 1.6 mm. In Fig. 5.6 the blue plane in the center and the signals inside or on top of this plane (blue for bottom, red for top layer on PCB) belong to the control system. All other signals are from the 270 V power system. Any components connected across this gap incorporate isolation: the isolated DC/DC converter, optical isolators for analog signals

(as described in detail in the following section) and isolated current transducers for phase currents and DC current measurement. The outer blue area near the outside of the PCB provides ground for the primary side of the voltage isolation circuit. These circuits are supplied by a dual output DC/DC converter.

5.2 Sensorless control strategy

The schematic control system is shown in Fig. 5.5. It has not only a Hall sensor circuit, but also a sensorless control strategy to increase the reliability of the control system.

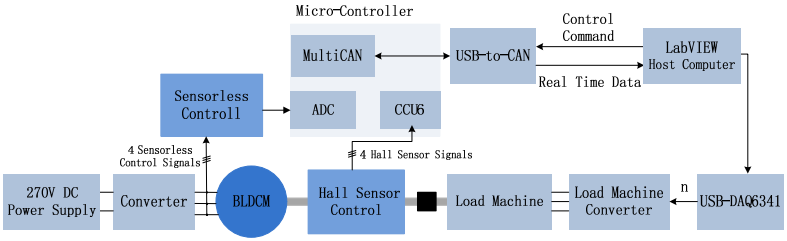

Fig. 5.5: Schematic of control system

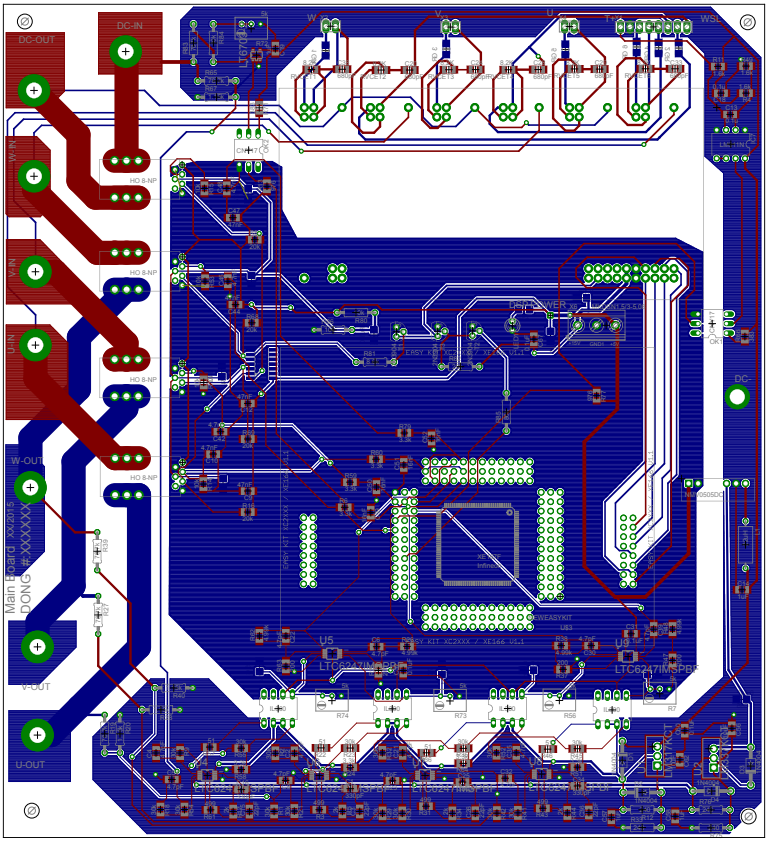

15.01.2019 18:41:09 D:\2_Doctoraldissertation\dissertation\dissertationrong\5inverter\20.04.2015.new.schematic lpf_2.brd

Fig. 5.6: PCB schematic of high and voltages isolation(scaled)

A high speed, good linearity analog isolation circuit was designed to sample the phase voltages of the motor and the DC-link voltage, which are required to realize the sensorless control strategy.

This sensorless control strategy is using the combination of hardware and software methods to detect the rotor position. The circuit has to transmit the isolated terminal voltages $U_{1\text{-}}$, $U_{2\text{-}}$ and $U_{3\text{-}}$ as well as the DC-link voltage U_{DC} to corresponding ADC inputs of the micro-controller. These voltages are re-

lated to the negative rail of the DC-link. When the measured voltage of the floating phase crosses $U_{DC}/2$, this coincides with the zero crossing of the corresponding phase EMF and it can be used to identify the current rotor position. With increasing speed, more accuracy is achieved due to the steeper gradient of the sensed voltage, but less sample points per 60° electric period will limit the maximum achievable accuracy.

The waveform of a phase voltage U_L (from Fig. 2.3)(relative to the negative rail) including PWM is shown in Fig. 5.7. The voltages have to be sampled while the PWM is in its on-period, but a delay after turn-on has to be taken into account, to avoid the turn-on transient behavior. Therefore a minimum turn-on time has to be present.

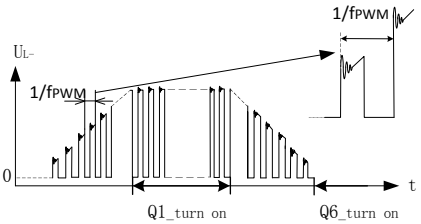

Fig. 5.7: Phase voltage waveform with duty cycle

5.2.1 Concept of the sensorless circuit

The circuit has to fulfill two tasks. The first is to realize the galvanic isolation for the analog voltage signals. The second task is to minimize the response time of the PWM voltages, i.e. a rather high bandwidth is required.

The simple usage of an optocoupler is only sufficient for the first task. Therefore, in this part the design of a fast analog isolation circuit (FAIC) with improved response time will be presented.

The working principle is based on the linear optocoupler IL300. It uses a Light Emitting Diode (LED) that is coupled optically to a servo PhotoDiode (PD) and an output photodiode [86]. The device was designed for both photocurrents to be proportional with low temperature coefficient. Therefore the servo PD is used in a primary side feedback loop to enhance linearity and reduce drifting or aging effects.

The IL300's 130 dB common mode rejection ratio (CMRR), $\pm 50\,ppm/°C$ stability, and $\pm 0.01\,\%$ linearity provide a quality link from the voltage to the controller input including galvanic isolation, hence the IL300 was chosen for the isolation circuit.

Although the photovoltaic topology (PD at zero voltage) of the IL300 offers the best linearity, lowest noise and drift performance, the photoconductive photodiode operation (PD reverse biased) provides a larger frequency bandwidth which is desired in the circuit.

A: Transmission stage

Light emitting diodes have a nonlinear current to light power characteristic. In order to realize a linear analog optical transmission system using light emitting diodes and photodiodes, a feedback control can be applied. If a nonlinear system is operated around a working point in a quite linear section of its characteristic and inserted in a feedback loop control scheme, it can be considered as a linear system [87]. Hence, a feedback loop is applied to connect the LED and servo photodiode.

The servo photodiode (pins 3, 4) on the input side of the IL300 is optically coupled to the LED and produces a current directly proportional to the light flux falling onto its junction. It provides a feedback signal for a control loop which is driving the current to the LED emitter (pins 1, 2). This technique compensates for non-linear, thermal or aging problems of the light emitting diodes.

The solution to meet the bandwidth requirements of the sensorless control system is to add a PI controller in the feedback photodiode loop to control IP1, as shown in Fig. 5.8.

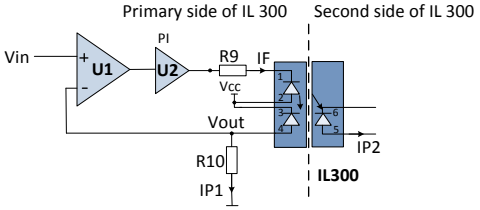

Fig. 5.8: Working principle diagram of the proposed circuit

A value of 25 kHz for the switching frequency was chosen to balance the following two requirements in this application. The sensorless control strategy will be applied only if the duty cycle is higher than 15 % which means the minimal turn on time of one PWM period $t_{\mathrm{on,min}} \geq 6\,\mu\mathrm{s}$. Assuming that the isolation circuit behaves like a first order low pass with a time constant τ, a time constant of $\tau = t_{\mathrm{on,min}}/3$ will settle to less than 5 % error during $t_{\mathrm{on,min}}$.

The working principle is explained according to the block diagram in Fig. 5.9. The voltage to be measured is transmitted through a voltage divider to the first fast operational amplifier U1, which is used as a difference amplifier. A second fast operational amplifier U2 is used as PI controller. The output voltage of U2 is applied to R_9 and becomes the LED current IF. Then the feedback photodiode captures a part of the light flux of the LED and generates a corresponding photocurrent IP1. The indicated time lag behavior is caused by the capacitance of the photodiode in conjunction with the output resistor R10. Finally, IP1 leads to the desired output voltage across resistor R10.

This closed loop control improves both, the linearity and the response time.

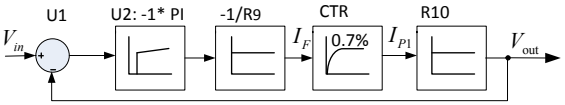

Fig. 5.9: PI Control model of the circuit

B: Reception stage

On the secondary side, the LED flux is also coupled to a photodiode. The output current IP2 of this photodiode is amplified to satisfy the needs of succeeding circuits. The value of the isolated voltage is limited to the supply voltage of U3. The ratio of IP1/IP2 varies from device to device, so for compensation an adjustable amplifier gain was considered.

Based on the control model of the FAIC, the electrical circuit is shown in Fig. 5.10. By adjusting the resistance of R9, the primary LED current IF can be limited. The operational amplifiers U1 and U2 use a $\pm 2.5\,\mathrm{V}$ power supply. In the reception stage, an adjustable resistance R11 is used to eliminate all gain variations throughout the circuit. The additional capacitors C1, C2 and C3 across the input and output of the operational amplifiers are used for compensation to avoid oscillations.

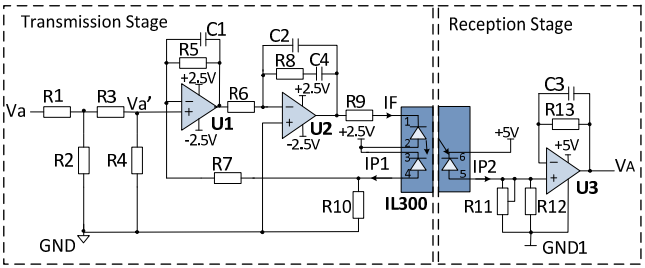

Fig. 5.10: Equivalent circuit diagram of fast analog isolation circuit

C: Transfer gain of circuit

At the transmission stage side, the relationship of LED drive to input voltage is shown by combining equations (5.13), (5.14) and (5.15).

$$V_{1+} = V_{1-} = V_{\mathrm{a}}^{'} \tag{5.13}$$

where V_{1+} and V_{1-} is the voltage of the inverting input and non-inverting input of the amplifier U_1, respectively.

$$I_{\mathrm{P1}} = I_{\mathrm{F}} K_1 \tag{5.14}$$

$$V_{1-} = I_{\mathrm{P1}} \frac{R_{10} R_5}{R_5 + R_7 + R_{10}} \tag{5.15}$$

Equation (5.18) shows that the LED current is related to the input voltage $V_{\mathrm{a}}^{'}$. A changing V_{1+} causes a modulation in the LED flux. The LED flux will change to a level which generates the necessary servo photocurrent to balance the optical feedback loop. The LED flux will be a linear representation of the input voltage, $V_{\mathrm{a}}^{'}$. The servo photodiode's linearity controls the linearity of the isolation IL300.

$$V_{1+} = I_{\mathrm{P1}} \frac{R_{10} R_5}{R_5 + R_7 + R_{10}} \tag{5.16}$$

$$V_{\mathrm{a}}^{'} = I_{\mathrm{F}} K_1 \frac{R_{10} R_5}{R_5 + R_7 + R_{10}} \tag{5.17}$$

$$I_F = \frac{V_{\mathrm{a}}^{'}}{K_1 \frac{R_{10} R_5}{R_5 + R_7 + R_{10}}} \tag{5.18}$$

At the secondary side, the output photodiode is also operated in the photoconductive mode. I_{P2} is derived from the same LED that irradiates the servo photodetector. The output signal, V_{A}, is proportional to the output photocurrent, I_{P2}, times the resistance of parallel connections of R_{11} and R_{12} ($R_{11,12}$).

$$V_{\mathrm{A}} = I_{\mathrm{p2}} R_{11,12} \tag{5.19}$$

$$I_{\mathrm{p2}} = I_{\mathrm{F}} K_2 \tag{5.20}$$

Combining equations (5.19) and (5.20) and solving for I_{F} results in equation (5.21).

$$I_{\mathrm{F}} = \frac{V_{\mathrm{A}}}{K_2 R_{11,12}} \tag{5.21}$$

The voltage divider at the input gives:

$$V_{\mathrm{a}}^{'} = V_{\mathrm{a}} \frac{R_2 R_4}{R_1 R_2 + (R_1 + R_2)(R_3 + R_4)} \tag{5.22}$$

The input-output gain of the isolation circuit is determined by combining equations (5.18), (5.21), and voltage divider equation (5.22), as shown in (5.25).

$$\frac{V_{\mathrm{A}}}{V_{\mathrm{a}}} = \frac{K_2}{K_1} \cdot \frac{R_{11,12}}{\frac{R_{10} R_5}{R_5 + R_7 + R_{10}}} \cdot \frac{R_2 R_4}{R_1 R_2 + (R_1 + R_2)(R_3 + R_4)} \tag{5.23}$$

K_3 is the transfer gain of the IL300. It describes the relation of the input-output photocurrents of the device. The transfer gain is calculated as the output (forward) gain, K_2, divided by servo gain, K_1, as shown in equation (5.24). That leads to the final equation for the transfer gain of the isolation circuit in equation (5.25).

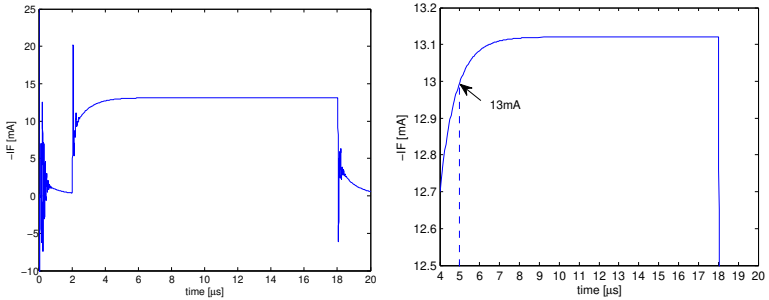

(a) full scale plot (b) detailed plot

Fig. 5.11: Simulated step response curve for primary side current I_F

$$K_3 = K_2/K_1 \tag{5.24}$$

$$\frac{V_A}{V_a} = K_3 \cdot \frac{R_{11,12}}{\frac{R_{10}R_5}{R_5+R_7+R_{10}}} \cdot \frac{R_2R_4}{R_1R_2 + (R_1+R_2)(R_3+R_4)} \tag{5.25}$$

5.2.2 Verification of the sensorless circuit

The model of the circuit was build in LTspiceIV and is used to simulate the performance and response behavior of the isolated circuit. For the amplifier dual LTC6247 (Analog Devices), providing two high speed unity gain stable rail-to-rail input/output operational amplifiers [88], were applied.

The emitting current I_F at rated input voltage is chosen depending on the maximum current allowed through the emitting diode of IL300 and the maximum output sinking current of the LTC6247. However, this current is further limited to less than 20 mA because the best linearity of IL300 will be obtained at drive currents between 5 mA to 20 mA.

Then, in order to ensure the servo photodiode is operated with negative voltage bias, the voltage across R_{10} must be smaller than the power supply voltage of the servo photodiode of +2.5 V.

The IL300 eliminates the problems of gain nonlinearity and drift induced by time and temperature, by monitoring the LED's output flux. A smaller I_F could decrease the effect of above factors. Considering all factors, I_F was chosen to be around 13 mA at rated input voltage.

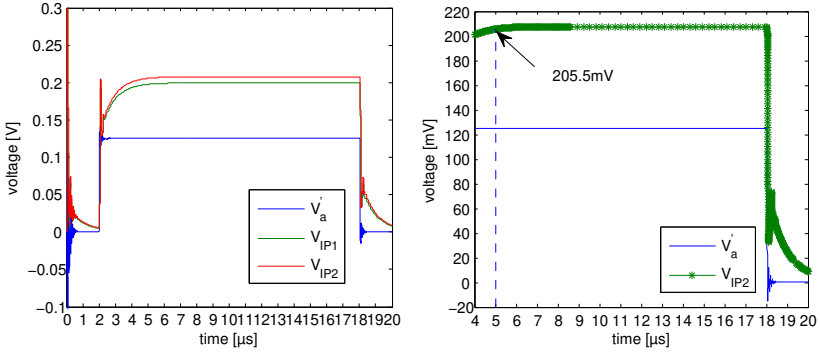

(a) voltage waveform

(b) input and output voltage waveform

Fig. 5.13: Simulated voltage waveform in LTspiceIV

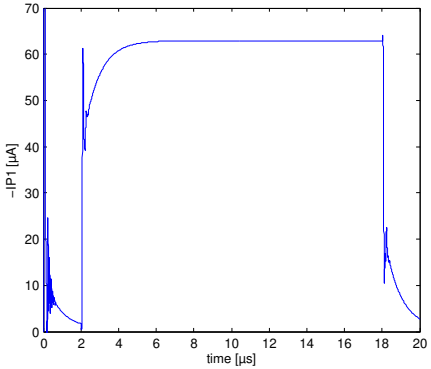

Fig. 5.12: Simulated servo current response waveform

The input voltage in the simulation has a voltage step up to the rated voltage at 2 µs, the corresponding response curve of primary side I_F is shown as in Fig. 5.11. Fig. 5.11(b) shows that the current response value 3 µs later at 5 µs is equal to 13 mA , i.e. within 1 % error of the stable value of 13.12 mA and therefore it meets the design time requirements.

The maximum voltage across R_{10} is 0.231 V, which makes sure, that the servo diode is working in photoconductive mode. At the same time, the photocurrent I_{P1} is roughly -63 µA, as shown in Fig. 5.12.

Fig. 5.13(a) shows the relationship between input voltage and the response behavior of servo feedback and secondary output voltages. In Fig. 5.13(b) the output voltage V_{IP2} at 5 µs is 205.5 mV which is 1 % error compared with the final value of 207.66 mV.

The measured response curves of the input and output signals are shown in Fig. 5.14. The yellow curve represents $V_a^{'}$ after the voltage divider, which is transmitted to the non-inverting input of operational amplifier U1. The green signal V_{IP2} is the output of the operational amplifier U3. The response time is roughly 3 µs and therefore meets the requirement. The output signal has the desired response speed and also meets the requirement of the input signal range of the ADC inside the microcontroller.

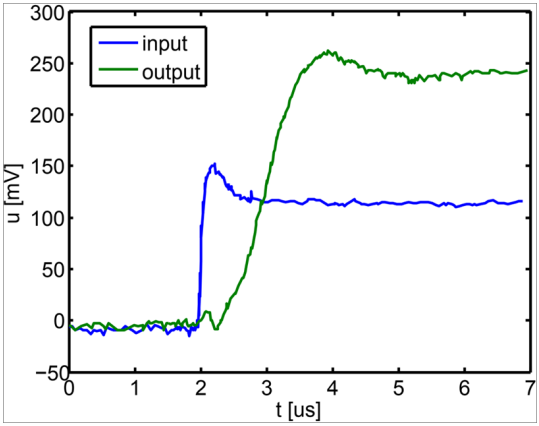

Fig. 5.14: Input and output voltage response waveform

5.2.3 Temperature drift behavior

The temperature drift behavior of the electronic devices affects the accuracy of the control for sensorless strategy. The main components of the sensorless circuit are the amplifier and optocoupler. Based on the information of the temperature drift in the data sheet, the effect is discussed here.

The input offset voltage drift of this amplifier is $-2\,\mu V/°C$. The non-inverting input voltage V_{IP1} of the amplifier U1 is 206 mV shown in Fig. 5.13. When the change of the temperature is 100 K, the temperature drift effect is 0.1 %. The inverting input signal of the amplifier U1 is from the output of the surface mounted voltage resistor divider. The temperature coefficient of the surface mounted resistor is around $\pm 50\,ppm/K$ and has less effect of temperature.

The transfer gain stability K3 of the optocoupler is ±0.5 % at $I_F = 10$ mA when the change of the temperature is 100 K.

Therefore, the effect of temperature on the sensorless circuit can be neglected.

5.3 Summary

A 3 phase full bridge inverter for controlling the BLDCM was designed and built up. It was configured to allow for 200 % of rated load at standstill. It includes the BLDC control strategy of 6 commutation states based on Hall sensor signals, and incorporates over-temperature, over-voltage and over-current protection circuits.

For sensorless control, a fast isolation circuit for phase- and DC-voltages was realized and characterized. By designing the working current of the primary side in the most suitable linear working area of the optocoupler and implementation of the feedback loop for the photodiode light flux, it improves the linearity of the analog signal significantly. A PI controller is applied in the feedback circuit to ensure a response time suitable to follow the PWM modulated voltage sufficiently fast, to allow for the sensorless control method.

6 Analysis of acoustic noise

Vibration and noise of electric machines have been studied extensively [89][90]. Acoustic noise up to 20,000 Hz could be harmful to human hearing [91][92]. The acoustic noise sources of an electrical machine are mainly classified as magnetic, mechanical and aerodynamic sources [93][94][95], as shown in Figure 6.1.

Several researchers applied improved control strategies to avoid exciting and reinforcing the mechanical resonances [96]. [97] proposes high-order sliding mode (HOSM) controllers, combined with the vector control method to improve the dynamic performance of the excitation current and the motor speed.

However, stator vibration due to electromagnetic force is the dominant noise source of the acoustic noise sources [98]. [92] derived an analytical model to study the radial displacement of the stator and verified that noise and vibration is caused by the stator teeth due to the radial electromagnetic force rather than torque ripple and cogging torque. The intensity of acoustic noise is related to the circumferential mode shapes, frequencies, and the magnitude of magnetic radial force [99]. [93] examines the effect of a stator frame on the acoustic noise and vibration.

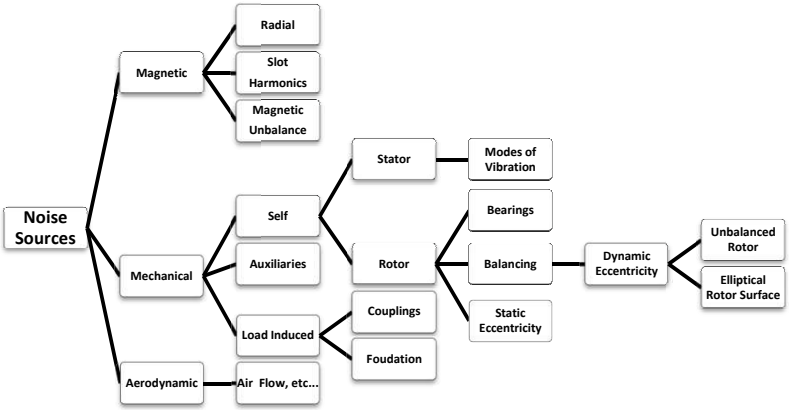

Fig. 6.1: Classification of noise sources [100]

This chapter focuses on the vibration and noise of BLDCM with two different IPM rotor structures, which will be mainly divided into two parts. The first part is dealing with acoustic noise caused by the electromagnetic force. The other important reason of acoustic noise is the amplification by dynamic response

of the motor structure. Therefore, the natural mode analysis is essential for predicting the mechanical noise and was studied in the second part.

6.1 Electromagnetic source

The electromagnetic force produced by magnetic flux exists between magnets and stator teeth, including components in both tangential and radial directions. However, the main source of electromagnetic vibration and noise is the radial force from air gap magnetic field to the stator teeth which is transmitted to the stator surface. This radial force is generated by both, the magnetic field from the rotor and the armature reaction from the load current. The tangential electromagnetic force will provide the torque to drive electric machine.

The electromagnetic radial force generated in the air-gap have an effect on both the stator and rotor. Since the rotor has a regular shape which means more stiffness and less susceptible to the force, the noise is mainly produced by stator. The radial force is distributed on the stator teeth which have less mass and stiffness. Furthermore, the vibrations are also transmitted to the whole yoke and housing structure.

6.1.1 Calculation of the electromagnetic force

The radial electromagnetic force is determined by the magnetic flux density. Different arrangements of the embedded magnets generate distinguishing waveforms along the air gap, as shown in Fig. 3.15. This section will analyze the difference between the electromagnetic forces of the motor with 8 magnet blocks and the motor with 4 magnet blocks.

6.1.1.1 Two calculation methods for the electromagnetic force

There are two common methods to calculate the electromagnetic force [101]. The electromagnetic force is always represented by using the Maxwell stress tensor [102] or force density [103].

A: Stress tensor method

Since the electrical forces can be neglected in electrical machines: E=0, only the magnetic force density $\vec{f_m}$ components is calculated in cylindrical coordinates in equation (6.1) [104].

$$\vec{f_m} = \nabla \cdot T_m - H^2 \cdot \nabla\mu \tag{6.1}$$

The calculation of the electromagnetic force uses Maxwell's Stress Tensor T_m.

$$\vec{F} = \begin{pmatrix} F_x \\ F_y \\ F_z \end{pmatrix} = \iiint_V div(T_m) dV = \int_A T_m d\vec{A} \tag{6.2}$$

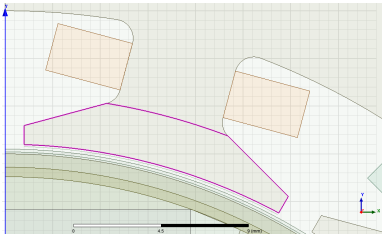

Fig. 6.2: Integration paths of edge force density method on one tooth

where the magnetic tension tensor T_m is the non-dispersive part of $\vec{f_m}$,

$$T_m = \mu \cdot \begin{bmatrix} H_x^2 - \frac{H^2}{2} & H_x \cdot H_y & H_x \cdot H_z \\ H_y \cdot H_x & H_y^2 - \frac{H^2}{2} & H_y \cdot H_z \\ H_z \cdot H_x & H_z \cdot H_y & H_z^2 - \frac{H^2}{2} \end{bmatrix} \tag{6.3}$$

Since 2D stator modal is used to simulate the electromagnetic forces, the force density f_m is only available in Maxwell 2D FEM. It is available only on object outlines adjacent to air vacuum space, as defined as:

$$f_\mathrm{m} = \frac{1}{\mu_0}\mathbf{n} \cdot \begin{bmatrix} B_x^2 - B^2/2 & B_x B_y \\ B_x B_y & B_y^2 - B^2/2 \end{bmatrix} \tag{6.4}$$

where $\mathbf{n}$ is the outward normal direction of the edge.

B: Force density method

Force density $\vec{f}$ is defined as derivation of the electromagnetic force on the stator volume V. The total electromagnetic force $\vec{F}$ can be expressed as in equation (6.5).

$$\vec{F} = \begin{pmatrix} F_\mathrm{x} \\ F_\mathrm{y} \\ F_\mathrm{z} \end{pmatrix} = \iiint_V \vec{f}\, dV \tag{6.5}$$

Based on the x- and y-components of the electromagnetic force density, the electromagnetic forces on the stator can be derived from equations (6.6) and (6.7). These forces will result by integration of the force density over the stator.

The radial electromagnetic force F_rad and the tangential electromagnetic force F_tan on one tooth can be estimated from the magnetic field in the air gap along the purple line, as shown in Fig. 6.2.

$$F_\mathrm{rad} = \oint (f_x \cos\phi + f_y \sin\phi)\mathrm{d}l \tag{6.6}$$

$$F_\mathrm{tan} = \oint (-f_x \sin\phi + f_y \cos\phi)\mathrm{d}l \tag{6.7}$$

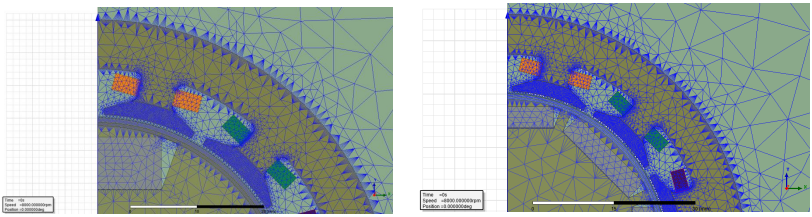

(a) 4 magnet blocks (b) 8 magnet blocks

Fig. 6.3: Meshing results

where ϕ is the polar angle, f_x and f_y represent the x- and y-components of the electromagnetic force density.

6.1.1.2 Comparison of FEM results

Since the edge force density is one of the default results from electromagnetic field calculation in Maxwell and could be used to calculate a set of electromagnetic forces of the motor, the edge force density method is used to calculate electromagnetic force. The forces obtained by this method are imported to ANSYS Mechanical for subsequent analysis on frequency response, vibration, and acoustic noise.

Assuming the magnetic flux does not change along the axial direction and the electromagnetic forces are primarily distributed in radial and tangential direction, a 2D FEM model is sufficient for this study. Due to the symmetry of the traditional and the proposed machine, 1/4 of the motor structure has been built to represent the whole BLDCM.

The quality of the mesh impacts the accuracy of the result. In order to get an FEM force result of higher precision, the air-gap was divided into 3 layers to get a sufficiently fine mesh and therefore more accurate results.

Since the electromagnetic forces act directly on the surface of the stator teeth, a finer mesh with a maximum size of 0.25 mm has been selected at their surface, as shown in Fig. 6.3. The maximum mesh size of stator, coil, rotor and permanent magnet was defined as 5 mm, 1 mm, 5 mm and 2 mm, respectively.

Fig. 6.4 shows the distribution of the radial electromagnetic force on three adjacent stator teeth when the motors run at rated load situation. The maximum electromagnetic force occurs when the axis of the magnet is aligned with a stator tooth.

During the rated load situation, FEM simulated electromagnetic force in radial and tangential direction on a stator tooth for both motors is shown in Fig. 6.5. The magnitude of radial and tangential force differ dramatically and the value of the radial force is much larger than the tangential force. The radial force is the main reason to cause the deformation of the stator, vibration and acoustic noise and the tangential forces mainly cause torque ripple.

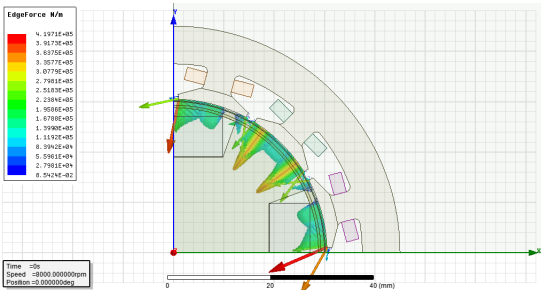

(a) 4 magnet blocks

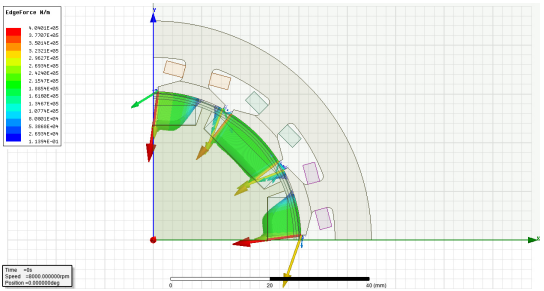

(b) 8 magnet blocks

Fig. 6.4: Electromagnetic force density distribution along the stator teeth

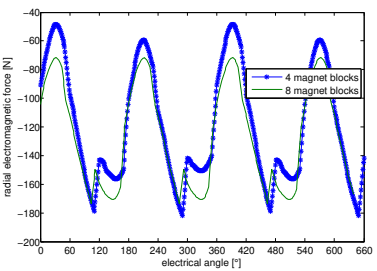

(a) radial force

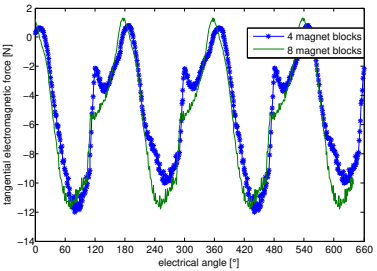

(b) tangential force

Fig. 6.5: Comparison of electromagnetic force on a stator tooth vs. rotor position

The comparison of the radial force on a stator tooth for the two different magnetic structures is shown in Fig. 6.5(a). The radial force of the conventional 8-8 structure has 180° symmetry and equal minimum absolute values of 73.0 N. However, due to the distribution of flux density, the proposed 4-8 rotor structure has two different minimum values, which are 49.1 N and 59.5 N. Both machines have a rather similar maximum radial force, which is 173.7 N for the 8 magnets rotor and 181.6 N for the 4 magnets rotor. It is more important and shows that the poles of electromagnetic force is 1 in the proposed motor and 2 for the conventional rotor structure. The tangential electromagnetic force to produce the output torque is shown as in Fig. 6.5(b) .

In conclusion, the force difference of the radial force is slightly larger in the machine with the 4 magnets rotor. Therefore the vibration in the machine with 4 magnet blocks will be larger.

6.1.2 Vibration analysis of the motor

In the preceding part, it was discussed that the radial electromagnetic force is the main reason to cause the vibration of the electrical machine. Despite the deformation of the stator structure caused by the force will affect the magnetic field, only weak coupling between the electromagnetic forces and mechanical movement can be assumed without loosing precision. Noise emission into the surrounding medium is the result of the vibration. In order to analyze the acoustic behavior of the electrical motor, the vibration caused by force variations on the teeth of the stator is analyzed in this section.

The forced vibration analysis is the essence to evaluate the vibration characteristics of the machine. The acceleration and velocity of the vibration are caused by the excitation through the node force F, as expressed in equation (6.8).

$$[M]\{\ddot{x}(t)\} + [C]\{\dot{x}(t)\} + [K]\{x(t)\} = \{F(t)\} \tag{6.8}$$

where $[M]$, $[C]$, $[K]$ are the mass, damping and stiffness characteristics. $\ddot{x}(t)$, $\dot{x}(t)$, $x(t)$ are the acceleration vector, velocity vector and displacement vector of each node. This equation is the basis for the 3-D FEA mechanical analysis, in which the radial electromagnetic forces act on the stator teeth.

6.1.2.1 FEM procedure

As shown in Fig. 6.6, the first step of the FEM process for motor vibration analysis is to derive the electromagnetic force density from MAXWELL. Afterwards the force density in frequency domain is applied to the teeth of 3D stator stack model. With ANSYS MECHANICAL, the frequency response and deformation of the stator of the electromagnetic force on each tooth can be extracted. The last step is to use the above results and calculate the subsequent acoustic behavior.

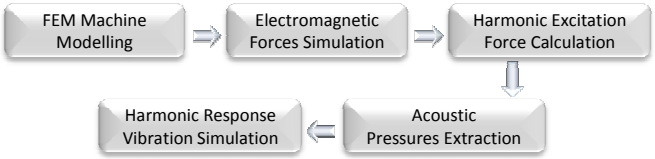

Fig. 6.6: Flow chart for vibration and noise prediction

Owing to the inner interaction and processes in ANSYS Workbench (see Fig. 6.7), the solutions achieved in Maxwell are transformed from time domain to frequency domain by FFT. Afterwards, a harmonic analysis can be conducted which helps to determine the steady state response of a structure to harmonic loads. As a result, harmonic displacements at each Degree Of Freedom (DOF) are generated along with frequency responses. Additionally, sound pressure level result at corresponding frequencies is obtained by applying the acoustic extension. During the simulation, the entire model is assumed to have constant stiffness and mass.

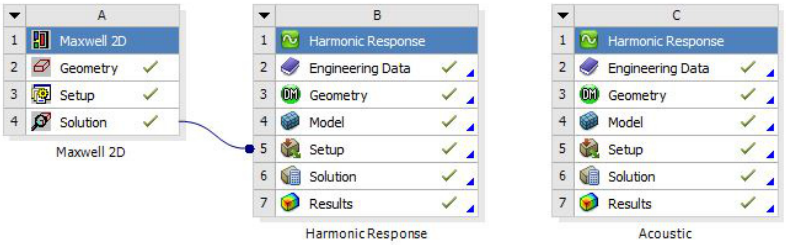

Fig. 6.7: FEM Simulation steps

6.1.2.2 Simulation results

The electromagnetic radial and tangential forces were simulated under the rated load situation of both BLDCMs and the time characteristic of these forces are shown for one tooth in Fig. 6.5. The force density distribution of the inner surface of the stator in time domain is applied as the excitation. Fig. 6.8 and Fig. 6.9 show the harmonic components of the radial and tangential electromagnetic excitation force of one tooth. The radial force dominantly leads to the vibration of the motor. During the rated load working condition, the frequency of the electromagnetic excitation force is mainly located in the range of 0-20 kHz.

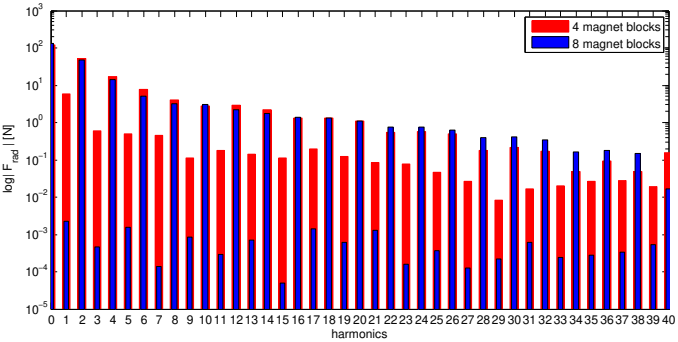

Fig. 6.8: Radial electromagnetic excitation force in the frequency domain on one tooth

Furthermore, it is shown in Fig. 6.8 that the interaction of the rotating rotor and the armature reaction of the stator winding leads to main components located at even order harmonics. Due to the 8-8's 180° periodicity, odd order harmonics are very small for this design. For the 4-8 design, odd order harmonics are present at low amplitudes, that are roughly one order of magnitude smaller than surrounding even order harmonics.

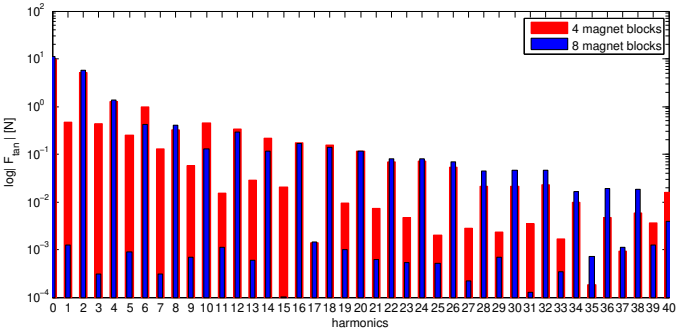

Fig. 6.9: Tangential electromagnetic excitation force in the frequency domain on one tooth

The electromagnetic force simulations are based on a 2D machine model. The calculation result of the electromagnetic force from last Maxwell FEM is coupled to MECHANICAL for harmonic response analysis in the frequency domain and applied to the surfaces of the teeth of the 3D stator model. Fig. 6.10 shows that the direction of electromagnetic forces applied to the stator teeth.

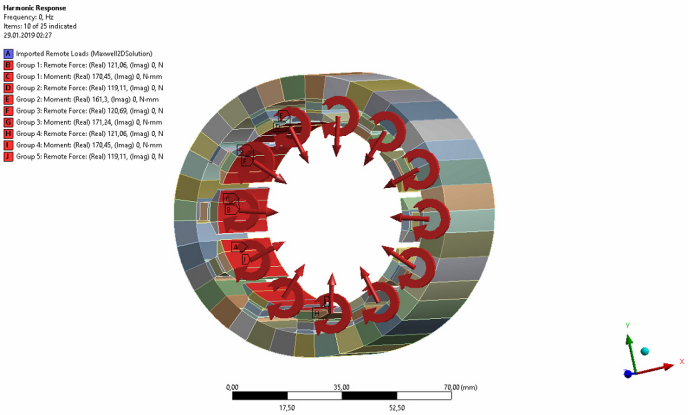

Fig. 6.10: Application of electromagnetic forces to the 3D mechanical stator model

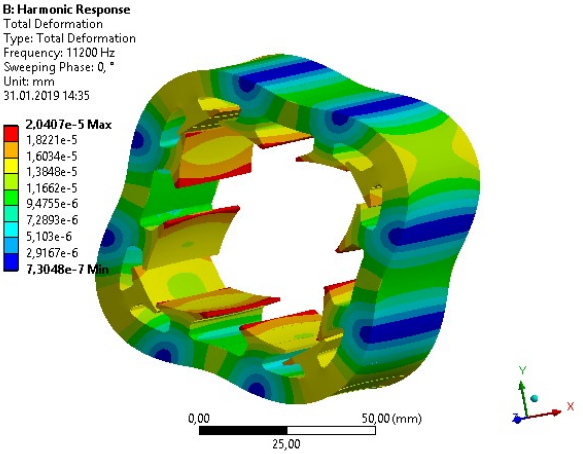

Fig. 6.11: Total deformation of the stator(mm) effected by 4 magnet blocks rotor at 11200 Hz

The frequency response of the harmonic response analysis at the rated working point is shown in Fig. 6.12 and Fig. 6.13 for both motors. The interaction under the excitation of the radial and tangential forces, the maximum acceleration of the stator occurs at a frequency of 11200 Hz for the motor with 4 magnet blocks, which is the 21st harmonic.

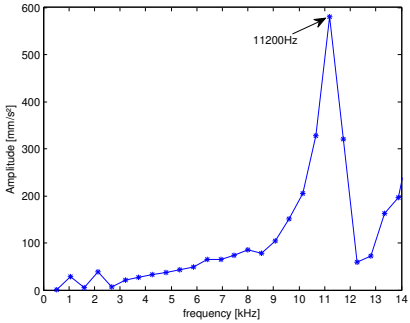

Fig. 6.12: Vibration spectrum on stator with 4 magnet blocks

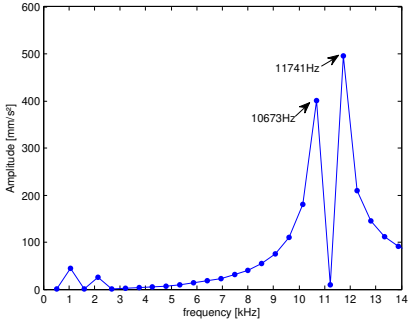

Fig. 6.13: Vibration spectrum on stator with 8 magnet blocks

6.1.2.3 Resonance condition

Since the poles of the electromagnetic forces for the motor with 4 magnet blocks is 4 in 360° mechanical angle, the mode shape of $4k(k = 1, 2, 3 \cdots\cdots\cdots)$ may cause the resonance. By that analogy, the mode shape of $8k(k = 1, 2, 3 \cdots\cdots\cdots)$ for the motor with 8 magnet blocks may cause the resonance.

In order to avoid certain operating speeds at which could cause strong resonance, the corresponding speeds for the harmonic orders at different mode shapes of stator are given in Tab. 6.1.

Tab. 6.1: The relationship of speed and resonance frequency

Mode shape	0	2	3	4	5
Frequency of mode shape f_r(Hz)	16,928	2,366	6,340	11,330	16,534
Harmonic order g	Speed(rpm) $n = f_r/p/g$				
1	253,920	35,490	95,100	169,950	248,010
2	126,960	17,745	47,550	84,975	124,005
3	84,640	11,830	31,700	56,650	82,670
4	63,480	8,873	23,775	42,488	62,003
5	50,784	7,098	19,020	33,990	49,602
6	42,320	5,915	15,850	28,325	41,335
7	36,274	5,070	13,586	24,279	35,430
8	31,740	4,436	11,888	21,244	31,001
9	28,213	3,943	10,567	18,883	27,557
10	25,392	3,549	9,510	16,995	24,801
...					
21				8,093	

As it is shown, during the speed varies from 0–8000 rpm, the motor with 8 magnet blocks does not cause any resonance. However, the motor with 4 magnet blocks cause the weak resonance under the rated working point (8000 rpm) at 21_{th} harmonic order. Fig. 6.11 shows the deformation of the stator with 4 magnet blocks at 11,200 Hz. Apparently mode shape r=4 is excited.

6.1.3 Acoustic noise performance

The vibration of the stator caused by electromagnetic force was simulated in the former section. This vibration transmits energy to the air and generates acoustic noise.

6.1.3.1 FEM analysis

In order to study the acoustic noise, an air model is necessary and has been set up in ANSYS, as shown in Fig. 6.14(a).

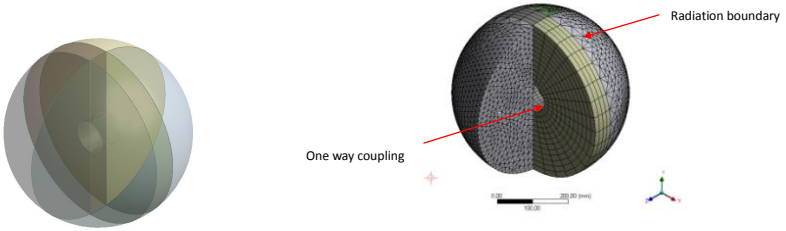

(a) Air model (b) Meshing results

Fig. 6.14: Acoustic performance in the air model

Fig. 6.14(b) shows that the inner contact area of the air model encircles an empty cylinder which has the same outer diameter as the stator model. This entire geometry is defined as 'acoustic body'.

As presented in Fig. 6.8, the electromagnetic radial forces have less impact for frequencies beyond 5 kHz. The element size of the air model should be less than a quarter of the sound wave length. Hence, with the purpose of analyzing the acoustic frequency range below 5 kHz, the mesh size was set to 17 mm. This geometry is divided into six parts to perform sweep method meshing of the extended outside of the stator.

For the rated operation situation, the excitation obtained from FEM harmonic response have been coupled to the interior of the air model for a 'one way coupling analysis'.

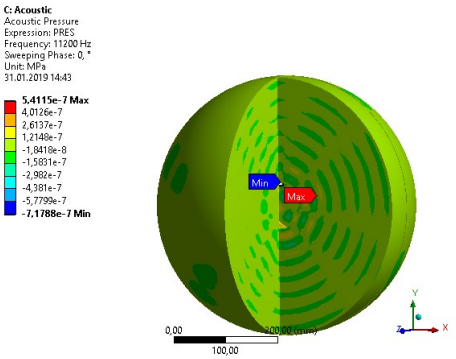

(a) 4 magnet blocks at 11200 Hz

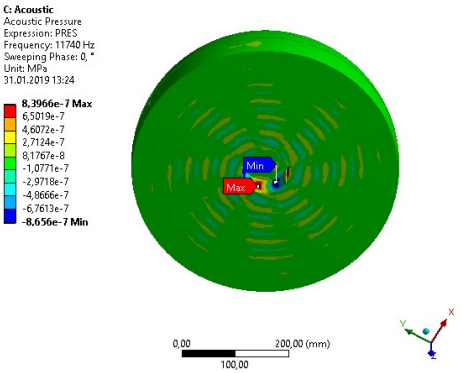

(b) 8 magnet blocks at 11740 Hz

Fig. 6.15: Acoustic performance in the air model

Since the fourth natural mode has been excited at the rated working point, the maximum acoustic pressure of the motor with 4 magnet blocks and 8 magnet blocks occurs at the frequency of 11.2 kHz and 11.7 kHz, respectively. These points were analyzed in FEM, as shown in Fig. 6.15 for both rotor structures. The acoustic pressure for the 8-8 structure is larger than the 4-8 structure, which are $8.3 \cdot 10^{-7}$ MPa and $5.4 \cdot 10^{-7}$ MPa, respectively. There is also another phenomenon, i.e. a vibration occurs also along the axial direction of the machine. Here the SPL decreases from the contact surface of the stator cap to the end edge of the air model. But the noise caused along the axial direction is much smaller than the one based on the radial electromagnetic force.

An 'Acoustic far field microphone' was placed at a 1 m distance from the center of the air model to measure the sound pressure level, as shown in Fig. 6.16. Far field is one of the boundary type in ANSYS which defines an open boundary used to model free-stream compressible flow at infinity.

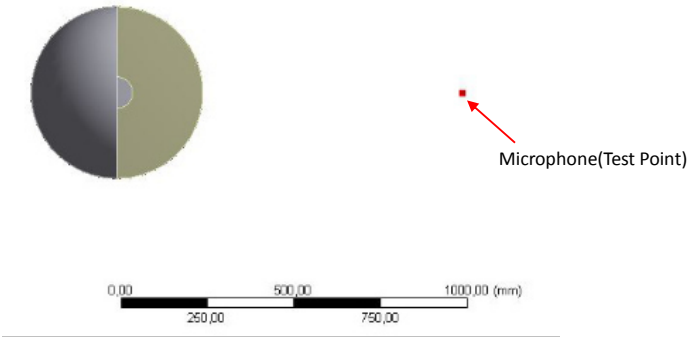

Fig. 6.16: SPL test setup

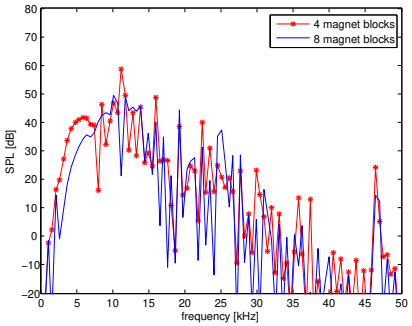

Fig. 6.17: FEM SPL comparison of both magnet structures

Fig. 6.17 shows the simulated sound pressure level at 8000 rpm rated operation for both motors. In general, the proposed machine has a larger noise level. The loudest noise component of 58.6 dB occurs at $f = 11.2$ kHz and is 9.1 dB larger than the highest noise level of the conventional rotor. Because the amplitude of harmonic response analysis for motor with 4 magnet blocks is 96.5 mm/s^2 larger, it may produce higher noise. Moreover, the trend of the 8 magnet blocks structure is smoother before it reaches its peak value.

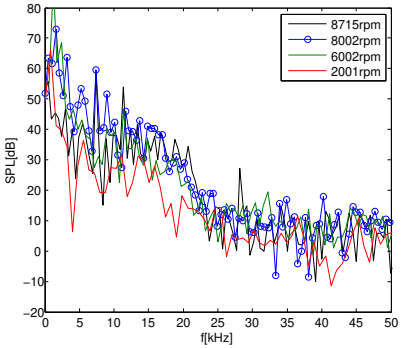

(a) 4 magnet blocks

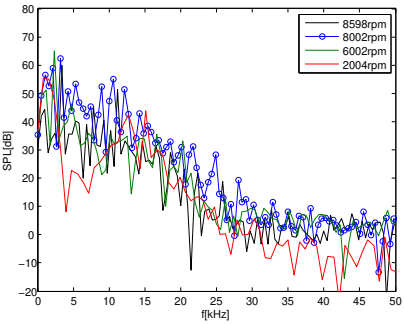

(b) 8 magnet blocks

Fig. 6.18: Experimental acoustic noise test of two motors at different speeds

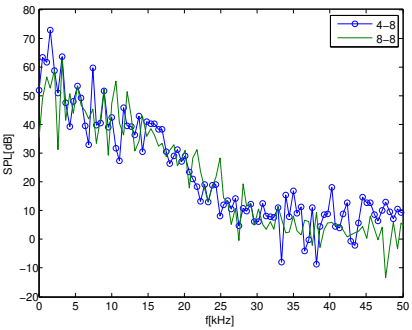

Fig. 6.19: Measured SPL comparison at rated working condition

Under the rated working condition, the SPL of both motors were measured at a distance of 1 m from the motor. The result is shown in Fig. 6.19. At frequencies below 2 kHz the proposed 4-8 design has larger noise.

Fig. 6.18 shows the measured sound spectrum for each motor at different working speeds. It can be seen that the sound of the surroundings in the lab has the rather same sound level. Since the noise level of the motor is relatively low, more accurate acoustic measurements were not conducted. Instead, some further possible sources are investigated in the following paragraph.

6.2 Mechanical source

The mechanical source of noise and vibration is mainly caused by rotor eccentricity and stator vibration. Due to a rotor unbalance, bearing or manufacturing tolerances, eccentricity may occur. This will lead to a rotor displacement from the center of the stator, which causes the air gap magnetic field to generate destabilizing radial forces [105][106]. On the other hand, the electromagnetic force applied to the stator may excite the circumferential mode shapes and natural frequencies of the stator, which cause additional acoustic noise.

6.2.1 Rotor unbalancing

During the manufacturing of the two rotors, one of the shafts became bent during the press fitting process of the rotor lamination to the shaft. In order to reduce the eccentricity, a rotor balancing test became necessary and was conducted.

Limited by the test speed , both rotors were tested at 4700 rpm. Based on this balancing, operation up to about 10,500 rpm is covered. Since the rated speed is about 8000 rpm, the result form the unbalancing measurement is adequate and the hereby calculated mass removals were carried out on the rotor caps.

6.2.2 Modal analysis

The natural frequencies are one of the inherent characteristics of every particular body at which the structure is excitable to vibrate. During the design process of the machine, the natural frequency behavior needs to be considered. When the harmonic frequencies of the electromagnetic force accord with some of the natural frequencies, strong vibrations can be excited and thus noise emitted. Therefore, it is necessary to analyze this characteristic.

6.2.2.1 Analytical calculation of natural frequencies

Since both BLDCM have the same stator, modal analysis is used to calculate the natural frequency of this stator. In [107] an analytical method was used to calculate the natural frequencies based on the natural vibration modes of the stator yoke. The following assumptions are made in predicting the frequencies:

– the yoke part of the stator is a round rigid body
– the stator teeth and winding wound on them have no rigidity, which means the mass is simply attached to the yoke
– the periodic magnetic force waves with r^{th} order are symmetrically extended onto the stator yoke ring
– all defects and notches on the stator have only the effect of mass reduction.

The following equations are used to calculate the natural vibration frequencies f_r for the force wave with r^{th} order:

$$f_r = \frac{1}{2\pi}\sqrt{\frac{k_r}{m}} \tag{6.9}$$

where m is the equivalent mass per square meter (kg/m^2) on the cylindrical surface at the average yoke radius, which can be expressed by the following formula:

$$m = \frac{W_{\text{t}}}{2\pi R_{y,\text{av}} L_{\text{stk}}} \tag{6.10}$$

and k_r is the equivalent spring stiffness coefficient per square meter on the cylindrical surface at the average yoke radius, expressed below:

$$k_r = \begin{cases} \frac{Eh_{\text{y}}}{R_{y,\text{av}}^2} & r = 0 \\ k_{\text{D}} & r = 1 \\ \frac{r^2(r^2-1)}{r^2+1}\frac{Eh_{\text{y}}^3}{12R_{y,\text{av}}^4} & r \geq 2 \end{cases} \tag{6.11}$$

where E is the Young's modulus, h_{y} is the yoke height in the radial direction, $R_{y,\text{av}}$ is the average radius of yoke, k_{D} is the spring stiffness coefficient of the shock absorber under the motor ($k_{\text{D}} = 0$ without absorber), L_{stk} is the effective length of yoke in axial direction, r is mode number and W_{t} is the yoke mass. The numerical parameters for the stator stack are shown in Table 6.2.

Tab. 6.2: Machine parameters

Parameter	Value	Unit
Average radius of yoke $R_{y,\text{av}}$	41.25	mm
Yoke height in radial direction h_y	7.5	mm
Length of yoke in axial direction L_{stk}	59.85	mm
Young's modulus E	$1.85 \cdot 10^{11}$	Pa

The analytical results from the above simplified calculation are shown in Table 6.3.

Tab. 6.3: Analytical results of the resonance frequencies

Mode	Natural frequency (Hz)
0	15,264.9
2	2,149.9
3	6,080.7
4	11,659
5	18,855

6.2.2.2 FEM calculation of natural frequencies

The stator is a more complex object which consists of complex functions of mass and stiffness matrices that are not considered in the analytical model used in the previous section.

With the aid of the structural finite element method, natural frequencies and mode shapes of the stator lamination stack are calculated for a 3D finite element model. In this modal analysis FEM simulation, no load constrain has been added. $[M]$ and $[C]$ in the equation (6.8) are real symmetric matrices of the linear system. Hence, the displacement vector of each node $x(t)$ can be expressed as:

$$\{x(t)\} = \{\phi\}\cos(\omega t) \tag{6.12}$$

where $\{\phi\}$ is the eigenvector and ω is the corresponding frequency. From (6.8) and (6.12), the motion equation for an undamped system can be expressed in the following matrix notation when the free vibration is periodic:

$$([C] - \omega^2[M])\{\varphi\} = 0 \tag{6.13}$$

As hexahedral elements can guarantee free deformation in all degrees of freedom, the sweep meshing method has been used to achieve hexahedral elements which are more accurate compared with a default tetrahedral meshing method. To get a systematic meshing result, the whole stator structure has been divided into substructures, as shown in Fig. 6.20.

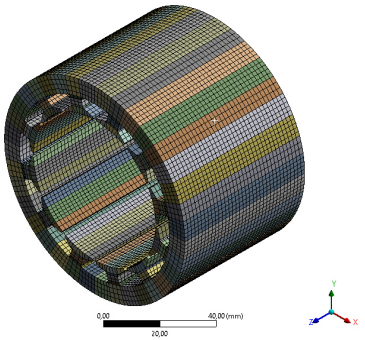

Fig. 6.20: 3D Meshing of stator [100]

In Fig. 6.21 the skewness of mesh metrics after meshing is shown on the x-axis. The skewness represents the evaluation of the meshing quality. A smaller value of the skewness describes better meshing results. The final meshing metric skewness has an average value of 0.139. The mesh metrics are shown below in Fig. 6.21. 'Hex20' and 'Wed15' stand for hexahedral and prismy elements. The hexahedron is the most regular shape and easy to accurately solve. Using hexahedron for meshing, the number of units and nodes is reduced compared to prismatic elements, thus it will save computing time and resources to use hexahedrons dominantly.

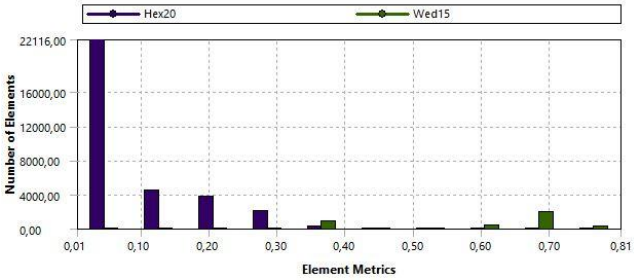

Fig. 6.21: Skewness of mesh metrics [100]

The FEM simulation results for the dominant mode shapes and resonance frequencies are shown in Fig. 6.22.

6.2.3 Resonance frequency measurement

To validate the computed results of the numerical models above, a resonance frequency experiment was carried out. Several researchers used the electrical

acceleration measurement with a certain frequency and sensitivity [108]. Since the magnitude of the excitation does not effect the value of the natural frequency and the procedure of the hammer excitation is much simpler compared to the shaker excitation test, a simple impact hammer testing was conducted. The impact produces an impulse force to excite the structure over a broad frequency range.

6.2.3.1 Test setup

The Measured Object (MO) includes not only the stator stack, but also the coils, housing and an additional aluminum ring placed between housing and stator. A corresponding FEM model, shown in Fig. 6.23(a), was built to simulate the actual structure shown in Fig. 6.23(b). Since the surface bodies that lie on top of each other will have a gap between the midplanes, a setup to employ with bonded contact across a gap between surface body midplanes was used in FEM analysis.

During the test, the structure was hanging upside down on a thread attached to the mounting feet of the housing. The hammer was used to apply a radial direction impulse. The resonance sound was recorded by a microphone placed at the opposite side of excitation side.

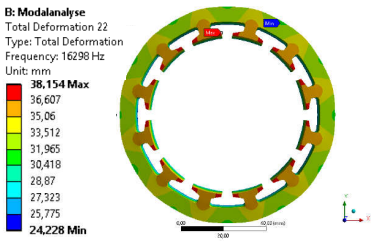

(a) mode=0, f=16,298 Hz

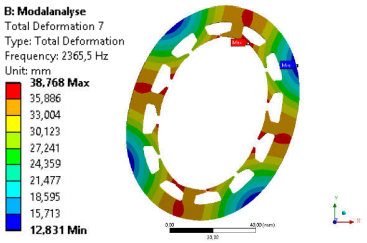

(b) mode=2, f=2,366 Hz

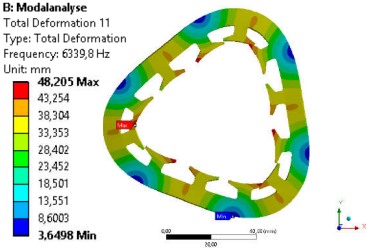

(c) mode=3, f=6,340 Hz

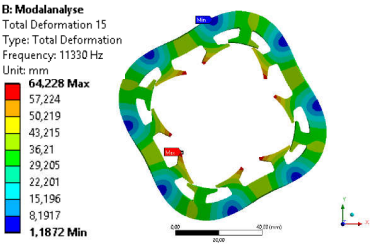

(d) mode=4, f=11,330 Hz

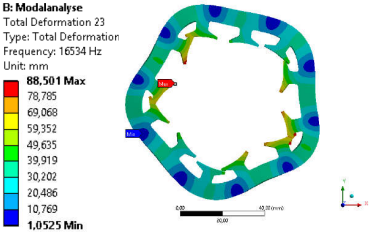

(e) mode=5, f=16,534 Hz

Fig. 6.22: 3D mode shapes and frequencies

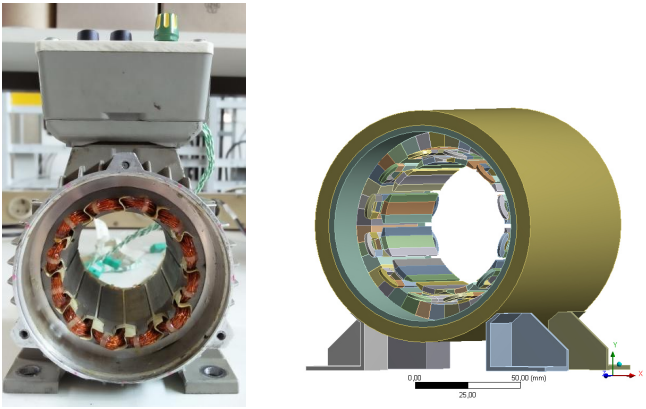

(a) Measured Object (b) 3D FEM model[100]

Fig. 6.23: Test stator parts

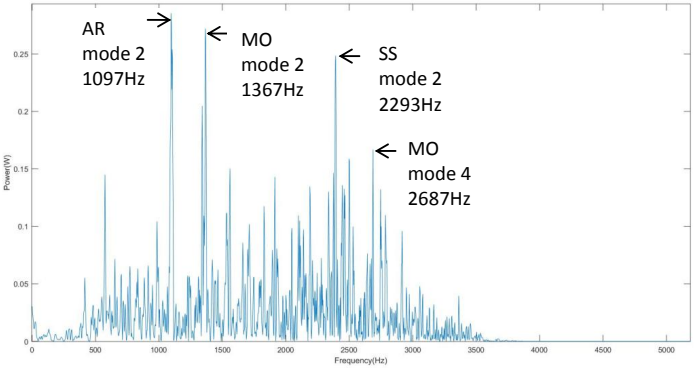

Fig. 6.24: Sound spectrum of impact hammer testing [100]

6.2.3.2 Test results

Several tests have been performed to minimize the errors. The sound signal spectrum after FFT transform is shown in Fig. 6.24. Some mode frequencies can be identified from the spectrum. The 'mode=2' of the Aluminum Ring (AR) and Stator Stack (SS) are clearly showing as peak values. In Table 6.4 the analytic, FEM simulation and test results are compared. As expected, the analytic results show the largest deviation, which are 21.2 % and 10.2 %. The large deviation for

the 3D FEM and test results for the aluminum ring may be due to the damaged stator housing which was repaired using resin glue between stator housing and aluminum ring. The remaining 3D FEM results have relatively small deviation to the test results.

The 2 and 4 mode of the measured object have also been detected in Fig. 6.24. The whole measured object is a complex structure containing different parts, that were modeled in a 3D FEM model. The natural frequency comparison of this structure is also shown in Tab. 6.4.

Tab. 6.4: Natural frequency results comparison

		Natural frequency(Hz)		
Structure Part	Mode	Analytic method	3D FEM	Test
Aluminum Ring (AR)	2	864.7 (21.2 %)	912 (16.9 %)	1097
Stator Stack (SS)	2	2,149.9 (10.2 %)	2,364 (1.2 %)	2,393
Measured Object (MO)	2	N	1,372.2 (0.38 %)	1,367
	4	N	2,843.3 (2.7 %)	2,766.4

Comparing to 3D FEM results, the experimental values of the measured object have 0.38 % and 2.7 % deviation for 2 mode and 4 mode, respectively. The difference may come from the simplification of the model. The coils part were just simplified as solid entity and the end coils were also considered. Further, the connection box and the cooling fins on the housing were disregarded.

6.3 Summary

Acoustic performance of the BLDCM has been discussed in this chapter. 2D FEM models were built to calculate electromagnetic forces of the proposed and conventional BLDCM. Based on a 3D model of the stator, the difference of vibration behavior and noise level of the motors were analyzed. Analytic calculation of natural mode frequencies has also been conducted to compare and validate the accuracy of simulations. In addition, a hammer impact test has been performed to compare the natural mode frequencies of different motor parts with the performed calculations.

7 Summary and future works

7.1 Summary

This dissertation is aimed at designing and developing a high performance BLDC machine and drive technology to improve the performance of electrical propulsion system for solar-powered UAV applications.

A 8 pole BLDC motor with 12 stator slots with only 4 magnet blocks replacing the conventional 8 magnet blocks structure is proposed to fulfill the requirements. Design and construction of prototypes of both proposed and conventional magnet structure have been carried out. A test bench to study the performance of the two motors was built. Hence, an extensive comparison between proposed and conventional magnet structure of BLDC machines has been completed.

The important parameters of the two BLDCMs have been analytically determined and the motor models were verified through the finite element analysis software ANSYS. The results showed good correlation between the simulation and experimental results.

7.1.1 Motor performance

The proposed BLDC machine with 4 magnet blocks for 8 pole pairs has a cogging torque, which is 45.4 % lower than in the conventional design.

The magnet volume only needed to be increased by 11.4 % for the machine using 4 magnet blocks to reach the same RMS value of the back EMF.

Attention was given to the calculation of d-axis inductance L_d and q-axis inductance L_q and influence factors on absolute and differential inductance. The change of the inductance value with rotor position is less sinusoidal for the proposed design and shows two different minimal values. This leads to following conclusions about d- and q-inductance: The L_q values of both motors are almost equal. However, for the 4-8 motor the d-axis inductance has two different values depending on the rotor position relative to the stator teeth. The higher L_d value occurs when the center of each magnet is aligned with a slot, and the lower L_d for alignment with a tooth. Both values are higher compared to the conventional design, for the lower L_d it is +16 % and for the higher L_d +44 %. This leads to an increase in reluctance torque and thus more torque in Maximum Torque Per Ampere operation mode. In practical BLDC operation mode at rated working point, the torque of the motor with 4 magnet blocks is increased by 1.083 %.

For L_q there is only slight saturation visible, at ±8 A the inductance value decreases by 4.7 % for the 8-8 structure and 16.7 % for the 4-8 structure. For the d-inductance the larger L_d value of the 4-8 structure was measured. For both

designs the trend is similar, but the absolute value of the 4-8 design is 21.9 % higher at 0 A. But the relative change is almost identical for both motors.

Considering the uncertainty of 0.5 % of efficiency, the experimental efficiencies of both motors are comparable at rated speed: for the proposed 4-8 design at 89.91 % and 89.56 % for the 8-8 design. At lower speeds the conventional 8-8 design has a higher efficiency: for rated torque the difference is about 1 % at 4000 rpm and 2 % at 2000 rpm. The accuracy of the efficiency measurement is 0.477 %.

A thermal test at rated load was carried out to verify the thermal behavior of the two motors. The motors revealed a steady-state winding temperature of 88.9 °C for the 8-8 design and 85.9 °C for the 4-8 design. The test was conducted in the laboratory at an air speed of 11 m/s. The higher temperature of the 8-8 design translates into 64 °C at a working altitude of 20 km, taking into account the adapted properties of the air, ambient temperature and wind speed. At low operating heights the airspeed is assumed to be similar to the conditions in the laboratory. Therefore the maximum temperature occurs at low operating heights, i.e. at start and during climbing. The obtained temperatures are well below the isolation class temperature of the wire (180 °C) and also below the maximum magnet temperature of 120 °C. This gives the possibility to run at overload conditions.

7.1.2 Acoustic behavior

Acoustic performance of both motors has been studied in a FEM mechanical analysis. A 3D model of the stator was used to analyze the different behavior of the proposed and the conventional rotor structure regarding vibration and noise level. The proposed machine with the 4 magnet blocks rotor produces higher radial electromagnetic forces, leading to a stronger vibration and higher noise levels.

Modal analysis of the stator was conducted through analytical calculation and FEM. The natural frequency of the stator is around 30 times larger than the fundamental frequency, so it can not be excited when the motors run at rated working condition. The 4^{th} mode frequency leads to the maximum resonance and vibration in both motors under the rated working condition.

Modal analysis of the whole part which includes the stator, winding, aluminum ring and housing was analyzed by FEM to verify the hammer impact test. The modal frequencies of each part and the whole structure could be identified in the spectrum of the sound from the hammer impact test.

7.1.3 Sensorless control strategy

For the sensorless control strategy, special attention was given to the isolation of the voltages that need to be measured. A high speed, good linearity analog optical isolation circuit was used to transfer the voltages of the 270 V system to the microcontroller. The proposed circuit uses a PI controller using fast operational amplifiers for the linearizing feedback loop of a linear optocoupler. By this approach, the settling time of the output voltages is reduced to about

3 µs, so the PWM modulated voltage can be accurately measured at low duty cycles of 15 % at 25 kHz switching frequency.

7.2 Future work

Since the d-axis inductance of the proposed and conventional BLDCM have different characteristics, the control behavior affected by inductance could have theoretic and practical significance.

Considering the environment requirement, the lab design of the inverter must be reviewed concerning its application in an aircraft flying in 20 km altitude towards a more lightweight construction has higher challenges.

A Abbreviations

AR	Aluminum Ring
BLDCM	Brushless Direct Current Machine
CAL	Controlled Axial Lifetime
DOF	Degree of Freedom
EMF	ElectroMotive Force
FEA	Finite Element Analysis
IGBT	Insulated−Gate Bipolar
IPM	Interior Permanent Magnet
LED	Light-Emitting Diode
Maximum-Torque-Per-Ampere method	MTPA
MMF	MagnetoMotive Force
MO	Measured Object
MOSFET	Field Effect Transistor
MPPT	Maximum Power Point Tracker
PM	Permanent Magnet
PMSM	Permanent Magnet Synchronous Motor
PTC	Positive Temperature Coefficient
PWM	Pulse Width Modulation
RMS	Root mean square
SPM	Surface-Mounted Permanent Magnet
$SmCo_2$	Samarium-Cobalt
SS	Stator Stack
UAV	Unmanned aerial vehicles

B Symbols

Greek and Other Symbols

α_{i}	pole arc coefficients
ψ_f	flux linkage in the air gap
ψ_R	flux linkage of the rotor
ρ	air density
ρ_{20}	resistivity
δ	air gap
θ_m	Mechanical angle
θ_e	Electric angle
ω	Angular frequency
ψ	Flux linkage
μ_0	Permeability of vacuum
λ	Ratio of motor length and rotor diameter
λ_1	Thermal conductivity of the aluminum
λ_{f}	Thermal conductivity of the air

Latin

a	umber of parallel branches
$\hat{A}'_{\mathrm{s}}$	peek value of current loading
A	The total area of the housing
b	Width of the fin channel
B'_δ	Flux density in the air gap
B_{x}	x-component magnetic density
B_{r}	Remanence
B_{y}	y-component magnetic density
c	Speed of sound
C	Damping
D'_{i}	Rotor diameter
$\vec{E}$	Electric field

E	Young's modulus
$E_{\text{turnon,IGBT}}$	Switch-on energy of IGBT
$E_{\text{turnoff,IGBT}}$	Switch-off energy of IGBT
$E_{\text{fw,D}}$	Free-wheeling energy of diode
E_{rr}	Switch-off energy of diode
f_{d}	Edge force density
f_{sw}	Switching frequency
f_1	Fundamental Frequency
f_{L}	Force density
f_{mf}	Magnetic force density
f_{r}	Frequency of mode shape
$\vec{f}_m$	Magnetic force density
f_{m}	Electromagnetic force density
f_{x}	Electromagnetic force density on x-axis components
f_{y}	Electromagnetic force density on y-axis components
F_{cen}	Centrifugal force
F	Electromagnetic force
F_{rad}	Radial electromagnetic force
F_{tan}	Tangential electromagnetic force
g	Harmonic order
h	Heat transfer coefficient
h_{y}	Yoke height in the radial direction
H	Magnetic field
H_{x}	Magnetic field on x-axis components
H_{y}	Magnetic field on y-axis components
H_{CB}	Coercitivity

$H1$	High of the fin
$\vec{i}$	Phase current
i_c	Current flowing through IGBT
i_{d}	Current in direct axis
i_{q}	Current in quadrature axis
I_{cav}	Average value of current
I_{crms}	RMS value of current
I_{F}	Primary side current of IL300
I_{p1}	Secondary side feedback current of IL300
I_{p2}	Secondary side output current of IL300
I_{g}	Current through gate resistor
I_{u}	Phase U current
I_{v}	Phase V current
I_{w}	Phase W current
$I_{\mathrm{f.s.z}}$	Current range in the Power Analyzer measurement
J_{N}	Electric current density
k_{Nm}	Winding factor
k_D	Spring stiffness coefficient
K	Stiffness
$K1$	Servo gain of IL300
$K2$	Output gain of IL300
$K3$	Inout-output gain of IL300
$k_r(m^3)$	Equivalent spring stiffness coefficient
LM	Magnet thickness
L_{stk}	Motor length
L_{dif}	Differential inductance

L_{d}	Synchronous direct inductance
L_{q}	Synchronous quadrature inductance
L_{h}	Length of the fin
m	Mass
n_{N}	Rated speed
N_{c}	Number of turns per slot
Nu_{i}	Nusselt number
p	Magnet pole pairs
P'	Rated power/efficiency
p_{s}	Sound pressure
p_{ref}	Reference of sound pressure
$P_{\mathrm{cond,IGBT}}$	Conduction losses of IGBT
$P_{\mathrm{cond,D}}$	Conduction losses of diode
$P_{\mathrm{sw,IGBT}}$	Switching losses of IGBT
$P_{\mathrm{sw,D}}$	Switching losses of diode
$P_{\mathrm{loss,D5}}$	Power losses of the diode during 120° electric angle
$P_{\mathrm{loss,Q2}}$	Power losses of the IGBT during 120° electric angle
$P_{\mathrm{IGBT\_module}}$	Power losses of the IGBT module
$P_{\mathrm{g,upper}}$	Power losses of the gate resistor with PWM
$P_{\mathrm{g,lower}}$	Power losses of the gate resistor without PWM
P_{e}	Electric Power
Q	Electric charge energy during IGBT turn-on or turn-off
q	Electric charge
r	Mode number
r	Radius of rotating mass

R_{u}	Phase U resistance
R_{v}	Phase V resistance
R_{w}	Phase W resistance
r_{c}	ON-state resistance of IGBT
R_{g}	Gate resistance
R_{g}	Gate drive resistor
$R_{\mathrm{th(j\text{-}s)}}$	Thermal resistance of the heat sink
$R_1 0$	Feedback resistor of sensorless control circuit
$R_1 1, 12$	Output Parallel resistor of sensorless control circuit
Rs	Stator radius
R	Rotor radius
$R_{\mathrm{y(av)}}$	Average radius of yoke
r_{TO}	on-state resistance of diode
Re'_{b}	Channel-Reynolds number
Re_{b}	Reynolds number
SPL	Sound pressure level
S	Cross sectional area of wire
T_{w}	Teeth width
$TK(B_r)$	Temperature coefficient of remanence
T_{em}	Magnetic torque
T_{sw}	Switching period
$\Delta T_{\mathrm{heat\_sink}}$	Maximum temperature of the heat sink
$T_{\mathrm{junction\_max}}$	Maximum junction temperature in IGBT
$T_{\mathrm{IGBT\_module}}$	Temperature of IGBT module
T_{Amb}	Ambient temperature
$T_{\mathrm{f.s.z}}$	Full scale reading value of Power Analyzer

$T_{\mathrm{f.s.s}}$	Full scale value of torque sensor
T_m	magnetic tension tensor
t	Width of the fin
u_c	Uncertainty of the measurement
$u(x_{\mathrm{i}})$	Error limit
U_{d}	Synchronous direct voltage
U_{T}	Uncertainty of torque sensor
U_{TZ}	Uncertainty of AD-conversion of the torque value
U_{nZ}	Uncertainty of the speed measurement
U_{PZ}	Uncertainty of the electric power measurement
U_{q}	Synchronous quadrature voltage
u_{CE0}	Threshold voltage across IGBT collector-emitter during ON-state
$V_{\mathrm{CE(TO)}}$	on-state constant voltage drop of IGBT
V_{TO}	on-state constant voltage drop of diode
V_{1+}	Voltage of the inverting input of the amplifier
V_{1-}	non-inverting input of the amplifier
Va	Input voltage of sensorless control circuit
Va'	Input voltage of sensorless control circuit after voltage divider
V_{A}	Output voltage of sensorless control circuit
V	Wind velocity
v	Rotating speed
v_1	Kinematic viscosity
W_{mag}	Magnet span
W_{t}	Yoke mass
Z	Number of slots

Bibliography

[1] H. B. Park, J. S. Lee, and K. H. Yu, "Flight evaluation of solar powered unmanned flying vehicle using ground testbed", in *2015 15th International Conference on Control, Automation and Systems (ICCAS)*, pp. 871–874, Busan, South Korea, Oct 2015.

[2] A. Noth, "History of solar flight", *Autonomous Systems Lab, Swiss Federal Institute of Technology Zuerich*, July 2008.

[3] K. Sydorenko and V. Budko, "Flying of the uav by the solar energy", in *2012 2nd International Conference "Methods and Systems of Navigation and Motion Control" (MSNMC)*, pp. 159–160, Kiev, Ukraine, Oct 2012.

[4] Sudha, S. S. R. Patange, S. Raja, B. Aravindu, L. Raghavendra, and M. S. Devi, "Experimental studies for enhancing endurance of unmanned air vehicles", in *2017 International Conference on Electrical, Electronics, Communication, Computer, and Optimization Techniques (ICEECCOT)*, pp. 216–219, Mysuru, India, Dec 2017.

[5] B. M. Albaker, "Preliminary architectonic design for a smart solar-powered uav", in *2013 IEEE Conference on Clean Energy and Technology (CEAT)*, pp. 238–242, Lankgkawi, Malaysia, Nov 2013.

[6] J. Dolce and A. Colozza, "High-altitude, long-endurance airships for coastal surveillance", 03 2005.

[7] J. Meyer, J. A. F. du Plessis, P. Ellis, and W. Clark, "Design considerations for a low altitude long endurance solar powered unmanned aerial vehicle", in *AFRICON 2007*, pp. 1–7, Windhoek, South Africa, Sep. 2007.

[8] R. A. Society, "Airbus zephyr launch". `https://www.youtube.com`. 11 July 2018.

[9] J. Li, *Design Procedure of Propeller for Solar-powered UAV*, 2012.

[10] A. Alsahlani and T. Rahulan, "The impact of altitude, latitude, and endurance duration on the design of a high altitude, solar powered unmanned aerial vehicle", in *2016 International Conference for Students on Applied Engineering (ICSAE)*, pp. 463–468, Alsahlani2016, Oct 2016.

[11] J. Brombach, A. Lücken, B. Nya, M. Johannsen, and D. Schulz, "Comparison of different electrical hvdc-architectures for aircraft application", in *2012 Electrical Systems for Aircraft, Railway and Ship Propulsion*, pp. 1–6, Bologna, Italy, Oct 2012.

[12] X. Zhao, J. M. Guerrero, and X. Wu, "Review of aircraft electric power systems and architectures", in *2014 IEEE International Energy Conference (ENERGYCON)*, pp. 949–953, Cavtat, Croatia, May 2014.

[13] S. J. Forrest, J. Wang, G. W. Jewell, C. M. Johnson, and S. D. Calverley, "Analysis of an ac fed direct converter for a switched reluctance machine in aerospace applications", in *2006 CES/IEEE 5th International Power Electronics and Motion Control Conference*, vol. 2, Shanghai, China, Aug 2006.

[14] W. Xu, "Novel decoupling model-based predictive current control strategy for flux-switching permanent-magnet synchronous machines with low torque ripple and switching loss", *IEEE Transactions on Applied Superconductivity*, vol. 24, pp. 1–5, Oct 2014.

[15] A. Deihimi, "Novel switched reluctance machine synthesis algorithm based on voltage pam control strategy for machine design optimization", in *2009 International Conference on Power Engineering, Energy and Electrical Drives*, pp. 617–622, Lisbon, Portugal, March 2009.

[16] S. M. de Pancorbo, G. Ugalde, J. Poza, and A. Egea, "Comparative study between induction motor and synchronous reluctance motor for electrical railway traction applications", in *2015 5th International Electric Drives Production Conference (EDPC)*, pp. 1–5, Nuremberg, Germany, Sep. 2015.

[17] J. Choi, Y. Chun, P. Han, M. Kim, D. Koo, J. Lee, and J. Chun, "Design of high power permanent magnet motor with segment rectangular copper wire and closed slot opening on electric vehicles", *IEEE Transactions on Magnetics*, vol. 46, pp. 2070–2073, June 2010.

[18] C. Lai, G. Feng, J. Tjong, and N. C. Kar, "Direct calculation of maximum-torque-per-ampere angle for interior pmsm control using measured speed harmonic", *IEEE Transactions on Power Electronics*, vol. 33, pp. 9744–9752, Nov 2018.

[19] Y. Chen, J. Song, J. Zhang, and Q. Huang, "Design and analysis of six-phase fault-tolerant pmsm for electric vehicle", in *2016 Prognostics and System Health Management Conference (PHM-Chengdu)*, pp. 1–6, Chengdu, China, Oct 2016.

[20] H. Yu, Z. Wang, Y. Zhao, H. Xie, and Y. Zhang, "Flux weakening speed control of non-salient pole permanent magnet synchronous motor based on pch and l2 gain", in *2016 Chinese Control and Decision Conference (CCDC)*, pp. 6438–6442, Yinchuan, China, May 2016.

[21] N. Zhao and W. Liu, "Loss calculation and thermal analysis of surface-mounted pm motor and interior pm motor", *IEEE Transactions on Magnetics*, vol. 51, pp. 1–4, Nov 2015.

[22] R. Son and M. Jeon, "A study for starting characteristic analysis method of salient pole synchronous motors", *IEEE Transactions on Industry Applications*, vol. 53, pp. 1627–1634, March 2017.

[23] P. M. Lindh, H. K. Jussila, M. Niemela, A. Parviainen, and J. Pyrhonen, "Comparison of concentrated winding permanent magnet motors with embedded and surface-mounted rotor magnets", *IEEE Transactions on Magnetics*, vol. 45, pp. 2085–2089, May 2009.

[24] A. Seidel, M. Costa, J. Joos, and B. Wicht, "Isolated 100% pwm gate driver with auxiliary energy and bidirectional fm/am signal transmission via single transformer", in *2015 IEEE Applied Power Electronics Conference and Exposition (APEC)*, pp. 2581–2584, Charlotte, NC, USA, March 2015.

[25] L. Cheng, N. Yang, X. Zhou, and M. Yan, "A novel low power consumption and quasilinear cmos optically coupled isolation amplifier", in *2010 International Conference on Computer, Mechatronics, Control and Electronic Engineering*, vol. 5, pp. 175–178, Changchun, China, Aug 2010.

[26] C. E. Lin, A. S. Hou, and K. S. Hsu, "A current conveyor design in wide bandwidth isolation amplifier", in *Proceedings of the 20th IEEE Instrumentation Technology Conference (Cat. No.03CH37412)*, vol. 2, pp. 1013–1017 vol.2, Vail, Colorado, USA, May 2003.

[27] G. Crotti, D. Gallo, D. Giordano, C. Landi, and M. Luiso, "Medium voltage divider coupled with an analog optical transmission system", *IEEE Transactions on Instrumentation and Measurement*, vol. 63, pp. 2349–2357, Oct 2014.

[28] J. B. Simoes, R. M. C. Silva, A. M. L. S. Morgado, and C. M. Correia, "The optical coupling of analog signals", *IEEE Transactions on Nuclear Science*, vol. 43, pp. 1672–1674, June 1996.

[29] B. Mecrow, J. Bennett, A. Jack, D. Atkinson, and A. Freeman, "Very high efficiency drives for solar powered unmanned aircraft", in *2008 18th International Conference on Electrical Machines*, pp. 1–6, Vilamoura, Portugal, Sept 2008.

[30] G. Heins, D. M. Ionel, and M. Thiele, "Winding factors and magnetic fields in permanent-magnet brushless machines with concentrated windings and modular stator cores", *IEEE Transactions on Industry Applications*, vol. 51, pp. 2924–2932, July 2015.

[31] S. Makita, Y. Ito, T. Aoyama, and S. Doki, "The proposal of a new motor which has a high winding factor and a high slot fill factor", in *2014 International Power Electronics Conference (IPEC-Hiroshima 2014 - ECCE ASIA)*, pp. 3823–3827, Hiroshima, Japan, May 2014.

[32] Y. Yokoi, T. Higuchi, and Y. Miyamoto, "General formulation of winding factor for fractional-slot concentrated winding design", *IET Electric Power Applications*, vol. 10, no. 4, pp. 231–239, 2016.

[33] Z. Pan, M. Schweizer, G. Shrestha, and V. Leppänen, "Cell voltage balancing of a series-connected multiphase bldc motor drive", in *IECON 2017 - 43rd Annual Conference of the IEEE Industrial Electronics Society*, Beijing, China, Oct 2017.

[34] J. Dong, Y. Huang, L. Jin, and H. Lin, "Comparative study of surface-mounted and interior permanent-magnet motors for high-speed applications", *IEEE Transactions on Applied Superconductivity*, vol. 26, June 2016.

[35] S.-M. Sue, K.-L. Wu, J.-S. Syu, and K.-C. Lee, "A phase advanced commutation scheme for ipm-bldc motor drives", in *2009 4th IEEE Conference on Industrial Electronics and Applications*, pp. 2010–2013, China, May 2009.

[36] J. Ye, *Design of Brushless DC Machine*. 2007.

[37] M. Centner and U. Schafer, "Optimized design of high-speed induction motors in respect of the electrical steel grade", *IEEE Transactions on Industrial Electronics*, vol. 57, pp. 288–295, Jan 2010.

[38] D. Cichon and R. Psiuk, "Model-based characterization of permanent magnets with a 3d hall-sensor array", in *2016 6th International Electric Drives Production Conference (EDPC)*, Nuremberg, Germany, Nov 2016.

[39] J. Park, H. Kim, S. Lee, and J. Hur, "Characteristics of irreversible demagnetization in accordance with phase advance angle in ipm-type bldc motor", in *2016 IEEE Conference on Electromagnetic Field Computation (CEFC)*, pp. 1–1, Miami, FL, USA, Nov 2016.

[40] J. W. Jung, B. H. Lee, D. J. Kim, J. P. Hong, J. Y. Kim, S. M. Jeon, and D. H. Song, "Mechanical stress reduction of rotor core of interior permanent magnet synchronous motor", *IEEE Transactions on Magnetics*, vol. 48, pp. 911–914, Feb 2012.

[41] J. Rao, R. Qu, J. Ma, and W. Xu, "Investigate the influence of magnetic bridge design on mechanical strength and electromagnetic characteristics in high speed ipm machines", in *2014 17th International Conference on Electrical Machines and Systems (ICEMS)*, Hangzhou, China, Oct 2014.

[42] R. Lin, S. D. Sudhoff, and C. Krousgrill, "Analytical method to compute bridge stresses in v-shape ipms", *IET Electric Power Applications*, vol. 12, no. 7, pp. 938–945, 2018.

[43] A. S. Abdel-Khalik, S. Gadoue, S. Ahmed, and A. Massoud, "A permanent-magnet machine with improved torque density based on a single layer winding layout for electric vehicle applications", in *IECON 2014 - 40th Annual Conference of the IEEE Industrial Electronics Society*, Dallas, TX, USA, Oct 2014.

[44] A. S. Abdel-Khalik, S. Ahmed, and A. M. Massoud, "A nine-phase six-terminal concentrated single-layer winding layout for high-power medium-voltage induction machines", *IEEE Transactions on Industrial Electronics*, vol. 64, pp. 1796–1806, March 2017.

[45] N. Samoylenko, Q. Han, and J. Jatskevich, "Dynamic performance of brushless dc motors with unbalanced hall sensors", *IEEE Transactions on Energy Conversion*, vol. 23, pp. 752–763, Sept 2008.

[46] J. S. Park and K. Lee, "Online advanced angle adjustment method for sinusoidal bldc motors with misaligned hall sensors", *IEEE Transactions on Power Electronics*, vol. 32, pp. 8247–8253, Nov 2017.

[47] X. Song, B. Han, S. Zheng, and J. Fang, "High-precision sensorless drive for high-speed bldc motors based on the virtual 3rd harmonic back-emf", *IEEE Transactions on Power Electronics*, vol. PP, no. 99, pp. 1–1, 2018.

[48] R. M. Pindoriya, A. K. Mishra, B. S. Rajpurohit, and R. Kumar, "Analysis of position and speed control of sensorless bldc motor using zero crossing back-emf technique", in *2016 IEEE 1st International Conference on Power Electronics, Intelligent Control and Energy Systems (ICPEICES)*, Delhi, India, July 2016.

[49] Gajraj, Y. K. Chauhan, and B. Kumar, "Indirect back emf detection based sensorless operation of pmbldc motor drive", in *2016 IEEE 1st International Conference on Power Electronics, Intelligent Control and Energy Systems (ICPEICES)*, pp. 1–5, Delhi, India, July 2016.

[50] *Hall sensor-Continuous-Time Latch Family.*

[51] J. Jung, B. Lee, D. Kim, J. Hong, J. Kim, S. Jeon, and D. Song, "Mechanical stress reduction of rotor core of interior permanent magnet synchronous motor", *IEEE Transactions on Magnetics*, vol. 48, pp. 911–914, Feb 2012.

[52] R. Dutta, M. F. Rahman, and L. Chong, "Winding inductances of an interior permanent magnet (ipm) machine with fractional slot concentrated winding", *IEEE Transactions on Magnetics*, vol. 48, Dec 2012.

[53] P. B. Reddy, A. M. El-Refaie, K. K. Huh, J. K. Tangudu, and T. M. Jahns, "Comparison of interior and surface pm machines equipped with fractional-slot concentrated windings for hybrid traction applications", *IEEE Transactions on Energy Conversion*, vol. 27, pp. 593–602, Sept 2012.

[54] R. Dutta and M. F. Rahman, "A comparative analysis of two test methods of measuring$d$- and$q$-axes inductances of interior permanent-magnet machine", *IEEE Transactions on Magnetics*, vol. 42, Nov 2006.

[55] L. Chong and M. F. Rahman, "Comparison of d- and q-axis inductances in an ipm machine with integral-slot distributed and fractional-slot concentrated windings", in *2008 18th International Conference on Electrical Machines*, pp. 1–5, Vilamoura, Portugal, Sep. 2008.

[56] T. D. Strous, H. Polinder, and J. A. Ferreira, "Inductance calculations for pm machines with concentrated windings", in *2011 IEEE International Electric Machines Drives Conference (IEMDC)*, pp. 447–452, Niagara Falls, ON, Canada, May 2011.

[57] M. Seilmeier, "Modelling of electrically excited synchronous machine (eesm) considering nonlinear material characteristics and multiple saliencies", in *Proceedings of the 2011 14th European Conference on Power Electronics and Applications*, pp. 1–10, Birmingham, UK, Aug 2011.

[58] S. M. Schneider, *Test bench design for power measurement of inverter-operated machines in the medium voltage range*. PhD thesis, Technische Universitaet Berlin, 2018.

[59] P. Teertstra, M. M. Yovanovich, J. R. Culham, and T. Lemczyk, "Analytical forced convection modeling of plate fin heat sinks", in *Fifteenth Annual IEEE Semiconductor Thermal Measurement and Management Symposium (Cat. No.99CH36306)*, pp. 34–41, San Diego, CA, USA, March 1999.

[60] "Rotating electrical machines part 1: Rating and performance", *IEC*, no. 60034-1, 2004.

[61] U. SanAndres, G. Almandoz, J. Poza, and A. J. Escalada, "Thermal test procedure and analytical model calibration method for electrical machines", in *2013 IEEE Workshop on Electrical Machines Design, Control and Diagnosis (WEMDCD)*, pp. 95–103, Paris, France, March 2013.

[62] N. H. Baars, C. G. E. Wijnands, and J. L. Duarte, "Reduction of thermal cycling to increase the lifetime of mosfet motor drives", in *IECON 2014 - 40th Annual Conference of the IEEE Industrial Electronics Society*, Dallas, TX, USA, Oct 2014.

[63] J. Colmenares, D. Peftitsis, G. Tolstoy, D. Sadik, H. P. Nee, and J. Rabkowski, "High-efficiency three-phase inverter with sic mosfet power modules for motor-drive applications", in *2014 IEEE Energy Conversion Congress and Exposition (ECCE)*, Pittsburgh, PA, USA, Sept 2014.

[64] D. Han, C. Morris, W. Lee, and B. Sarlioglu, "Determination of cm choke parameters for sic mosfet motor drive based on simple measurements and frequency domain modeling", in *2016 IEEE Applied Power Electronics Conference and Exposition (APEC)*, Long Beach, CA, USA, March 2016.

[65] S. Woothipatanapan, A. Jangwanitlert, and P. Chancharoensook, "Efficiency improvement of converter for switched reluctance motor drives by mixed parallel operation of igbt and mosfet", in *TENCON 2010 - 2010 IEEE Region 10 Conference*, pp. 1841–1846, Fukuoka, Japan, Nov 2010.

[66] T. Zhao, J. Wang, A. Q. Huang, and A. Agarwal, "Comparisons of sic mosfet and si igbt based motor drive systems", in *2007 IEEE Industry Applications Annual Meeting*, pp. 331–335, New Orleans, LA, USA, Sept 2007.

[67] Semikron, *SKiiP 28AC065V1*, 2006.

[68] M. Hansmann, *Technical Explanation CAL Diodes*, 2014.

[69] S. Das, G. Narayanan, and M. Pandey, "Space-vector-based hybrid pulsewidth modulation techniques for a three-level inverter", *IEEE Transactions on Power Electronics*, vol. 29, pp. 4580–4591, Sept 2014.

[70] F. Yang, A. R. Taylor, H. Bai, B. Cheng, and A. A. Khan, "Using d q transformation to vary the switching frequency for interior permanent magnet synchronous motor drive systems", *IEEE Transactions on Transportation Electrification*, vol. 1, pp. 277–286, Oct 2015.

[71] A. M. Trzynadlowski, R. L. Kirlin, and S. F. Legowski, "Space vector pwm technique with minimum switching losses and a variable pulse rate [for vsi]", *IEEE Transactions on Industrial Electronics*, vol. 44, pp. 173–181, Apr 1997.

[72] Y. L. Familiant and A. Ruderman, "Variable switching frequency pwm technique for induction motor drive to spread acoustic noise spectrum with reduced current ripple", *IEEE Transactions on Industry Applications*, vol. 52, pp. 5355–5355, Nov 2016.

[73] M. S. Islam, R. Islam, and T. Sebastian, "Experimental verification of design techniques of permanent-magnet synchronous motors for low-torque-ripple applications", *IEEE Transactions on Industry Applications*, vol. 47, pp. 88–95, Jan 2011.

[74] D. Jiang, Q. Li, X. Han, and R. Qu, "Variable switching frequency pwm for torque ripple control of ac motors", in *2016 19th International Conference on Electrical Machines and Systems (ICEMS)*, pp. 1–5, Chiba, Japan, Nov 2016.

[75] F. Blaabjerg, U. Jaeger, and S. Munk-Nielsen, "Power losses in pwm-vsi inverter using npt or pt igbt devices", *IEEE Transactions on Power Electronics*, vol. 10, pp. 358–367, May 1995.

[76] M. Ke, "Power electronics for the next generation wind turbine system", 2015.

[77] M. Ishiko and T. Kondo, "A simple approach for dynamic junction temperature estimation of igbts on pwm operating conditions", in *2007 IEEE Power Electronics Specialists Conference*, pp. 916–920, Orlando, FL, USA, June 2007.

[78] D. D. Graovac and M. Puerschel, *IGBT Power Losses Calculation Using the Data-Sheet Parameters*, 2009.

[79] O. Semiconductor, *Thermal Calculations for IGBTs*, 2014.

[80] M. Hermwille, *Gate Resistor – Principles and Applications*, 2007.

[81] SEMIKRON, *Sixpack IGBT and MOSFET Driver SKHI61R and SKHI71R*, 2007.

[82] D. Christen, M. Stojadinovic, and J. Biela, "Energy efficient heat sink design: Natural vs. forced convection cooling", in *2016 IEEE 17th Workshop on Control and Modeling for Power Electronics (COMPEL)*, pp. 1–8, Trondheim, Norway, June 2016.

[83] S. Y. Kim and R. L. Webb, "Analysis of convective thermal resistance in ducted fan-heat sinks", *IEEE Transactions on Components and Packaging Technologies*, vol. 29, pp. 439–448, Sept 2006.

[84] C. Gammeter, F. Krismer, and J. W. Kolar, "Weight optimization of a cooling system composed of fan and extruded-fin heat sink", *IEEE Transactions on Industry Applications*, vol. 51, pp. 509–520, Jan 2015.

[85] Fischerelelctronik, *Luefteraggregate mit Axialluefter*, 2013.

[86] *Linear Optocoupler IL300, High Gain Stability, Wide Bandwidth.*

[87] X. Liu, Z. Hou, and S. Jin, "Switching adaptive control of a class of non-affine nonlinear systems", in *Proceedings of the 32nd Chinese Control Conference*, pp. 2986–2991, Xi'an, China, July 2013.

[88] *LTC6246/LTC6247/LTC6248 180MHz, 1mA Power Effcient Rail-to-Rail I/O Op Amps.*

[89] H. John, *DER GERAEUSCHARME ELEKREOMOTOR.* 1950.

[90] P. John E. k. Foreman, *SOUND ANALYSIS AND NOISE CONROL.* 1990.

[91] Z. Q. Zhu, Z. P. Xia, L. J. Wu, and G. W. Jewell, "Analytical modeling and finite-element computation of radial vibration force in fractional-slot permanent-magnet brushless machines", *IEEE Transactions on Industry Applications*, vol. 46, pp. 1908–1918, Sep. 2010.

[92] R. Islam and I. Husain, "Analytical model for predicting noise and vibration in permanent-magnet synchronous motors", *IEEE Transactions on Industry Applications*, vol. 46, pp. 2346–2354, Nov 2010.

[93] S. M. Castano, B. Bilgin, E. Fairall, and A. Emadi, "Acoustic noise analysis of a high-speed high-power switched reluctance machine: Frame effects", *IEEE Transactions on Energy Conversion*, vol. 31, pp. 69–77, March 2016.

[94] M. Arata, N. Takahashi, M. Fujita, M. Mochizuki, T. Araki, and T. Hanai, "Noise lowering for a large variable speed range use permanent magnet motor by frequence shift of electromagnetic forces causing structural resonance", in *8th International Conference on Power Electronics - ECCE Asia*, pp. 1398–1405, Jeju, South Korea, May 2011.

[95] P. Pellerey, V. Lanfranchi, and G. Friedrich, "Coupled numerical simulation between electromagnetic and structural models. influence of the supply harmonics for synchronous machine vibrations", *IEEE Transactions on Magnetics*, vol. 48, pp. 983–986, Feb 2012.

[96] A. Bahr and S. Beineke, "Mechanical resonance damping in an industrial servo drive", in *2007 European Conference on Power Electronics and Applications*, pp. 1–10, Aalborg, Denmark, Sep. 2007.

[97] J. Zheng, Y. Feng, and X. Yu, "Mechanical resonance suppressing method for pmsm system based on high-order sliding modes", in *IECON 2007 - 33rd Annual Conference of the IEEE Industrial Electronics Society*, Taipei, Taiwan, Nov 2007.

[98] A. Cavagnino, S. Saied, and S. Vaschetto, "Experimental identification and reduction of acoustic noise in small brushed dc motors", *IEEE Transactions on Industry Applications*, vol. 50, pp. 317–326, Jan 2014.

[99] M. N. Anwar, I. Husain, S. Mir, and T. Sebastian, "Evaluation of acoustic noise and mode frequencies with design variations of switched reluctance machines", *IEEE Transactions on Industry Applications*, vol. 39, pp. 695–703, May 2003.

[100] X. Feng, "Investigation of the acoustic behavior of a brushless dc motor", Master's thesis, Technical University Berlin, 2017.

[101] J. L. Besnerais, Q. Souron, and E. Devillers, "Analysis of the electromagnetic acoustic noise and vibrations of a high-speed brushless dc motor", in *8th IET International Conference on Power Electronics, Machines and Drives (PEMD 2016)*, pp. 1–10, Glasgow, UK, April 2016.

[102] M. K. Ghosh, Y. Gao, H. Dozono, K. Muramatsu, W. Guan, J. Yuan, C. Tian, and B. Chen, "Proposal of maxwell stress tensor for local force calculation in magnetic body", *IEEE Transactions on Magnetics*, vol. 54, pp. 1–4, Nov 2018.

[103] G. Jeong, H. Choi, H. Kim, H. Kim, and S. Lee, "Evaluation of magnetic force distribution and torque due to smooth interaction body force density in permanent-magnet materials", *IEEE Transactions on Magnetics*, vol. 47, pp. 2819–2822, Oct 2011.

[104] U. Schaefer, *Electrical Machines ii*, EA, Technische Universitaet Berlin, 2018.

[105] H. C. M. Mai, R. Bernard, P. Bigot, F. Dubas, D. Chamagne, and C. Espanet, "Consideration of radial magnetic forces in brushless dc motors", in *2010 International Conference on Electrical Machines and Systems*, pp. 1–6, Incheon, South Korea, Oct 2010.

[106] D. Kim, M. D. Noh, and Y. Park, "Unbalanced magnetic forces due to rotor eccentricity in a toroidally wound bldc motor", *IEEE Transactions on Magnetics*, vol. 52, pp. 1–4, July 2016.

[107] P. Pillay and W. Cai, "An investigation into vibration in switched reluctance motors", in *Conference Record of 1998 IEEE Industry Applications Conference. Thirty-Third IAS Annual Meeting (Cat. No.98CH36242)*, vol. 1, pp. 341–350 vol.1, St. Louis, MO, USA, Oct 1998.

[108] and P. Pillay and A. M. Omekanda, "Vibration prediction in switched reluctance motors with transfer function identification from shaker and force hammer tests", *IEEE Transactions on Industry Applications*, vol. 39, pp. 978–985, July 2003.

[109] Z. Q. Zhu, Z. P. Xia, L. J. Wu, and G. W. Jewell, "Analytical modelling and finite element computation of radial vibration force in fractional-slot permanent magnet brushless machines", in *2009 IEEE International Electric Machines and Drives Conference*, pp. 144–151, Miami, FL, USA, May 2009.

[110] J. H. Leong and Z. Q. Zhu, "Acoustic noise and vibration of direct-torque-controlled permanent magnet brushless dc drives", in *6th IET International Conference on Power Electronics, Machines and Drives (PEMD 2012)*, pp. 1–6, Bristol, UK, March 2012.

[111] X. Ge, "Simulation of vibration in electrical machines for hybrid-electric vehicles", Master's thesis, CHALMERS UNIVERSITY OF TECHNOLOGY, Goeteborg, 2014.

[112] Y. Kano, T. Kosaka, and N. Matsui, "Simple nonlinear magnetic analysis for permanent-magnet motors", *IEEE Transactions on Industry Applications*, vol. 41, pp. 1205–1214, Sept 2005.

[113] K. Bienczyk, "Angle measurement using a miniature hall effect position sensor", in *2009 2nd International Students Conference on Electrodynamic and Mechatronics*, pp. 21–22, Dallas, TX, USA, May 2009.

[114] H. K. Kim and J. Hur, "Dynamic characteristic analysis of irreversible demagnetization in spm- and ipm-type bldc motors", *IEEE Transactions on Industry Applications*, vol. 53, pp. 982–990, March 2017.

[115] W. A. Roshen, "Magnetic losses for non-sinusoidal waveforms found in ac motors", *IEEE Transactions on Power Electronics*, vol. 21, pp. 1138–1141, July 2006.

[116] W. Roshen, "Ferrite core loss for power magnetic components design", *IEEE Transactions on Magnetics*, vol. 27, pp. 4407–4415, Nov 1991.

[117] A. Boglietti, P. Ferraris, M. Lazzari, and F. Profumo, "Iron losses in magnetic materials with six-step and pwm inverter supply (induction motors)", *IEEE Transactions on Magnetics*, vol. 27, pp. 5334–5336, Nov 1991.

[118] F. Fuerst, "Design of a 48v three-phase inverter", Master's thesis, CHALMERS UNIVERSITY OF TECHNOLOGY, Goeteborg, 2015.

[119] U. Drofenik, A. Stupar, and J. W. Kolar, "Analysis of theoretical limits of forced-air cooling using advanced composite materials with high thermal conductivities", *IEEE Transactions on Components, Packaging and Manufacturing Technology*, vol. 1, pp. 528–535, April 2011.

[120] *Maxwell Online Help*, 2008.

Schriftenreihe **Elektrische Energietechnik an der TU Berlin**
Hrsg.: Prof. Dr. Sibylle Dieckerhoff, Prof. Dr. Julia Kowal, Prof. Dr. Ronald Plath, Prof. Dr. Uwe Schäfer

ISSN 2367-3761 (print)
ISSN 2367-377X (online)

1: Dinca, Christian: Motor design for maximum material exploitation and magnetization procedure with in-line quality check for mass production. - 2017. - XV, 168 S.
ISBN **978-3-7983-2883-9** (print) EUR **13,00**
ISBN **978-3-7983-2884-6** (online)
DOI 10.14279/depositonce-5630

2: Gkountaras, Aris: Modeling techniques and control strategies for inverter dominated microgrids. - 2017. - 169 S.
ISBN **978-3-7983-2872-3** (print) EUR **12,00**
ISBN **978-3-7983-2873-0** (online)
DOI 10.14279/depositonce-5520

3: Wolz, Christoph: Ein schnelles und genaues Simulationsmodell für permanentmagnet-erregte Kommutatormotoren kleiner Leistung mit Zahnspulen unter Berücksichtigung nichtlinearer Eigenschaften. - 2017. - XXI, 178 S.
ISBN **978-3-7983-2934-8** (print) EUR **14,00**
ISBN **978-3-7983-2935-5** (online)
DOI 10.14279/depositonce-5911

4: Zerbe, Johannes: Innovative Wickeltechnologien für Statorspulen zur Erhöhung des erregte Kommutatormotoren kleiner Leistung Füllfaktors und Reduzierung der Beanspruchungen im Wickelprozess. - 2019. - 227 S.
ISBN **978-3-7983-3045-0** (print) EUR **13,50**
ISBN **978-3-7983-3046-7** (online)
DOI 10.14279/depositonce-7533

5: Schneider, Simon Michael: Test bench design for power measurement of inverter-operated machines in the medium voltage range. - 2018. - xii, 128 S.
ISBN **978-3-7983-3024-5** (print) EUR **11,00**
ISBN **978-3-7983-3025-2** (online)
DOI 10.14279/depositonce-7222

6: Winkler, Tammo: Untersuchungen an weich schaltenden DC/DC Konvertern zur Versorgung von Hochleistungs-Diodenlasern. - 2019. - vi, 133 S.
ISBN **978-3-7983-3078-8** (print) EUR **12,00**
ISBN **978-3-7983-3079-5** (online)
DOI 10.14279/depositonce-8324

7: Sarmadi, Mohammed-Ali: Entwurf und Konstruktion einer vertikal laufenden Windturbine nach dem Widerstandsprinzip unter Nutzung der aerodynamischen Eigenschaften eines Flügelprofils. - 2018. - XX, 122 S.
ISBN **978-3-7983-3043-6** (print) EUR **11,00**
ISBN **978-3-7983-3044-3** (online)
DOI 10.14279/depositonce-7659

8: Eial Awwad, Abdullah: On the perspectives of SiC MOSFETs in high-frequency and high-power isolated DC/DC converters. - 2020. - xvii, 158 S.
ISBN **978-3-7983-3096-2** (print)
ISBN **978-3-7983-3097-9** (online)
DOI 10.14279/depositonce-8556

Universitätsverlag der TU Berlin

Design and comparison of two brushless DC drives for an electric propulsion system of solar-power unmanned aerial vehicles

The electrical propulsion system as the core component of solar-power Unmanned Aerial Vehicles (UAVs) for long duration flight requires high power density and stable drive technology. Brushless DC motors (BLDCM) with high power and torque density and control algorithms suitable for drive system are given preference for the application in UAVs.
This dissertation is aimed at designing an improved BLDCM using only 4 interior magnet blocks to realize 8 poles compared to the conventional 8 magnet blocks structure.
The performances of both BLDCM designs have been analytically determined and the motor models were verified through finite element software in ANSYS. Design and construction of the demonstrators of BLDCMs with the proposed and the conventional magnet structure have been carried out and a test bench for extensive performance comparison has been set up.
Since the proposed magnet structure leads to a particularity of the magnetic circuit, the behavior of absolute and differential synchronous direct and quadrature inductances have been investigated by finite element model analysis and experiments.

ISBN 978-3-7983-3126-6 (print)
ISBN 978-3-7983-3127-3 (online)

ISBN 978-3-7983-3126-6

http://verlag.tu-berlin.de